POLITECNICO DI MILANO
MECHANICAL DEPARTMENT
DOCTORAL PROGRAMME IN ENGINEERING OF MECHANICAL SYSTEMS

EXPERIMENTAL CHARACTERIZATION OF MICROSTRUCTURAL DAMAGE MECHANISMS

Doctoral Dissertation of:
Luca Patriarca

Supervisors:
Prof. Stefano Beretta (Politecnico di Milano)
Prof. Huseyin Sehitoglu (University of Illinois at Urbana-Champaign)

Tutor:
Prof. Tullio Tolio

The Chair of the Doctoral Program:
Prof. Bianca Maria Colosimo

2013 – Cicle XXV

Abstract

This work presents an experimental approach to investigate the material behavior at the micro-scale of two important alloys (FeCr and γ-TiAl) for structural applications. Local strain fields at multiple length scales are measured using an advanced optical technique. Local strain heterogeneities arises as a consequence of the local microstructure and deformation mechanisms. This work aims to gain further insights into the relation between the mechanical behavior of metals at the micro-scale with the observed mechanical behavior on the meso and macro scales. The main findings presented here provide valuable information into the deformation mechanisms activated in bcc metals (slip and twinning), which can be utilized by researchers as the basis of analytical models to be developed in the next future.

The work is divided into three main parts. In the first part, tension and compression experiments were conducted on multiple single crystal orientations of body-centered cubic Fe-47.8Cr single crystals. The critical resolved shear stress magnitudes for slip, twin nucleation and twin migration were established. The results show that the nucleation of slip always precedes twinning which nucleates with an associated load drop at an higher critical resolved shear stress. Following twin nucleation, twin migration proceeds at a critical resolved shear stress that is lower than the initiation stress. The experimental results of the nucleation stresses indicate that the Schmid law holds to a first approximation for the slip and twin nucleation cases, but to a lesser extent for twin migration particularly when considerable slip strains preceded twinning. The critical resolved shear stresses were determined experimentally using digital image correlation in conjunction with electron back scattering diffraction. The digital image correlation enabled pinpointing the precise stress on the stress-strain curves where twins or slip were activated. The crystal orientations were obtained using electron back scattering diffraction and used to determine the activated twin and slip systems through trace analysis. The results presented in Chapter 2 provide a considerable contribution in understanding the micro-mechanical behavior of bcc alloys.

In the second part of the present work slip transmission through grain boundaries is investigated. The full slip dislocation blockage, or the partial slip dislocation transmission processes at grain interfaces provide a significant contribution at the material strengthening. The study focuses on the link from the deformation mechanisms at the micro-scale to the global mechanical behavior (macro-scale). Strain fields across grain boundaries were measured using advanced digital image correlation techniques. In conjunction with strain measurements, grain orientations from electron back-scattered diffraction were used to establish the dislocation reactions at each boundary, providing the corresponding residual Burgers vectors due to slip transmission across the interfaces. A close correlation was found between the magnitude of the residual Burgers vector and the local strain change across the boundary. When the residual Burgers vector magnitude (with respect to the lattice spacing) exceeds 1.0, the high strains on one side of the boundary are paired with low strains across the boundary. When the residual Burgers vector approaches zero, the strain fields vary smoothly across the boundary. The FeCr bcc alloy exhibits single slip per grain making the measurements and dislocation reactions rather straightforward. The work points to the need to incorporate details of slip dislocation-grain boundary interaction (slip transmission) in modeling research.

In the last part of the work, a γ-TiAl alloy manufactured with electron beam melting technology is examined. The electron beam melting technology enables to avoid typical manufacturing defects. It follows that experiments carried out on this material provide several insights into the microstructural damage mechanisms leading to crack initiation. Classical experimental methodologies for the fatigue characterization were conducted adopting plain fatigue specimens, fatigue specimens with an initial artificial defect, and crack propagation specimens. Preliminary considerations from these experiments indicate that the interfaces between lamellar-lamellar grains, and lamellar-equiaxed grains act as potential crack initiation sites. Taking into account the typical lamellar grain size, the fatigue resistance of the duplex γ-TiAl alloy can be predicted. Further investigations on the influence of the microstructure were obtained using residual strain fields via high resolution digital image correlation in combination with high resolution images of the local microstructure after etching.

To all those who live their passions

And

To all those who let be led by those of others

Acknowledgements

First of all I would like to thank my parents, Paola and Oreste, for letting me follow my dreams, even if this implied to give something up in their life. I'm also thankful for my friends Mauro Madia and Paolo Berbenni (in Italy), and Wael Abuzaid (in US) who, during my PhD program, never missed their support (especially in my difficult periods), they became friends other than just colleagues. I'm also thankful for all the other friends who came in my life in these three years, in which I crossed for five times the ocean between Italy and US. In US I'd like to thank Piyas, Garrett, Mallory, Tawhid, Jay, Avinesh, Jifeng, Alpay, Emre with whom I enjoyed the time in the office and the lab. Simone, Claudia, Hannah, Beatriz, Riccardo, Giovanni, Francesco, Chiara, Francesca, Lynn, Federico, Dave, Aya, Arnulfo for being my housemates, friends, and "snack mates". In Russia, my ex-colleague, and very close friend Khaydar. In Italy I'd like to thank Daniele, Michele, Stefano and all the other colleagues in Polimi, also Marta, Isabella, Paolo, Ottavio, Francesco, Andrea, Massi, Sara, Enrico, Romina, Nonna for being a necessary support.

Special thanks go to my two advisors and mentors Prof. Huseyin Sehitoglu, and Prof. Stefano Beretta. Prof. Huseyin Sehitoglu for helping me in my scientific and personal growth with his weekly meetings, his daily suggestions, his strong encouragements in improving the quality of the work, his persistence in helping me with my writings (for sure not one of my best skills, at least in English), and his kindness in supporting and being interested not only in our work in the office, but also in our life outside the office. Prof. Stefano Beretta for letting me develop my research topic with no time-limits in US, for his encouragements even from Italy, his visits in Champaign, his continuous ideas and enthusiasm in the research work, and his patience in waiting for me for setting up the lab in Polimi with the experimental tools I've been using in US.

Finally I'd like to thank everybody who shared my feelings, my ideas, my passions in these three years. Without deep relations among people, the pure work would not mean a thing.

Table of Contents

INTRODUCTION **5**

I.1. Experimental approach 6

I.2. Twin nucleation and migration, slip onset in FeCr single crystals 7

I.3. Slip transmission through Grain Boundaries in FeCr 11

I.4. Strain localizations in a γ-TiAl alloy 14

CHAPTER 1

EXPERIMENTAL METHODOLOGY **17**

1.1. Digital Image Correlation 17

1.1.1. In situ DIC *19*

1.1.2. Ex situ DIC *21*

1.1.3. In situ versus ex situ DIC *23*

1.2. DIC application for measuring Twin Nucleation and Migration stresses in FeCr single crystals 25

1.2.1. Incremental Digital Image Correlation *25*

1.3. Slip onset in FeCr single crystals 27

1.4. Strain fields from Grain-Boundary - Slip interaction 29

1.4.1. Strain accumulation on FeCr grain boundaries *29*

1.4.2. Strain accumulation on TiAl *31*

1.5. Slip and twin indexing 32

CHAPTER 2

TWIN NUCLEATION AND MIGRATION IN FECR SINGLE CRYSTALS **35**

2.1. Experimental setup 36

2.1.1. Sample geometries *36*

2.1.2. Digital Image Correlation setup *37*

2.2. Stress-strain curves 38

2.3. Activated twin and slip systems 40

2.4. Crystal orientation $[0\,\overline{1}0]$ 42

2.4.1. Tension experiments *43*

2.4.2. Compression experiments *46*

2.5. CRYSTAL ORIENTATION $[\bar{1}1\,\bar{1}]$ 47
2.5.1. Compression experiments *47*
2.6. CRYSTAL ORIENTATION $[\bar{1}0\,\bar{1}]$ 49
2.6.1. Tension experiments *49*
2.6.2. Compression experiments *52*
2.7. CRYSTAL ORIENTATION $[314]$ 55
2.7.1. Compression experiments *55*
2.8. FURTHER ANALYSIS OF THE RESULTS 56
2.8.1. Twin Migration Stress *57*
2.8.2. Strain Hardening *57*
2.8.3. Twin Nucleation Stress *58*
2.8.4. Slip Nucleation Stress *58*

CHAPTER 3

SLIP TRANSMISSION THROUGH GRAIN BOUNDARIES IN FECR POLYCRYSTAL 59

3.1. SCHEMATIC OF SLIP DISLOCATION–GRAIN BOUNDARY INTERACTION 59
3.2. MATERIAL AND METHODS 61
3.2.1. Microstructure characterization *61*
3.2.2. Experimental set-up and strain measurements *62*
3.3. RESULTS 63
3.3.1. Stress-strain curve and DIC strain measurements *63*
3.3.2. High resolution DIC strain measurements *67*
3.3.3. Strain measurements across grain boundaries *70*
3.4. DISCUSSION 73

CHAPTER 4

DAMAGE ACCUMULATION ON Γ-TIAL 75

4.1 MANUFACTURING PROCESS 75
4.2 MATERIAL 77
4.2.1 Microstructure *77*
4.3 FATIGUE EXPERIMENTS WITH PLAIN SPECIMENS 80
4.3.1 Experimental set-up *80*
4.3.2 Results *80*
4.4 FATIGUE EXPERIMENTS WITH ARTIFICIAL DEFECTS 82

4.4.1 Experimental set-up *82*
4.4.2 Results *82*
4.5 FATIGUE CRACK GROWTH EXPERIMENTS 84
4.5.1 Experimental set-up *84*
4.5.2 Results *86*
4.6 UNIAXIAL STATIC EXPERIMENTS USING DIC 90
4.6.1 Experimental set-up *90*
4.6.2 Results *92*
4.6.3 Compression experiment *92*
4.6.4 Tension experiment *93*
4.7 FINAL CONSIDERATIONS 95

CHAPTER 5

CONCLUDING REMARKS AND FUTURE DEVELOPMENTS 97

5.5 CONCLUDING REMARKS 97
5.1.1. Results of Chapter 2 ..... *97*
5.1.2. Results of Chapter 3 ..... *98*
5.1.3. Results of Chapter 4 ..... *98*
5.2. FUTURE DEVELOPMENTS 99
5.2.1. High Temperature experiments on FeCr *99*
5.2.2. Ex Situ Digital Image Correlation using SEM *102*

REFERENCES 105

Introduction

The characterization of the material behavior under the effect of static or repeated loads is one of the largest and most studied research field for mechanical and material science engineers. Nevertheless the abilities to predict mechanical behaviors of materials increased in the last decades, new and more reliable models are necessary in order to improve the quality and the safety of the component design. The increased ability to predict material behavior resides in the ability of the scientists to decrease the length-scales of the observations of the deformation mechanisms (*micro* and *nano* scales), and use this knowledge for predicting the global mechanical behavior (*macroscopic* scale). From the *experimental point of view* the investigation at the micro and nano scales involve different difficulties which are not encountered using the classical approaches on the continuous medium scale. First of all the active deformation mechanisms (slip and twin) depend on the atomistic structure of the analyzed material. In addition, the active deformation mechanisms are typically strongly dependent on the testing and environmental conditions: temperature, strain rate, etc., so the analyses need to be implemented at specific and defined conditions. Another important aspect to consider for these approaches is the limited area which can be studied. Since the phenomena involving dislocation motions are observed at nano-scales, the target area is small, and a general picture of the phenomena at meso-scale is difficult to draw. The main idea pursued in this work is to link the phenomena which occur at micro-level (slip and twin) with the resolved strains on the meso-scale. Experimentally, Digital Image Correlation (DIC) was used to investigate the local strain heterogeneities on the sample surface and correlate them with the microscopically activated deformation mechanisms.

In the following sections the main research areas covered in this work are introduced, along with an introduction to the materials under investigation. Section I.1 gives an overview of the experimental methodology adopted. Section I.2 introduces the study on FeCr single crystals, focusing on the experimental determination of the critical resolved shear stresses for slip onset, twin nucleation and migration. Section I.3 presents the fundamentals of the work on the FeCr polycrystal samples, DIC is used to measure strain changes across the grain boundaries in order to correlate the microstructural grain boundary behavior with the strains measured on the macro-scale. Finally, Section I.4 introduces the study on one γ-TiAl alloy in order to work out the effect of the microstructure on the fatigue behavior for these alloys.

I.1. Experimental approach

Along this work, Digital Image Correlation (DIC) is used to characterize the mechanical behavior of a FeCr alloy, and to study the crack initiation sites for a γ-TiAl alloy. For both the materials the experimental approach is the same, and it is schematically depicted in Figure I.1. DIC is used to capture local strain heterogeneities which develop on the sample surface as a consequence of local deformation mechanisms (slip/twin). The determination of crystal orientation through Electron Back-Scattered Diffraction (EBSD) for the same area covered with strain measurements allows the indexing of the slip/twin systems, and in case of a polycrystal material, also the definition of the grain boundaries. Further analysis of the sample surface (for example detections of small cracks, microstructure characterization following etching, etc.) is achieved using the Scanning Electron Microscope (SEM) or other optical devices.

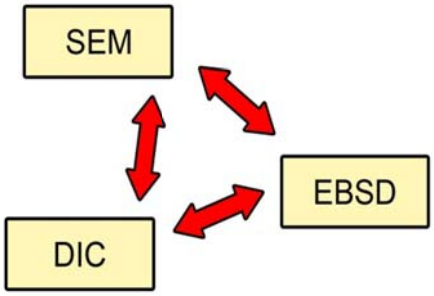

Figure I.1. Adopted experimental approach. Strain measurements via Digital Image Correlation are used in conjunction with crystal orientations from Electron Back-Scattered Diffraction technique and images obtained from Scanning Electron Microscope (SEM), or common optical microscopes.

One of the first pioneering work employing DIC was proposed in the early 1950s by Gilbert Hobrough who firstly tried to correlate high resolution photos in order to extract the information about the positions of different features on the images [1, 2]. In the 1960s and 1970s DIC methodologies found a great success in different research fields, in particular in the experimental solid mechanics field applying laser technology [3-8]. Starting with the work of Peters and Ranson [9], successively developed and refined by different authors [9-13], the numerical algorithms which form the basis for the 2D-DIC were proposed and validated. DIC is based on algorithms able to track the position of subset of pixels between two images and thus reconstruct the displacement filed. The sample surface is specifically treated in order to produce a random *speckle pattern* adapted for the purpose specified. In this work DIC is used in two different ways: *in-situ* DIC which refers to the real-time imaging acquisition process, the strain fields are then captured during the loading of the sample; alternatively, *ex-situ* DIC which refers to the imaging acquisition out of the load frame using an optical microscope.

Generally speaking, deformation mechanisms (slip and twinning) produce local strain heterogeneities on the sample surface. Adopting an in-situ DIC set-up is possible to capture the onset of slip and twinning measuring the localized strains on the sample area detected with the camera. This experimental set-up is particularly suited for the experiments on the FeCr single crystal samples, since the analyzed sample areas are characterized by the same crystal orientation, thus displaying an homogeneous mechanical behavior in terms of active twin and slip systems. Moving the attention to the polycrystal cases (FeCr and γ-TiAl alloy), the adoption of the DIC in-situ set-up is not adapted for capturing local strain heterogeneities and correlate them with the local microstructure. In fact, for these cases, the microstructure is small compared with the strain resolution typically used for in-situ applications. Higher image resolutions are required, and they can be obtained only using ex-situ DIC.

The characteristics of the implementation of in-situ and ex-situ DIC are described in Chapter 1. In particular, the chapter explains the different DIC applications for the specific cases addressed along the work.

I.2. Twin nucleation and migration, slip onset in FeCr single crystals

Chapter 1 presents the experimental results obtained from experiments on iron-chromium (FeCr) single crystal samples loaded along selected crystal orientations. Understanding the deformation response of iron based body-centered cubic (bcc) alloys has significant merit, as these alloys form the basis of materials that are widely utilized in structures. In particular, the Fe-Cr alloys are widely used in chemical and nuclear applications. For common structural applications, the percentage of chromium content doesn't exceed 30 at. pct. since higher chromium contents favor cleavage fractures, as a consequence of the high stresses present at twin-twin intersections [14-16]. However, adopting heat treatments that remove interstitial impurities drastically improve the brittleness of these alloys, and good mechanical properties (in particular ductility) are obtained. It is of great importance to provide a complete material characterization for these alloys, which can be also useful in order to gain further insides into the mechanical behavior of bcc materials. The majority of the previous investigations on FeCr alloys were carried out on polycrystals [17-22], whereas in the first part of this study single crystals have been employed to activate specific twin and slip systems.

Macroscopically, deformation by slip is accommodated by the sliding of planes of atoms one over the other as schematically reported in Figure I.2a. From the atomistic point of view, slip is originated by dislocation motion. Depending on the crystal structure (fcc, bcc, hcp) different crystallographic planes and different shear directions can be activated. For bcc materials, the typical slip planes are contained on the well-known $\{011\}$, $\{112\}$, $\{123\}$ families of planes, while the directions are contained on the $<111>$ family.

Twinning is still originated by an applied shear stress (Figure I.2b). A region inside the crystal is re-oriented according to a crystal symmetry (a mirror of the original crystal in terms of crystal orientation), this region is named twin. For bcc materials a load drop typically occurs during twin nucleation, in particular twin can also nucleate in the elastic region of the stress-strain curve [23].

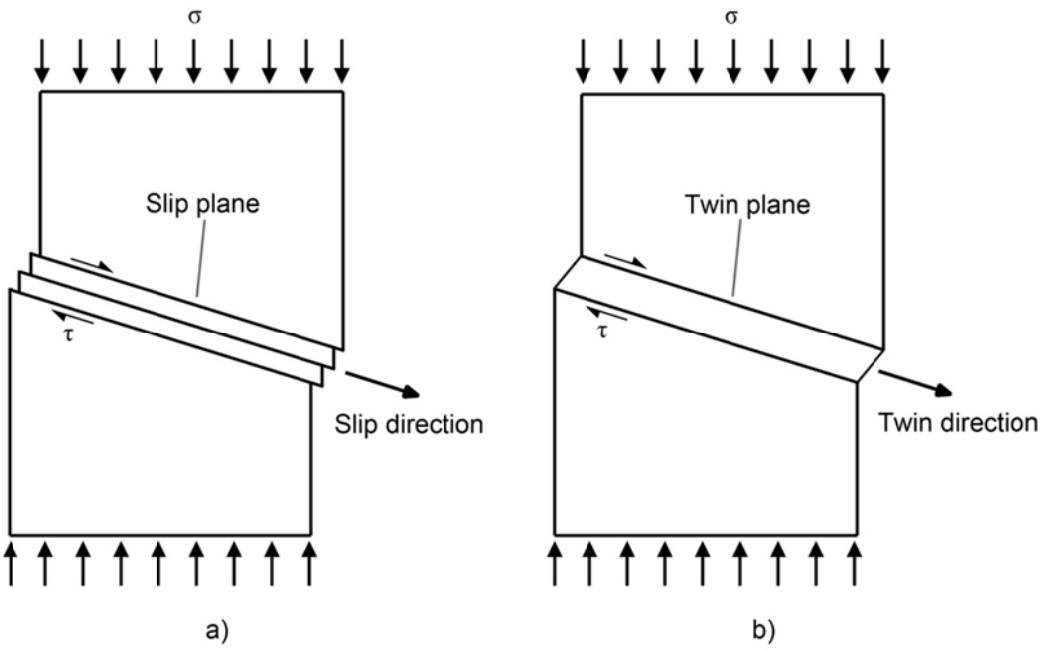

Figure I.2. Schematic of a) slip and b) twinning viewed on a single crystal.

For many years researchers studied dislocation mechanisms for twin nucleation and successive growth (also referred as *twin migration*), from the atomistic point of view. From these studies different theories explaining the dislocation mechanism which originate the twin nuclei were proposed (for bcc materials see [24-27]). From the experimental point of view, the adoption of the transmission electron microscope (TEM) allowed researches to clearly observe twinning (see i.e. [28-30]), in addition to classical studies adopting the optical microscope and the electron back-scattered diffraction (EBSD) methodology. Despite all these experimental approaches can provide several insights into the mechanisms of twin nucleation and eventual twin interaction with slip dislocations, there is a need to understand better what is the effect in terms of local strains on the meso-scale and how these strains are related with the active twin systems. It will be shown in the following that the implementation of strain measurements via digital image correlation on single crystal samples allows to capture several information on the twin and slip formation (and eventually successive interaction), which cannot be otherwise obtained adopting classical experimental, approaches such as TEM. In fact, the main advantage is that with the adopted image resolution it is possible to cover large sample areas, in particular adopting real time data acquisition, which is a difficult operation to obtain with other experimental techniques.

Another important aspect of this approach is that the use of specimens manufactured as single crystals with a specific crystal orientation in the load direction enables to study separately crystal orientations which display predominantly slip and crystal orientations that display also twinning. The complexity of using a polycrystal material relates to the difficulties of neglecting the effects of the grain boundaries, and more important, the random choice of the grain orientation. The idea pursued here is to load statically (in compression and tension) and study each selected crystal orientation using a defined experimental approach (crystal orientation from EBSD and strain measurements from DIC), and provide for each orientation the evolution of the local strain fields associated with slip and twinning. Since by using DIC methodology it is also possible to capture the *real-time* evolution of the strains during loading, the first point of the analysis is the measure of the exact point of twin and slip nucleation along the stress-strain curve. Different works dealt already the existence of a critical resolved shear stress for both slip and twinning. In particular, it is well established that the resolved shear stress for twinning is constant when different factors are fixed: alloy composition, temperature, strain rate, etc. For an exhaustive review on this topic and references see [23]. Many studies have been carried out on the dependence of these factors on the occurrence of twinning, but less interest has been devoted in understanding what is the effect of twinning on the local strain field, and more important what is the effect on the crystal behavior based on the point of twin nucleation on the stress-strain curve. In this sense, the use of EBSD and DIC can shed light into the study of twin nucleation and subsequent twin growth, in particular in terms of associated strain fields. Moreover, this work can provide a solid basis of experimental results which can be useful for understanding the subsequent slip and twin evolution (for example twin migration) and the interactions (slip/twin, slip/slip and twin/twin). In fact, since all the observed slip and twin systems have been indexed, the results can also be useful for testing plasticity framework based on active slip and twin systems. These concepts can be better understood analyzing the schematic proposed in Figure I.3 (obtained from the experiments proposed in Chapter 2) which represents a conceptual summary of the different stress-strain curves based on the load direction and the crystal orientation for bcc alloys. The stress-strain curves reported in Figure I.3 schematize the different possible mechanical behaviors of the FeCr single crystals depending on the active deformation mechanism (slip and/or twinning). It is evident that, based on the active slip/twin systems, a different level of crystal hardening is observed, along with a completely different mechanical behavior. Case (a) a load drop occurring in the nominally *elastic* part of the stress-strain curve characterizes the deformation behavior for the analyzed crystal orientation. The open questions are: what is the mechanism which leads to the observed load drop (slip or twinning)? The deformation mechanisms preceding and following the load drop are the same? What is the influence of the deformation mechanism activated during the load drop on the subsequent crystal deformation? Case (b) describes a slightly different crystal behavior, in fact along the stress-strain curve the load drop is preceded by a flat region which is characterized by an active deformation mechanism which doesn't provide hardening till the load drop. Also in this

case it is interesting to analyze what are the active slip and twin systems, and how these mechanisms interact and provide the measured strain fields. The last cases (c and d) define other two possible deformation behaviors which can be observed. In the latter cases no load drops have been observed, but two different hardening modulus are measured. In this case the observation of the strain fields, along with crystal orientations from EBSD can provide useful information on the active deformation mechanisms, and the explanation of the different observed hardening modulus. These questions can be answered only with a real-time data acquisition, and the first part of this work (Chapter 2) will cover this topic.

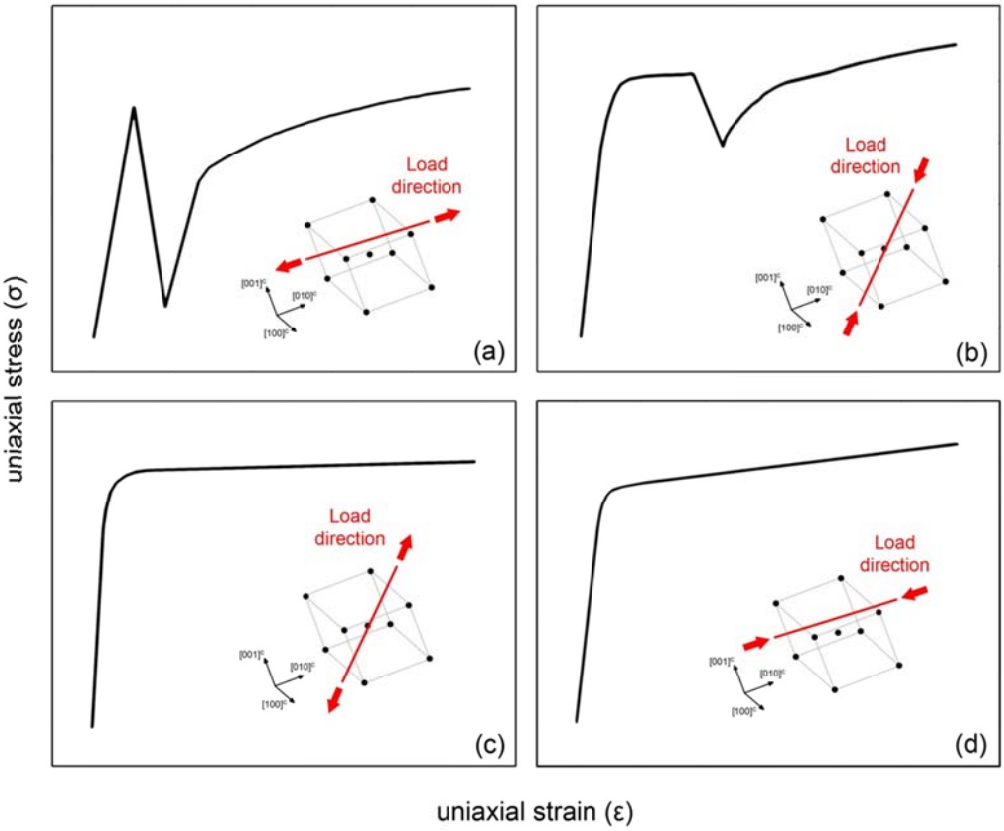

Figure I.3. Schematic of the possible crystal deformation behaviors for a bcc FeCr alloy. The stress-strain curve depends on the crystal orientation and load direction (tensile versus compressive load). The different deformation behaviors and load direction dependence of bcc alloys derive from the possibility of differently activate slip and/or twin systems.

The knowledge of the active slip and twin systems can also be useful in order to analyze the effect on the hardening induced by the different possible interaction mechanisms: slip-slip interactions, twin-slip interactions and twin-twin interactions. In general, a twin boundary can represent an obstacle to a slip dislocation or to another incoming twin. It follows that the reaction occurring at the twin boundary can provide a significant influence on the mechanical behavior of the alloy. For example, based on the reaction at the twin boundary, a slip dislocation needs to overcome an energy

barrier in order to react with the twin boundary [31], thus leading to an increment of the material strength. Twin-twin and twin-slip interactions can be beneficial for the strengthening of the material, but on the other side, the intersection regions can promote high strain and stress localizations. For example, twin-twin interactions are well-known for generating high localized stresses in the region of interaction, in particular when one twin is blocked in front of another twin [32-34]. Moreover, when loaded in tension, the reaction between some of the possible active twin systems for a particular crystal orientation can lead to the formation of the Cottrell dislocation which leads to cleavage fractures [32]. In general, in order to study the effect of the twin-twin interaction observed, it is useful to study the possible outcome in terms of dislocation reaction. For bcc materials different authors provided experimental studies showing the possible twin-twin and twin-slip reactions and the consequences on the mechanical behavior, see for example [35-38]. It is not the objective of the present work to focus on each twin-twin and twin-slip interaction observed and study the possible dislocation reactions. On the other side, giving the local strain measurements in correspondence of the twin-twin and twin-slip interactions can help in understanding the role of the interactions on the observed crystal hardening.

I.3. Slip transmission through Grain Boundaries in FeCr

Considerable research efforts have been devoted to incorporate dislocation slip at the crystal level to predict the overall response of metals. Substantial progress has been gained in predicting crystal orientation effects, strain hardening [39], slip-twin interactions [40], and change in crystallographic texture [41, 42]. Grain boundaries have been treated as a contributor to geometric hardening and the obstacle length has been incorporated in the models [40]. These models typically allow for predicting the overall macroscopic stress-strain response upon use of various homogenization schemes. Further advances in these models should encompass developments on grain boundary specifics. In fact, one of the strengthening mechanism at grain level is provided by the presence of grain boundaries which influence the slip dislocation transmission process. Grain boundaries act as a barrier to dislocation motion, thus inducing a contribution to the hardening of the alloy. The level of strengthening of the grain boundaries depends on the incoming and outgoing slip because of the different residual Burgers vectors that remain at the boundary. The level of strengthening associated with the grain boundaries can be quantified measuring the energetics of the slip transfer process. Using molecular dynamics simulations, Abuzaid at all established the energy barrier levels for different grain boundaries [43]. In particular, they analyzed different grain boundary specifics, showing that high energy barriers result in case of high residual Burgers vector magnitudes. The influence of the grain boundary specifics on the slip dislocation-GB interactions can also be experimentally studied on the meso-scales, since the slip transmission process influences the local deformation behavior at the grain boundaries. Over the years, studies examining dislocation-grain boundary interactions have been undertaken [44-47]. Historically, experiments on slip transmission

were conducted with optical microscopes or, more recently, using TEM (Figure I.4b). Using these techniques different authors established a series of possible dislocation reactions occurring at the Grain Boundary (see for example [48]). The main outcome of these studies is the role of the Burgers vector of the residual dislocation left at the grain boundary. As already briefly discussed in the preceding paragraphs, experimental techniques such as TEM, micro and nano indentation experiments [49-53], etc., provide an exhaustive, but localized analysis of the processes at the grain boundaries. The idea pursued in Chapter 3 is to study and analyze the slip transmission processes through grain boundaries on the meso-scale measuring the local strain fields across grain boundaries, and correlate these strain fields with the interaction of the incoming and outgoing slip systems through the grain interfaces. The use of the FeCr polycrystal samples, properly heat-treated in order to remove other hardening factors (for example fine dispersions of hard particles, martensite formation, strain aging in steels [54]), allowed to focus the study only on the crystal hardening introduced by dislocation-grain boundary interactions. Since every grain analyzed also displays only one main slip system, even the possible hardening introduced by slip-slip interactions is avoided [55]. In this scenario, the selected FeCr polycrystal represents the perfect material for studying slip dislocation-grain boundary interactions.

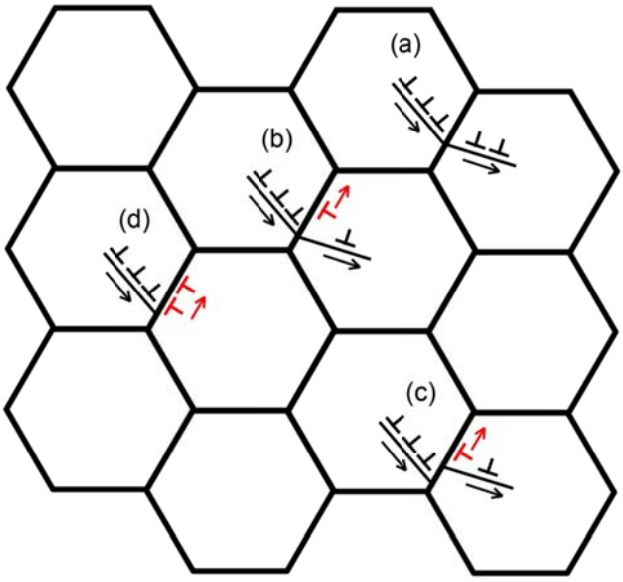

Figure I.4a. Slip dislocation-GB interactions in polycrystal materials: a) direct transmission, i.e. cross slip; b) direct transmission with generation of a residual dislocation on the grain boundary; c) indirect transmission; d) no transmission, the dislocations are incorporated inside the grain boundary.

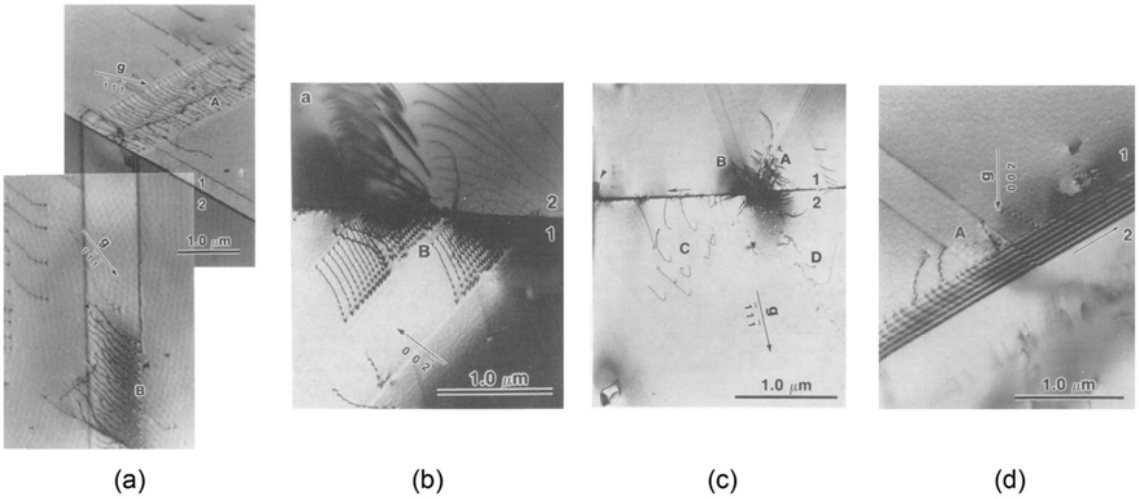

Figure I.4b. Examples of slip transmission studies using in situ TEM, from [48]: (a) Direct transfer of dislocation through the grain boundary; (b) Dislocation transfer with a residual dislocation left at the grain boundary; (c) Dislocation emission from the grain boundary from an area different than the point of interaction between the incident dislocations and the grain boundary; (d) slip dislocations absorbed at the grain boundary.

Clark et al. [56] and Lee at al. [48] utilized in situ TEM images and characterized the possible outcomes of the dislocation reactions occurring at a GB. Such studies form the basis of the analysis carried out here. The schematic proposed in Figure I.4a illustrates the possible dislocation-grain boundary interaction mechanisms. The schematic is paired with the experimental observations obtained via TEM reported in Figure I.4b (from [48]). In the cases presented in Figure I.4b, and in the grain boundaries analyzed in the present work, only one slip system in each grain is typically active in two adjacent grains. The general reaction provides an estimation of the residual dislocation left at the grain boundary as a consequence of the interaction between the incoming dislocations and the outgoing dislocations from the grain boundary. Recently, advanced simulation tools also provided further insight into energetics of these reactions [31, 57, 58]. Such studies provide fundamental calculations of the energy barriers which need to be overcome by a slip dislocation in order to react with the grain interface. In particular, Ezaz and co-workers [31] showed that these energy barriers depend on the magnitude of the residual Burgers vector left at the grain boundary. In respect to this, the adoption of simulation tools allow to fully characterize one singular local event on the nano-scale. From the experimental point of view, studies adopting TEM (see Figure I.4b) allow to verify the reactions proposed adopting these simulations. On the other side, the effects of these reactions on the entire grain boundary, and thus on the general polycrystal behavior, has received less attention. It is of high interest to analyze the entire grain boundary, and try to link the outcome of the dislocation reaction occurring at the interface with the behavior of the grain interface seen on the meso-scale. The idea pursued here is to use local strain measurements, e. g. the strain gradients following a specific slip-GB interaction, as a tool to experimentally quantify the role of the grain boundaries on

the meso-scale. To this aim, Chapter 3 analyzes and correlates the potential outcome of the dislocation reactions (local parameter) with the measured strain changes across grain boundaries (meso-scale behavior). The open question is: is there any possible parameter which is able to describe an average grain boundary behavior? Chapter 3 aims to answer this question, and shed further light into the localization of plastic strains due to dislocation-GB interactions.

I.4. Strain localizations in a γ-TiAl alloy

Gamma titanium aluminide based alloys (γ-TiAl) have become an important alternative for high temperature structural applications in the aircraft industry to supplant current nickel-based superalloys as the material of choice for low-pressure turbine blades [59, 60]. The advantages achieved by the use of γ-TiAl intermetallics are principally their low density (3.9-4.2 g/cm^3 as a function of their composition [61]), high specific yield strength, high specific stiffness, substantial resistance to oxidation and good creep properties up to high temperatures. Although the application of such materials appears very encouraging for the turbine engine industry, optimizing the performance improvements requires more advanced approaches to accurately predict fatigue strength and to demonstrate the damage tolerance of TiAl materials with respect to intrinsic or service-generated defects. Therefore, there is a need to understand and address the specific fatigue properties of these materials to assure adequate reliability of these alloys in structural applications [62]. The peculiarity of the alloy analyzed here is that components (and thus the samples) are manufactured using Electron Beam melting (EBM) technology. EBM is a technology based on a manufacturing process “layer by layer”, which allows a drastic reduction of the presence of defects such as inclusions, pores etc. In this scenario the influence of the material microstructure on the fatigue resistance becomes more important since the possible crack initiation sites are found in correspondence of defined microstructural features.

Figure I.5 shows the typical microstructures generally present on γ-TiAl alloys (this alloy is also indicated as a *duplex microstructure* alloy): the equiaxed grains and the lamellar colonies. The regions marked in red represent the critical regions for these alloys in terms of potential crack nucleation sites. Strains can accumulate at the grain boundaries as other polycrystalline materials (line marked (a) in Figure I.5a), or localized strains are detected in grain boundary regions where twins are blocked [63], or in triple points where strain incompatibilities are large [64]. The presence of the lamellar colonies create other potential sites where cracks can nucleate, for example as a consequence of the interfacial delamination and decohesion of the lamellar colonies [65].

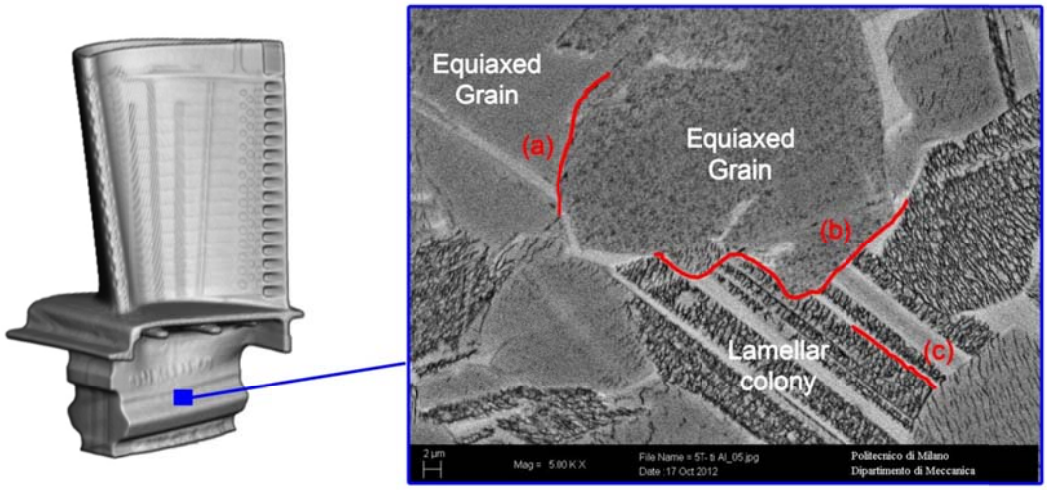

Figure I.5. Potential crack initiation sites due to the microstructure for a γ-TiAl alloy: a) interface between two equiaxed grains; b) interface between an equiaxed grain and a lamellar colony; c) decohesion between lamella phases or micro-cracking induced by slip blockage at lamellae interfaces.

Another important factor which influences the fatigue behavior is the presence of two phases (γ-TiAl and α_2-Ti_3Al) in the same microstructure (i.e. the lamellar colony) which creates an elastic incompatibility inside the lamellar package, thus favoring the decohesion phenomena (line marked (c) in Figure I.5c). It is evident that each of these potential *damage mechanisms* are strictly related with the presence of the two microstructures, their geometries, and the volume fraction of the phases. Chapter 4 investigates the mechanical behavior of the gamma titanium aluminide (γ-TiAl) Ti-48Al-2Cr-2Nb alloy with the aim to propose an experimental methodology able to investigate and quantify the main detrimental damage mechanisms at microstructural level. Two main sets of experimental results are presented. In the first part classical experimental methodologies (fatigue of smooth samples, fatigue of samples with artificial defects, crack propagation) are adopted for a general characterization of the alloy. From these experiments preliminary information about crack initiation sites are discovered. In the second part more information are obtained using high resolution ex-situ DIC strain measurements which confirm the main crack nucleation sites discovered and discussed in the first part of the chapter.

Chapter 1

Experimental methodology

The present work is characterized by an extensive usage of experimental strain measurements obtained via digital image correlation (DIC) methodology. An exhaustive reference on this technique is contained in [2]. In this chapter are briefly introduced the basic concepts and the details of the experimental techniques adopted along the work. Strain measurements from DIC and crystal orientations from electron back scattered diffraction methodologies (EBSD) were mainly used for studying the local strain fields associated with the different deformation mechanisms (slip, twinning, slip transmission across grain boundaries, twin-twin and twin-slip interactions). Each application requires a specific experimental set-up which will be analyzed in this chapter.

Section 1.1 contains general details on the DIC methodology. The first application of DIC is introduced in Section 1.2 with the measurements of the twin nucleation and migration stresses. The measurement of the stress required to initiate slip is analyzed separately in Section 1.3. High resolution strain measurements were also used to capture the strain changes across grain boundaries (GBs) on FeCr polycrystal (Section 1.4), the same section also provides the details of the strain averaging process. Finally, section 1.5 describes the slip and twin indexing calculations using grain orientations from EBSD and slip/twin traces on the sample surface.

1.1. Digital Image Correlation

DIC is a non-contact methodology for measuring local displacements on a flat area of the sample surface. The extension of the analyzed area depends on the research purposes that indicate the image resolution required (macro-scale, meso-scale, micro-scale, nano-scale), on the type of strain measurements (real time or out of the load frame), on the available experimental set-up (lens, camera), and on the preparation of the surface. The technique is based on reproducing on the target surface a random *speckle pattern* which results in a groups of pixels on the grey scale (from 0 to 255) in the images captured with a monochrome digital camera. This speckle pattern can be produced using different methodologies, in particular its preparation depends on the resolution adopted for the images. For example, it is possible to obtain the speckle pattern painting the sample using a commercial airbrush and a black paint. In other cases for which higher image resolutions are required (i.e. for measuring the strain localization produced by slip) a different procedure for

generating the speckle patterns is used. The ability to generate the correct speckle for the required application in terms of image resolution is the critical point of the DIC methodology.

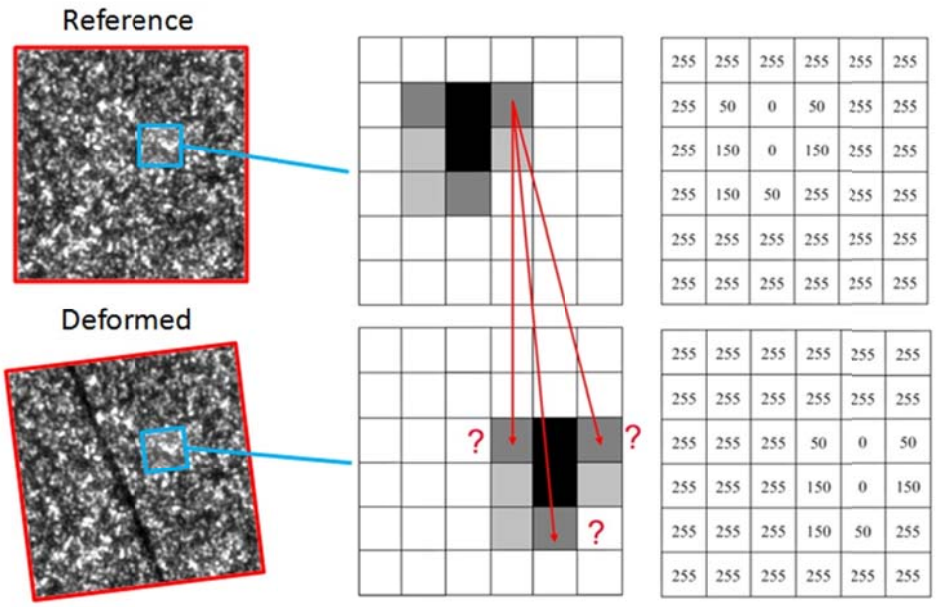

Figure 1.1. DIC technique is based on the recognition of the position of a subset of pixel on the deformed image, it is not possible to track one single pixel.

Figure 1.1 shows an example of a speckle pattern. The first *reference* image is captured on the virgin sample at zero load, while the *deformed* image represents the same area of the speckle pattern after the application of a load. In this case the pixels on the second images moved following the local deformation of the sample surface. The ability of the DIC algorithms resides in tracking the position of square groupings of pixels called *subsets*, since the position of the single pixel in the second (deformed) image is not unique. For example, as shown in Figure 1.1, for the first (reference) image more than one possibility exists for the pixel with value 50 in the second (deformed) image. The visual program used in this work (VIC 2D) contains adapted algorithms for defining the position of the subsets in the deformed image, thus allowing the definition of the vector displacement for the center of the subset (correlation point). In this work, with the adopted methodologies for the speckle deposition, are typically used subset sizes from 31 to 51 pixels for each edge of the square group of pixels. The length of the edge needs to contain a sufficient group of pixels which represents a defined marker that can be localized in the deformed image. It follows that the capability to increase the resolution of the images strictly depends on the quality of the speckle pattern, in particular on the mean size of the speckle features. In the present work is adopted a *random* speckle patter, which has been successfully used by different authors (see i.e. [66]), and it is considered better than a period grid pattern used in grid methods. Another important parameter for the correlation is the *subset spacing* which represents the number of pixels between each correlation point (center of the subset). Usually the typical subset spacing ranges from 5 to 10 pixels (in the present work is always

used 5 pixels). Repeating the process for different points inside the reference image determines the displacement field of the deformed image.

Along this work DIC is used in two different modalities:

- *In situ* DIC; the deformed images are captured during the experiment, the strain fields obtained represent a *real-time* strain measurement.
- *Ex situ* DIC; both the reference and deformed images are captured out of the load frame (at zero load), the strain fields obtained represent the residual strains that remain on the sample surface.

Digital image correlation is used to measure the evolution of local strains, *in situ*, on a full field basis [11, 12, 67, 68]. In addition to *in situ* DIC (sample under stress in the load frame), was also used higher resolution DIC strain measurements obtained *ex situ* (out of the load frame) for analyzing the local effect of slip and twinning. In the following sections are described the methodologies along with examples of the adopted speckles for both *in situ* and *ex situ* DIC.

1.1.1. In situ DIC

The typical experimental set-up for the implementation of in situ DIC is shown in Figure 1.2, in the schematic is described a tension experiment. The nominal strain is measured using an extensometer, and the strain signal is used to control the load during the experiment. An IMI model IMB-202 FT CCD camera (1600 x 1200 pixels) with a Navitar optical lens (the resolved resolution is about 3.0 μm/px) was used to capture the reference and deformed images. Using a dedicated software was possible to capture the images during the loading and un-loading steps at an arbitrary time interval. This DIC set-up is adapted for measuring increments of deformation, in situ DIC is also referred to be a real time strain acquisition technique. The speckle pattern for DIC was obtained using black paint and an Iwata Micron B airbrush. An example of the speckle pattern used for in situ DIC is shown in Figure 1.3, in this case is shown a compression sample. This speckle pattern allows to use a subset size of 51 px (4 μm/px).

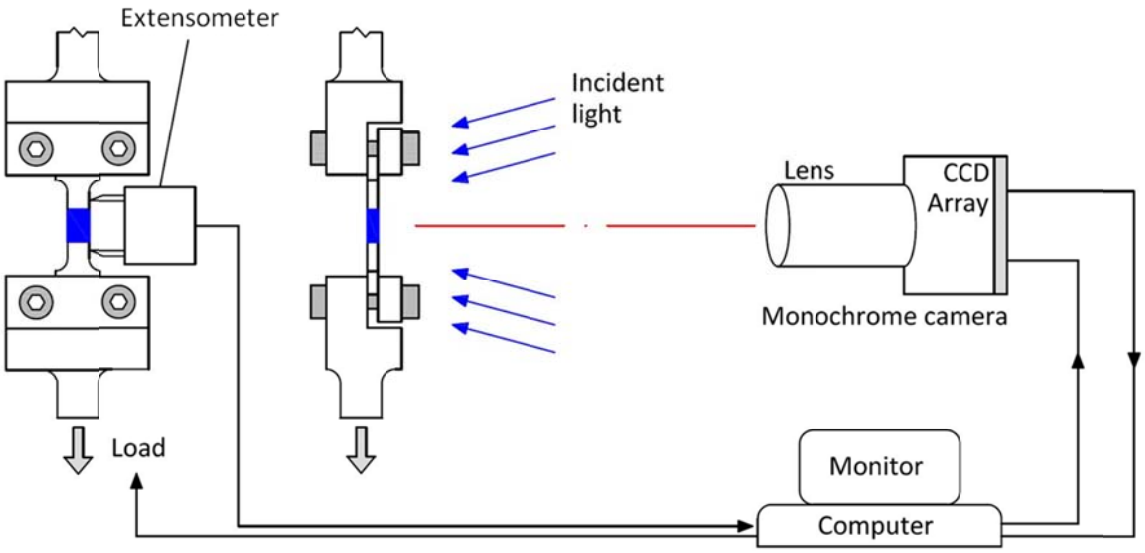

Figure 1.2. Experimental set-up for the in situ DIC methodology. The load frame and the camera are controlled by a central computer. A monochrome camera is used for capturing images during the experiment providing a *real time* image acquisition. The reference image is captured before the experiment at zero-load.

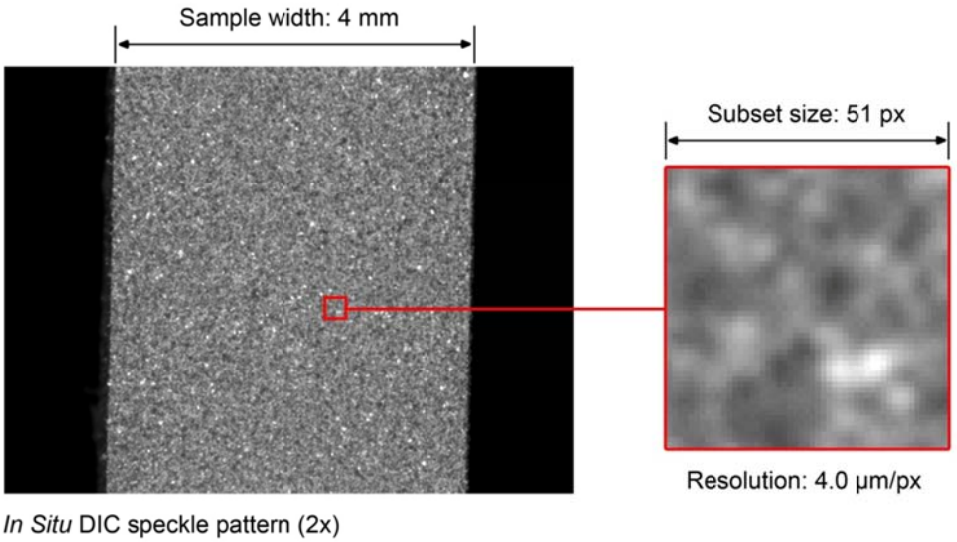

Figure 1.3. Image of the sample surface captured using an IMI model IMB-202 FT CCD camera (1600 x 1200 pixels) with a Navitar optical lens. The speckle patter is produced using black paint and an Iwata Micron B airbrush. The approximate subset size for the magnification adopted is 51 px (200 μm).

Typically, the speckle pattern generated with the airbrush is adapted for strain measurements on a 4 mm x 5 mm region (see Figure 1.3). Using this DIC set-up several applications can be implemented, for example crack closure measurements during fatigue [69], or similar studies on activated deformation mechanisms (slip/twin) for fcc materials [70]. In the present case, the selected DIC area allows to capture a significant portion of the surface involved in the deformation, and with the

adopted resolution strain heterogeneities derived from slip or twinning can be recognized (see as an example Figure 1.4).

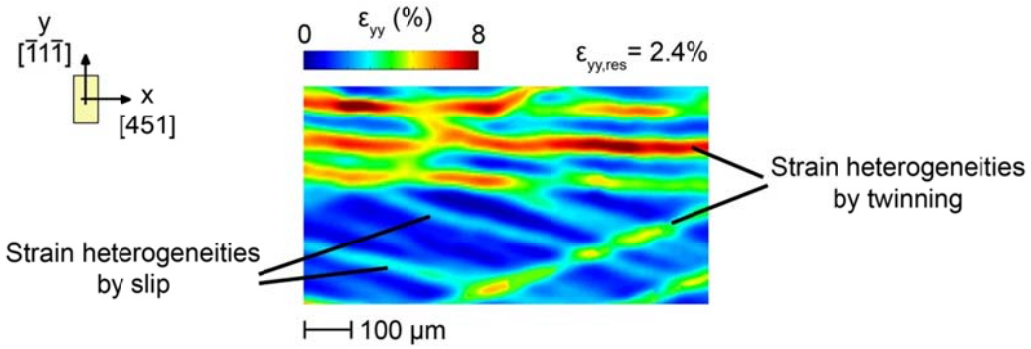

Figure 1.4. Strain heterogeneities introduced by slip and twinning. The local strains introduced by twinning are much higher than that of slip.

Finally, as deformation measurements via in situ DIC are made real time, the onset of slip, twin nucleation and twin migration can be evaluated using the full field strain contour plots obtained.

1.1.2. Ex situ DIC

For *ex situ* DIC, an optical microscope was used to capture the reference and deformed images. The microscope allows the images to be captured at a much higher magnification compared to the in situ images (2x versus 20x for *ex situ*). The increased imaging magnification improves the DIC measurement resolution (3.0 µm/pixel versus 0.44 µm/pixel for *ex situ*) [66] and enables better characterization of the local strain magnitudes that are associated with slip-grain boundary, twin-twin, twin-slip and slip-slip interaction regions.

The adoption of ex situ high resolution DIC provides the necessary strain field resolutions required when a local evaluation of the strain field is needed in order to study the particular effect of the interaction mechanism (slip/slip, twin/slip, slip/slip, slip/GB). On the other side, the usage of high resolution images (from a minimum resolution of about 1 µm/px) introduces more difficulties from the experimental point of view. First of all real time acquisition is partially excluded since with the increased resolution the covered region becomes smaller. It follows that during the experiment the target area can move out of the area covered by the camera because of the specimen moves due to the applied load. In this case the correlation cannot be implemented since the reference images are not found on the sequent deformed images. A second issue is schematically reported in Figure 1.5 and relates to the number of images to be acquired. Adopting ex situ DIC, for covering the entire net section of the tension sample, using the 5x set up (resolution 0.87 µm/px) 40 images are needed for covering all the surface of the sample. Increasing the image resolution (10x, resolution 0.437 µm/px), 40 x 4 = 160 images are needed in this case. If a further increment of the image resolution is needed

(20x, resolution 0.22 µm/px), a total of 160 x 4 = 640 images are required. So, when a high strain resolution is required, the number of images quickly increases with the adopted magnification. Moreover, further increments of the resolution limit the applicable loads since with high level of deformations the out-of-plane displacements (and potentially also the non-planarity of the surface) introduce a problem on maintaining a uniform focus of the image.

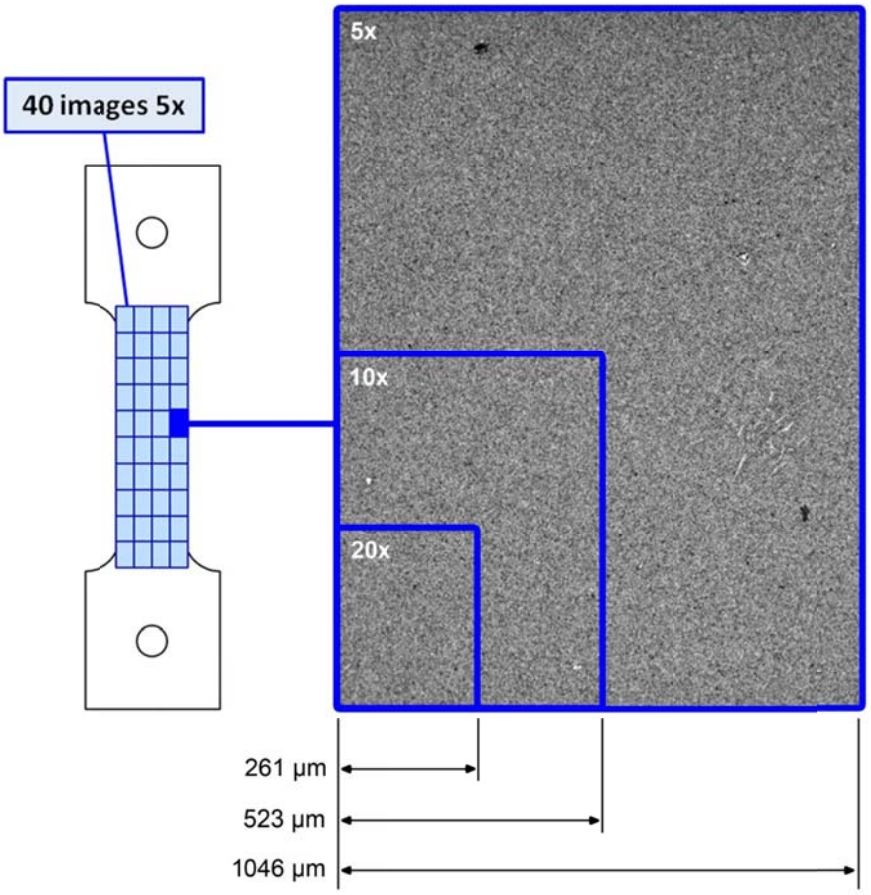

Figure 1.5. Image acquisition for ex situ DIC. The adopted speckle for ex situ DIC allow to use different optical microscope magnifications. The area of the tension samples can be covered stitching 40 images with a nominal magnification of 5x. In order to improve the strain field resolution is possible to cover the same area with 160 images (10x), while 640 images are needed with a further improvement of the resolution (20x).

An example of the speckle patter adopted for the ex situ DIC along this work is shown in Figure 1.6. The random speckle pattern is particularly adapted for images captured with a resolution of 0.44 µm/px. In the inset image of Figure 1.6 is also reported the typical subset selected for the correlations implemented with the adopted speckle. It is possible to notice that the features of the speckle are contained inside the subset, this is a first indication of the goodness of the correlation.

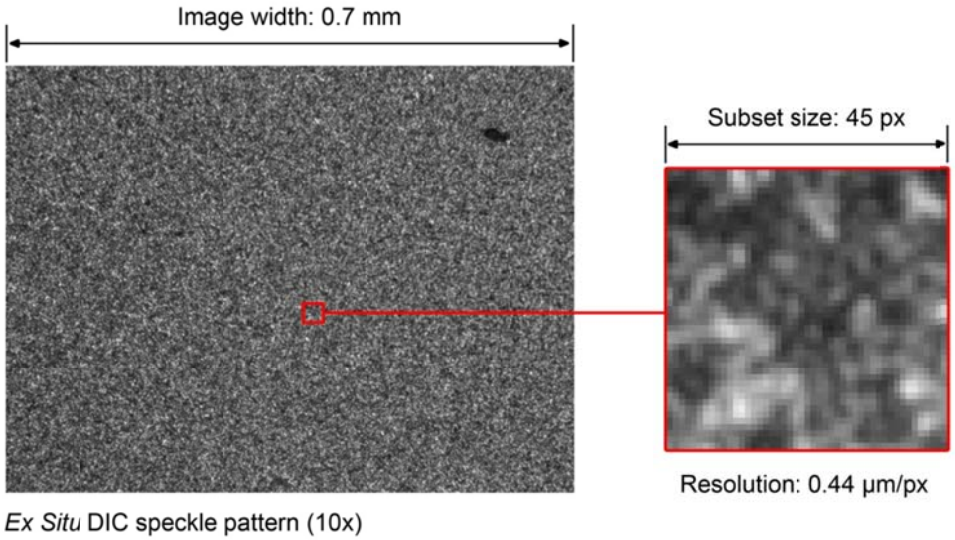

Figure 1.6. Image of the sample surface captured using an optical microscope (10x). The sample surface is used for the correlation providing a speckle pattern adapted for ex situ high resolution DIC. The approximate subset size for the magnification adopted is 45 px (20 µm).

1.1.3. *In situ* versus *ex situ* DIC

A simple comparison between the strain resolutions associated with is-situ and ex-situ DIC is shown in Figure 1.7. The strain fields reported refer to a static tension experiment on a single crystal with the loading axis oriented $[\bar{1}0\bar{1}]$. The strain field in the bottom represents the residual strain field for the central part of the sample. It is obtained correlating and stitching 5 images using the in situ set up (2.37 µm/px) captured at zero load. From this strain field, and from the associated region in the top-left, is possible to notice the strain localization due to slip on one main slip system. Strain measurements on the same region using ex situ DIC at the a resolution of 0.87 µm/px (5x) displays the same main slip system, in addition traces on a secondary slip system are detected. In this case, using the in situ set-up was not possible to clearly recognize the secondary slip system. It follows that the analysis of the strain fields obtained combining the results using different strain resolutions provided much more information than the adoption of only one set up. In particular using ex situ DIC strain fields is possible to define the strain introduced by different slip systems, and so localize all the possible activated slip systems. In situ, supported by the ex situ data, can be used to track the evolution of the strain associated with these slip systems during the deformation.

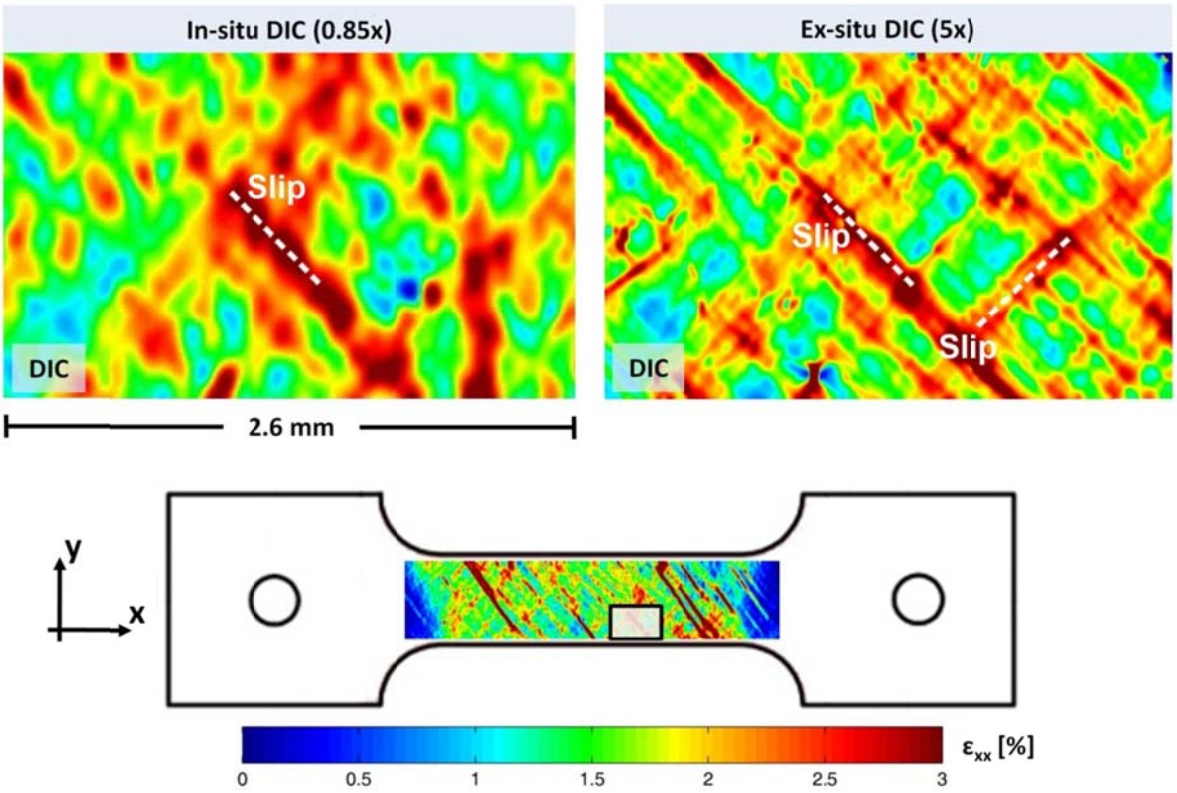

Figure 1.7. Comparison between strain fields displaying strain localizations due to slip obtained with in-situ DIC and ex situ DIC methodologies for a single crystal. The strain resolution obtained using ex situ DIC allows to correlate the strain field with each active deformation mechanism (slip or twin).

1.2. DIC application for measuring Twin Nucleation and Migration stresses in FeCr single crystals

As introduced in Chapter I, adopting in situ DIC in conjunction with EBSD, the mechanical behavior in terms of active slip and twin systems for different FeCr single crystal orientations was studied (see Chapter 2). Real time strain fields enable to capture the strain heterogeneities associated with slip, or twinning, during loading. In particular the application of this methodology for the selected single crystals allow to establish the points on the stress-strain curve where slip and twin nucleate, and follow the associated local strain evolution. The main advantage of using DIC relates to the possibility to quantify the local strain values associated with the deformation mechanisms. Typically, for bcc materials twin nucleation can also be identified on the stress-strain curve when a load drop occurs. In some cases the load drop can occur even in the 'elastic' region of the stress-strain curve [23, 71]. It is always better to verify the presence of twinned regions on the sample using for example EBSD, since for some bcc materials, under particular conditions, also slip nucleation can produce noticeable load drops [23]. In the following, all the crystal orientations displaying twinning have been successively analyzed using EBSD and, in some cases, also Transmission Electron Microscope (TEM). Moreover, as already described in the previous section, the local strains associated with slip and twinning are different. It follows that twinning can also be detected when a high local strain increment is measured following the load drop.

In general, depending on the alloy composition and in particular grain orientations, twinning can occur in conjunction with slip resulting in complex mechanical behavior which is difficult to detect and track with classical experimental approaches. For example, following twin nucleation at a critical resolved shear stress level (CRSS) τ^T, usually twin migration proceeds at a stress level τ^M which is lower [23]. Twin migration is also the result of twin-twin and twin-slip dislocation reactions occurring at twin boundaries. Experimental evidence of twin migration, supported by local strain measurements, can provide further insight for developments of bcc plasticity models, in particular on the hardening effect related to twin growth induced by twin/slip interactions. From the experimental point of view, measuring τ^T and τ^M requires local strain measurements and knowledge of the activated twin systems. The idea is to establish the twin nucleation and migration stresses using real time in situ strain measurements. In the following section are described the experimental details adopting incremental in situ DIC for correctly detect the τ^T and τ^M stresses.

1.2.1. Incremental Digital Image Correlation

The complexity of the strain fields when both slip and twin activate and provide strain localizations can be overcome using in situ *incremental* DIC. The idea is described schematically in Figure 1.8. In the schematic is represented a general stress-strain curve for a crystal orientation that displays both

slip and twinning deformation for a particular load direction. Along the stress-strain curve 5 points are marked. Each point refers to a particular image captured during the experiment. For example the point on the stress-strain curve marked as Image 1 refers to the point of slip onset. The correlation between the reference Image and the Image 1 enables to capture the strain localization due to slip initiation on the meso-scale.

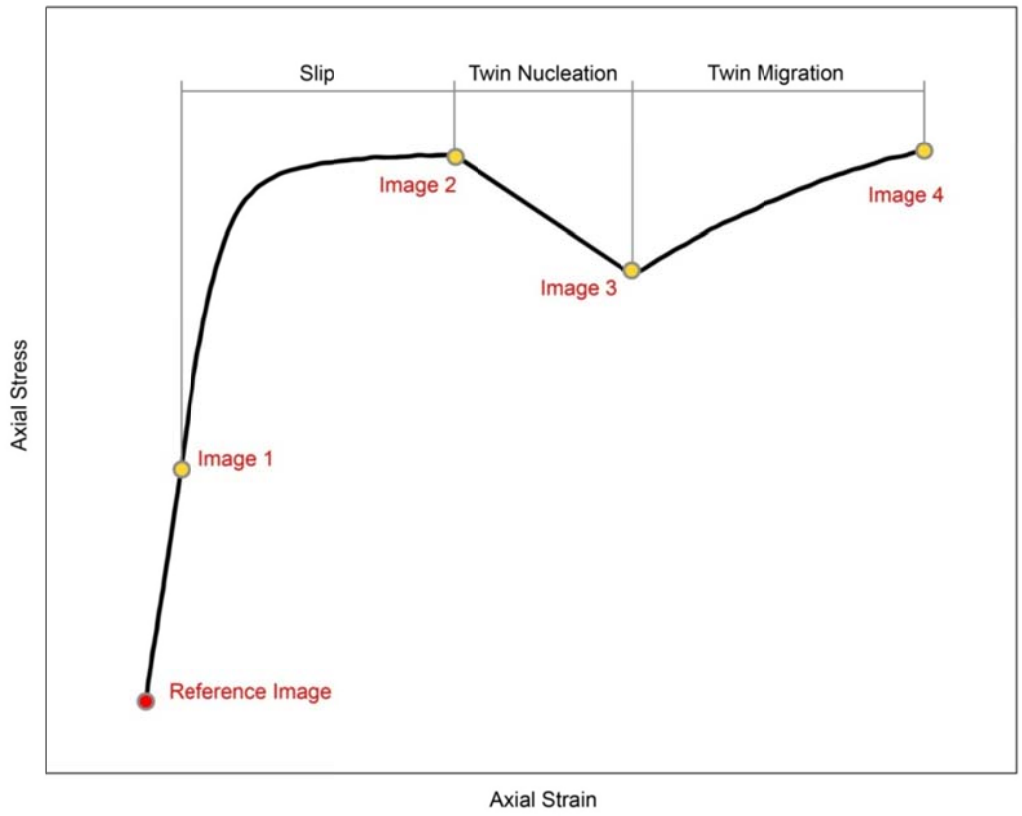

Figure 1.8. Schematic of the process for the identification of slip onset, twin nucleation and twin migration stresses using in situ DIC. Usage of different references image enables the characterization of the strain associated by each mechanism (see text for details).

Following the stress-strain curve, only one main slip system is active till Image 2. The correlation between the Reference Image with Image 2 quantifies the strain accumulation due to the active slip system. Twin nucleation occurs between Image 2 and Image 3. The subsequent correlation between the Reference Image with Image 3 provides the strain field in which the local strain contributions are provided by the strain fields of both slip and twinning. In this cases is useful to separate the strain contributions due to slip and twinning. *Incremental* DIC is implemented correlating two images along the stress-strain curve using as the reference image the point of slip or twin nucleation. In this case for example, the correlation between Image 2 and Image 3 enables to emphasize only the contribution of twin nucleation on the strain field, thus neglecting the contribution of the slip developed till Image 2. An example of strain fields obtained using incremental DIC is reported in

Figure 1.9 in which incremental DIC displays twin migration. The stress-strain curve introduced in Figure 1.9 refers to an experiment on a compression sample $[\bar{1}0\,\bar{1}]$ oriented. This crystal orientation displays both slip and twinning (for more details on this crystal orientation see Chapter 2). The inset marked A displays the strain field due to the activation of one slip system. Proceeding along the stress-strain curve, the resolved shear stress τ^T indicates nucleation of twins on two systems. Incremental DIC is used in this case to detect twin migration. The inset strain field marked B-B^i indicates that between point B and point B^i there is a strain accumulation in a region different than the localized strains detected on the inset strain field A. It follows that the strain accumulation measured correlating point B and point B^i indicates increment of local strains on the previously nucleated twins at τ^T.

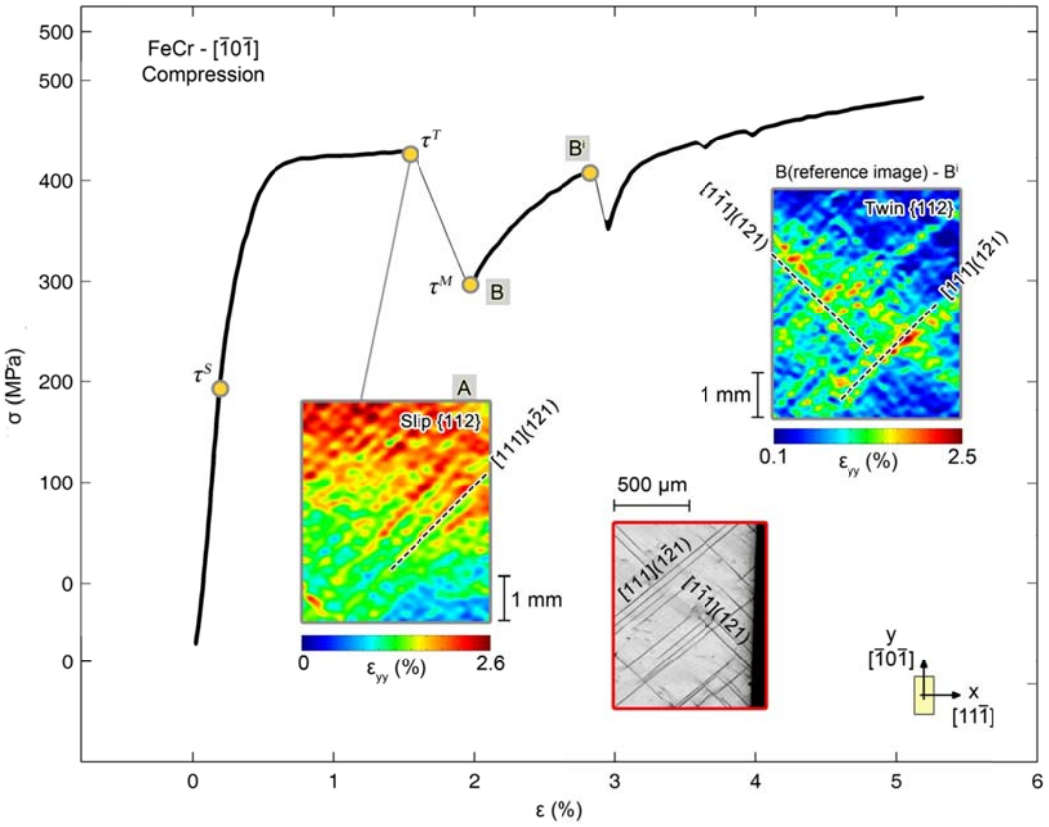

Figure 1.9. Stress-strain curve and in situ DIC strain measurements for $[\bar{1}0\,\bar{1}]$ orientation in compression. The inset image marked A shows the localized strains due to twin nucleation occurred at τ^T (twin systems $[1\,\bar{1}1](121)$ and $[111](1\bar{2}1)$). Incremental DIC (inset image marked B - B^i) is used to show twin migration τ^M, the correlations was implemented using the image B as the reference.

1.3. Slip onset in FeCr single crystals

Other important results using both the in situ and ex situ DIC on the single crystal samples cover the characterization of the slip onset. Different DIC image resolutions can be used for establishing the

critical resolved shear stress for slip onset τ^S. Along this work, ex situ DIC was adopted since high resolution images are required to capture the strain localizations developing from the initial slip traces formed on the sample surface. As previously described, ex situ DIC is not a real-time strain acquisition since the image acquisition process is obtained out of the load frame. At the same time, the estimation of the point of slip onset requires higher image resolution than the typical ones available with the in situ set-up.

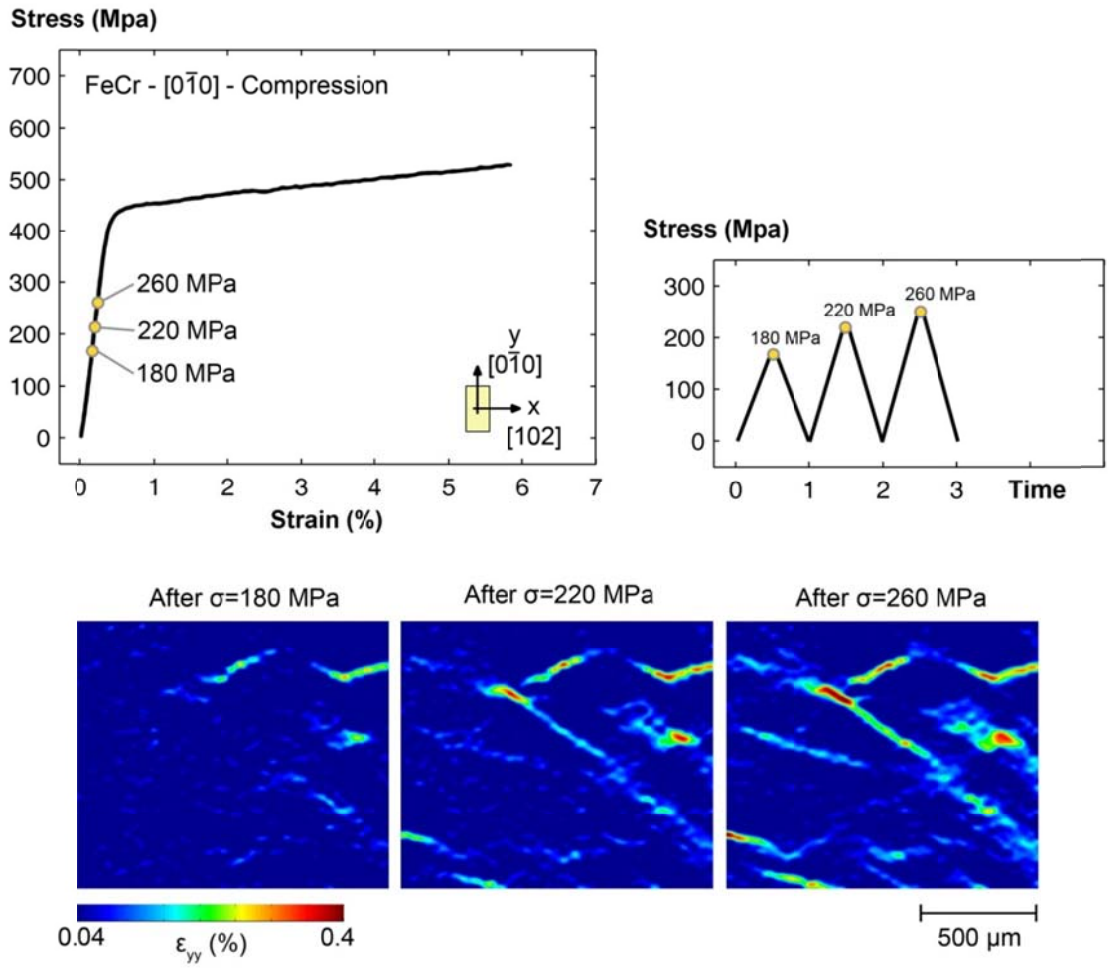

Figure 1.10. High resolution DIC strain fields (5x) obtained after loading the sample at three different load stages. High resolution images allow to capture the residual strain field after each load stage allowing to estimate the stress required to initiate slip. The images are acquired *out of the load frame* using an optical microscope.

The solution adopted in the following is to use ex situ DIC implementing different small load steps on the elastic region of the stress-strain curve (Figure 1.10). In this way is possible to estimate the interval of stresses between which slip initiates. The example reported in Figure 1.10 refers to the $[0\bar{1}0]$ crystal orientation in compression. One side of the sample has been prepared for ex situ DIC, and a fine speckle has been deposed on the target surface. 40 images of the target surface with a resolution of 0.87 µm/px (nominal 5x magnification) has been captured before the experiment (virgin

sample). Successively the sample was loaded in the nominally elastic region of the stress-strain curve at three maximum applied stresses (180, 220 and 260 MPa). The load was applied in three different steps, and after each load stage all the 40 (deformed) images of the target surface have been acquired. In the Figure 1.10 is reported the resulted residual strain field of the same region displaying traces of strain localization due to the activation of slip. We consider the stress required for slip onset between the values of 180 and 220 MPa.

1.4. Strain fields from Grain-Boundary - Slip interaction

1.4.1. Strain accumulation on FeCr grain boundaries

In this work, the strain measurements across the grain boundaries are used to characterize the slip transmission process. All the results presented in Chapter 3 refer to strain fields obtained using ex-situ DIC. High resolution strain fields have been obtained for polycrystal samples in compression which allow to reach higher deformations than the tensile case. The experimental procedure for characterizing the strain fields from DIC with the microstructure data (grain orientations) from EBSD is reported in [66], and schematically depicted in Figure 1.11. The surface of the sample is polished using SiC paper (from P800 up to P4000), and a final polishing suitable for EBSD data acquisition is obtained using a vibro-polishing with colloidal silica (0.05 μm). Successively 4 indentation markers are placed at the corners of the selected area (first inset schematic in Figure 1.11).

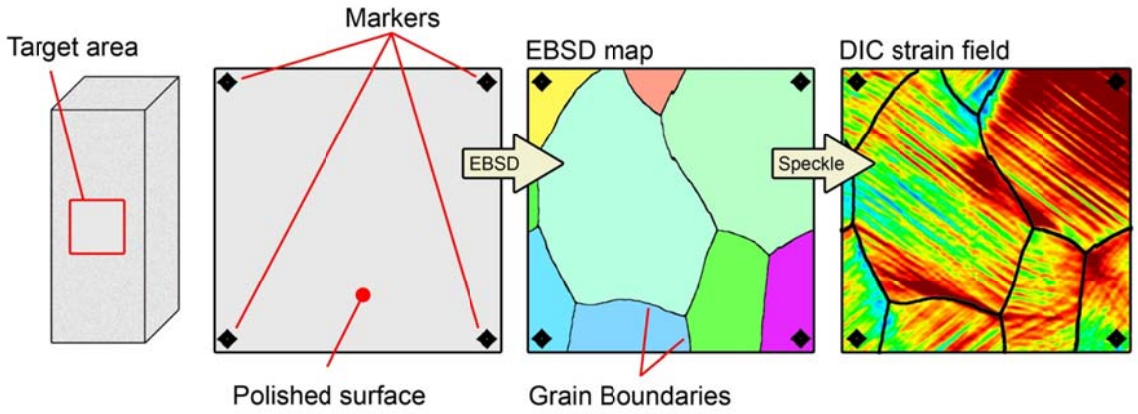

Figure 1.11. Experimental technique for the experiments on the FeCr polycrystal.

An EBSD scan of the selected area enables the characterization of the microstructure (second inset schematic in Figure 1.11), so the local grain orientation and the grain boundary morphology. Moreover, from the EBSD map is possible to recognize the position of the indentation marks. These markers provide the reference position for the overlap of the EBSD map with the strain data (third inset schematic in Figure 1.11). Successively a fine speckle patter has been applied on the sample surface and the experiment is carried out. Since from the images of the speckle pattern is possible to

detect the position of the indentation markers, the final overlap of the grain map with the strain field is obtained. This experimental approach has two main advantages. First of all knowing the grain orientation prior loading and the direction of the slip traces on the sample surface is possible to use the trace analysis for slip and twin indexing (see Section 1.5). Secondly, the overlap between the grain boundary map with the residual strain field enables to characterize the strain field across the grain boundaries which represents a critical aspect on the grain boundary characterization in polycrystal hardening.

Figure 1.12 shows an example of the local strains associated with the slip traces across a grain boundary. While with the approaches adopted in the literature (as shown for example in Figure 1.4b) was possible to characterize the reaction occurring at the grain boundary, no strain measurements are available with these techniques. The idea pursued here is to characterize the slip process through a measure of the strain gradient across the grain boundary, and relate this strain gradient with the result of the dislocation reaction. The idea is to show the possibility of the usage of the residual Burgers vector to predict the strain gradient at the grain boundaries, and so the contribution of the grain boundary to the material strengthening.

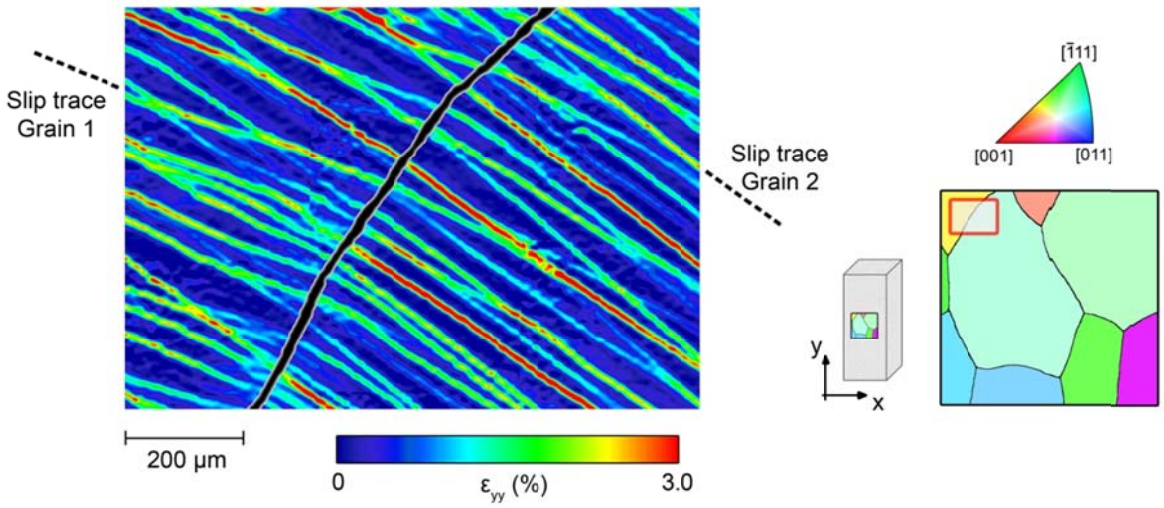

Figure 1.12. Strain field in proximity of a Grain Boundary. The strain measurements refer to the grain boundary reported in the EBSD map. The grain orientation determined from the EBSD data acquired allow the indexing of the slip systems and the correlation with the measured strain field.

Special codes for the calculation of the strains across the grain boundaries are adopted in this work. Figure 1.13 shows an example of such calculation. The strain field reported in Figure 1.13 is the same shown in Figure 1.12. The crystal orientation of the grains, and the grain boundary position were determined using EBSD. Successively the strain field obtained using high resolution ex situ DIC was overlapped at the EBSD map. The strain localizations along bands indicate the traces of slip on the surface. In order to establish the strain field across the grain boundary, and measure the strain

gradient across it, a rectangular selection of strain measurements are captured and averaged. Successively was determined the distance between the coordinates of the central point of the rectangular selection and the grain boundary. The minimum distance between the averaged strain measurements and the grain boundary is represented by half of the length of the rectangular selection side (perpendicular to the grain boundary), avoiding to include in the strain measurements for the Grain 1 some points belonging to Grain 2.

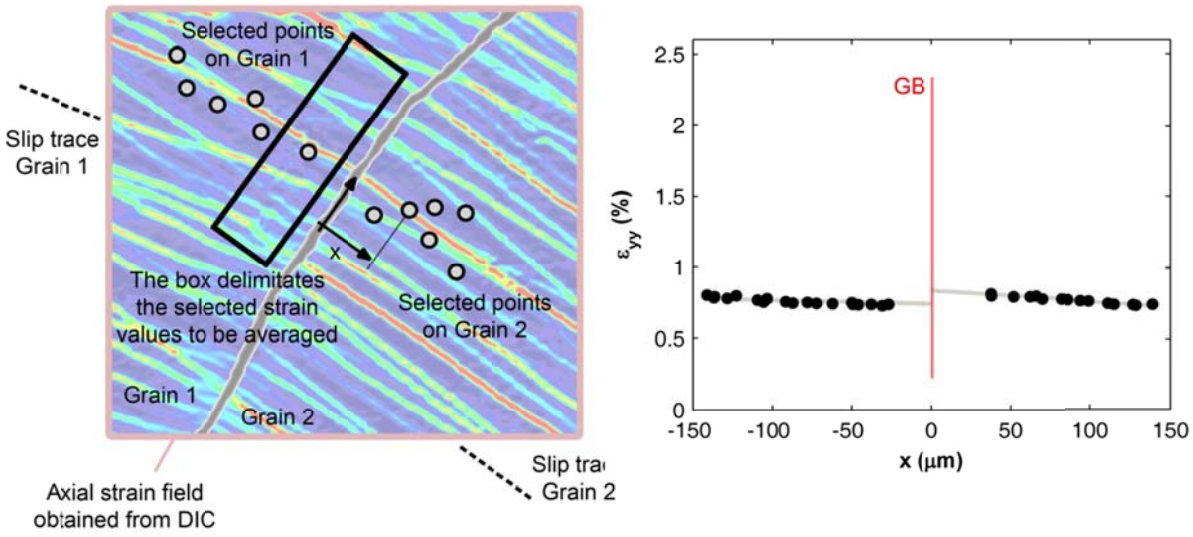

Figure 1.13. Strain measurement methodology for the calculation of the strain magnitude associated with the incoming slip system approaching the Grain Boundary for the case reported in Figure 1.12. The black box represents the selected region on the DIC strain fields. All the experimental strain values contained in this box are averaged, and the final value is plotted versus the distance from the grain boundary determined between the center of the rectangular selection and the point on the grain boundary determined projecting the center of the selection on the grain boundary.

The final plot obtained averaging the strains across the grain boundary is reported in Figure 1.13. In this case the strain values approaching the grain boundary are similar, a full strain transmission case is detected. In Chapter 3 are also derived the dislocation reactions for the estimation of the residual Burgers vector magnitudes. These information help in understanding the strain plot obtained, thus allowing to derive important considerations on the role of the residual Burgers vector on the slip transmission process.

1.4.2. Strain accumulation on TiAl

Strain accumulation on TiAl samples is studied following the same experimental approach depicted in Section 1.4.1 (Figure 1.11) for FeCr polycrystal samples. Figure 1.14 shows the application of the same experimental approach for the TiAl experiments. Due to the fine microstructure and the

complexity induced by the presence of two intermetallic phases, the usage of EBSD is rather complicated.

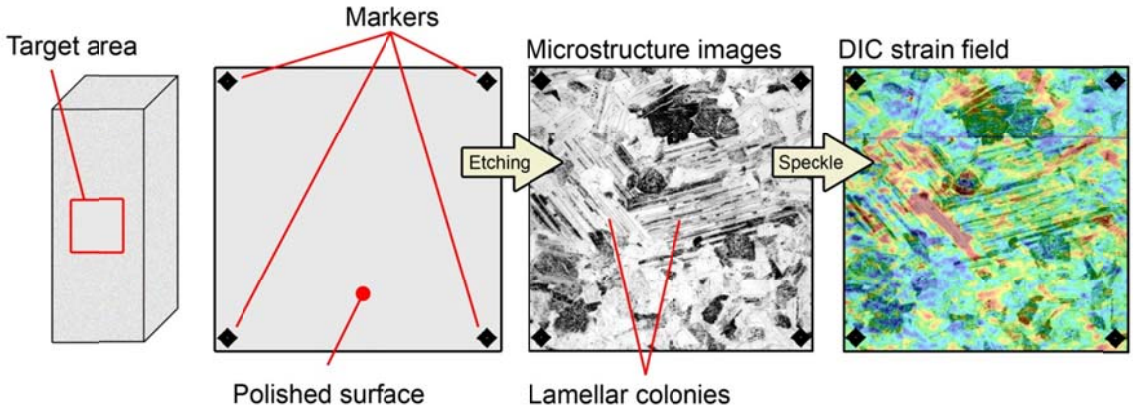

Figure 1.14. Sample preparation for TiAl experiments. 4 indentation markers are placed at the corner of a selected area of the sample surface after polishing. Successively the surface is etched and a set of images using an optical microscope is captured in order to characterize the material microstructure of the selected area.

The microstructural characterization is so implemented etching the polished surface in order to visualize with an optical microscope the two main microstructures present: the lamellar colonies and the equiaxed grains. For details on the solution composition for the etching see [72]. This procedures enables to easily characterize large samples areas which can be successively analyzed using high resolution DIC.

1.5. Slip and twin indexing

Along this work, indexing of slip and twin systems is obtained using the crystal/grain orientations measured through EBSD and the slope of the slip/twin traces on the sample surface. Crystal orientation from EBSD is given with Bunge convention (angles φ_1, ϕ, φ_2) and provides the three rotations between the crystal frame and the sample frame. From rotation angles defined with the Bunge convention is calculated the rotation matrix *g* [73]:

$$[g]=\begin{bmatrix} \cos(\varphi_1)\cos(\varphi_2)-\sin(\varphi_1)\sin(\varphi_2)\cos(\Phi) & \sin(\varphi_1)\cos(\varphi_2)+\cos(\varphi_1)\sin(\varphi_2)\cos(\Phi) & \sin(\varphi_2)\sin(\Phi) \\ -\cos(\varphi_1)\sin(\varphi_2)-\sin(\varphi_1)\cos(\varphi_2)\cos(\Phi) & -\sin(\varphi_1)\sin(\varphi_2)+\cos(\varphi_1)\cos(\varphi_2)\cos(\Phi) & \cos(\varphi_2)\sin(\Phi) \\ \sin(\varphi_1)\sin(\Phi) & -\cos(\varphi_1)\sin(\Phi) & \cos(\Phi) \end{bmatrix} \quad (1.1)$$

The load direction is defined as $(\overrightarrow{RD})_{crystal}$: $[100]^S$, the normal to the reference sample surface (DIC sample surface) $(\overrightarrow{ND})_{crystal}$: $[001]^S$, and the tangential direction $(\overrightarrow{TD})_{crystal}$: $[010]^S$ (Figure 1.15).

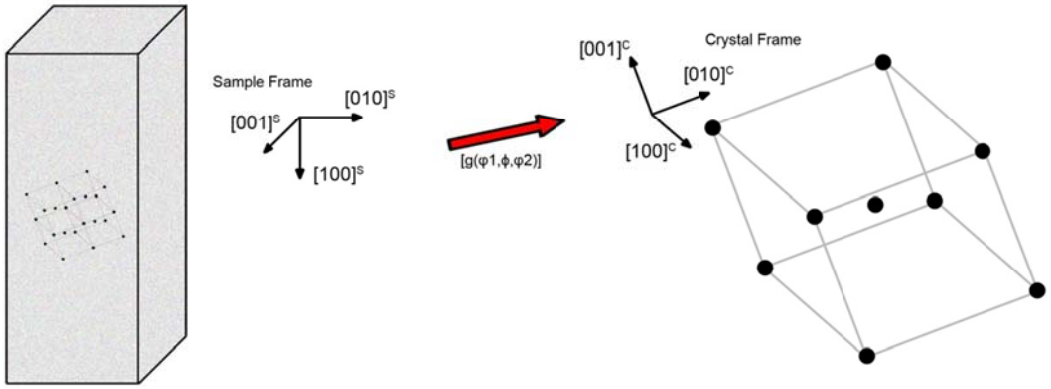

Figure 1.15. Schematic of the rotation matrix which relates the orientation of the sample frame with the orientation of the crystal frame.

Using the rotation matrix *g*, the crystal orientations on the sample frame $(\overrightarrow{RD})_{crystal}$, $(\overrightarrow{ND})_{crystal}$, $(\overrightarrow{TD})_{crystal}$ are determined as:

$$(\overrightarrow{RD})_{crystal} = g \cdot (\overrightarrow{RD})_{sample} \tag{1.2a}$$

$$(\overrightarrow{ND})_{crystal} = g \cdot (\overrightarrow{ND})_{sample} \tag{1.2b}$$

$$(\overrightarrow{TD})_{crystal} = g \cdot (\overrightarrow{TD})_{sample} \tag{1.2c}$$

In bcc materials, the most commonly observed slip planes in bcc materials are the {112}, {011} and {123} type, while twinning is restricted to the {112} family [54, 74]. In both twinning and slip the shear directions are from the <111> family. In order to index the slip/twin systems activated during the experiment, the slip/twin systems with the largest Schmid factors are selected: m^S for slip and m^T for twinning. $m^{T/S}$ are defined as

$$m^{S/T} = \cos(\lambda)\cos(\varphi) \tag{1.3}$$

in which λ is the angle between the slip direction and the tensile axis, φ the angle between the tensile axis and the slip-plane normal. Once established the *potential* active slip/twin systems based on Schmid factor analysis, the next step is to represent the selected slip/twin planes $(\overrightarrow{n_{\{abc\}}})_{crystal}$ (which are defined in the crystal frame) in the sample frame:

$$(\overrightarrow{n_{\{abc\}}})_{sample} = g^{-1} \cdot (\overrightarrow{n_{\{abc\}}})_{crystal} \tag{1.4}$$

Successively is determined the projection of the intersection between the slip/twin plane on the sample frame $(\overrightarrow{n_{\{abc\}}})_{sample}$ with the plane defining the analyzed sample surface $(\overrightarrow{ND})_{sample}$

$$(\overrightarrow{trace})_{sample} = (\overrightarrow{n_{\{abc\}}})_{sample} \times (\overrightarrow{ND})_{sample} \tag{1.5}$$

From equation 1.5 is obtained a vector which lies on the $(\overrightarrow{ND})_{sample}$ plane. This vector can be compared with the slip/twin traces experimentally observed on the sample surface (Figure 1.16).

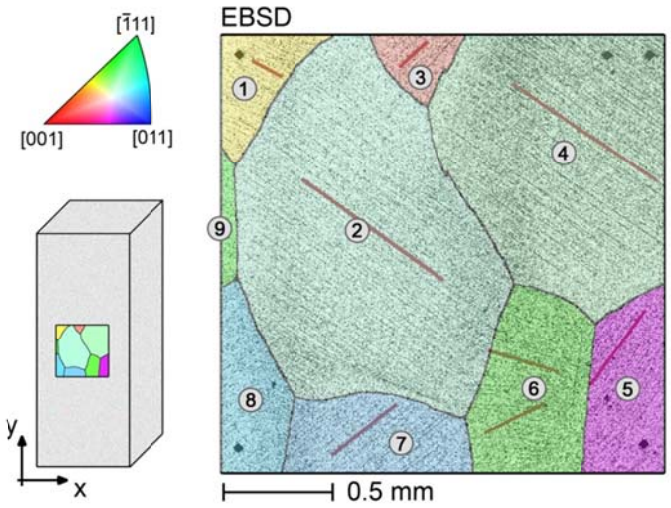

Figure 1.16. Slip traces on the sample surface which are compared with the projected slip planes (see text for details).

Chapter 2

Twin nucleation and migration in FeCr Single Crystals

Part of this work is published in [55].

In this Chapter are presented the results of the experiments on the FeCr single crystals implemented for understanding the mechanical behavior of bcc materials, focusing on the evolution of the deformation mechanisms (slip/twinning) during loading. The usage of single crystals allows to focus on specific grain orientations, and it avoids the complexity introduced by grain boundaries in polycrystals. In particular, the careful selection of the crystal orientations allowed to activate specific twin and slip systems. Different crystal orientations and loading directions have been tested, leading to a precise characterization of the strain fields due to the activation and interaction of twin and slip. Based on the type and number of active systems, different stress-strain curves are then expected (see schematic in Figure I.3).

In earlier works on Fe-47.8Cr alloy, Marcinkowski conducted indentation experiments and observed the presence of twinning and slip predominantly on <111>{112} systems [22]. Since it is not easy to identify the slip and twin systems coinciding with {112} planes by simple optical observations, DIC and Electron Back Scattering Diffraction are then used, as the combination of these tools facilitates this distinction. Indexing the twin systems with EBSD and measuring local strain fields allow to monitor the nucleation and evolution of both slip and twinning during deformation. In the following, particular emphasis is placed on the analysis of the deformation mechanism at the early stages of plasticity (either corresponding to first yielding or twin migration subsequent to the load drop). DIC was utilized at higher resolutions compared to conventional studies and provides micro scale resolution measurements and allows pinpointing strain localizations due to slip and twin activation. The characterization of the strain fields related to the active deformation mechanisms provides further insight onto the evolution of the deformation for bcc materials.

In this chapter are addressed the following main issues: (i) Depending on the crystal orientation, the precise determination of the critical resolved shear stresses (CRSSs) for twin (τ^T) and slip nucleation (τ^S), by pinpointing local strain disturbances using DIC. Therefore, are discussed the implications of these experimentally determined stresses with respect to the Schmid Law. (ii) Making a distinction

between twin nucleation τ^T and twin migration τ^M critical stresses. (ii) The interactions of twins, in particular their influence on the formation of large local strains and increase in hardening. (iv) The cases of slip-twin interaction, which leads to impedance of slip and ensuing strain hardening as confirmed with DIC results.

2.1. Experimental setup

2.1.1. Sample geometries

Single crystals of FeCr with a composition of 47.8 wt. % Cr were manufactured using the Bridgman technique in a He atmosphere. Tensile dog-bone shaped specimens with a 1.5 x 3 mm cross-section and a 10 mm gage length were electro-discharged machined (EDM) with the loading axis along the $[0\,\bar{1}0]$ and $[\bar{1}0\,\bar{1}]$ crystallographic directions (Figure 2.1).

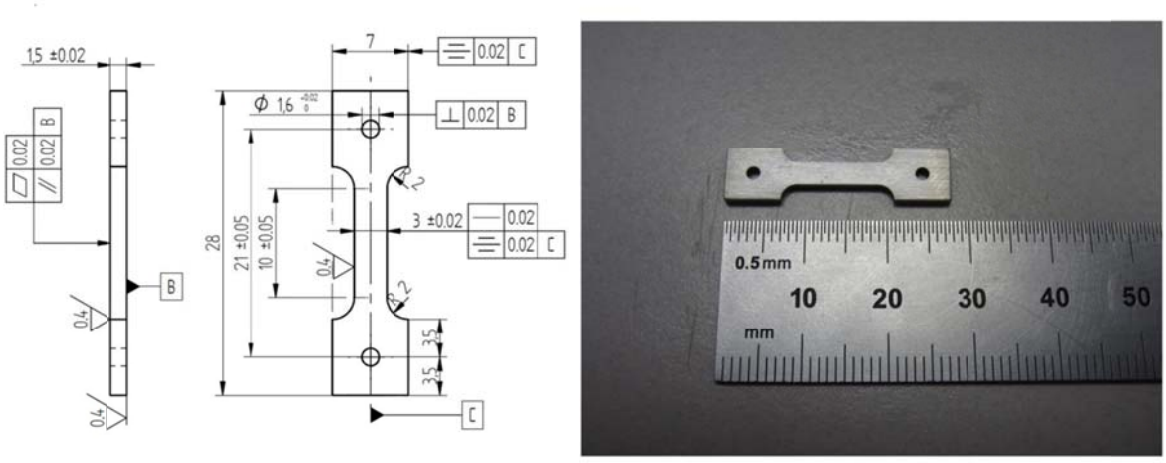

Figure 2.1. Sample geometry adopted for tension experiments. The samples were cut using Electron-Discharged Machining (EDM). The samples have a 1.5 mm x 3 mm cross-section and a 10 mm gage. The experiments were generally conducted on strain control.

Compression samples were also sectioned into 4 mm x 4 mm x 10 mm using EDM (Figure 2.2). The loading axis was normal to the $[\bar{1}0\,\bar{1}]$, $[\bar{1}1\,\bar{1}]$, $[0\,\bar{1}0]$, and $[314]$ planes and parallel to the 10 mm side of the sample. The crystallographic orientations in the other two directions, *i.e.,* across the width and through the thickness of each sample, were determined using electron backscatter diffraction (EBSD). Prior to loading, all samples were solution annealed at 900 ºC for 1h followed by a water quench.

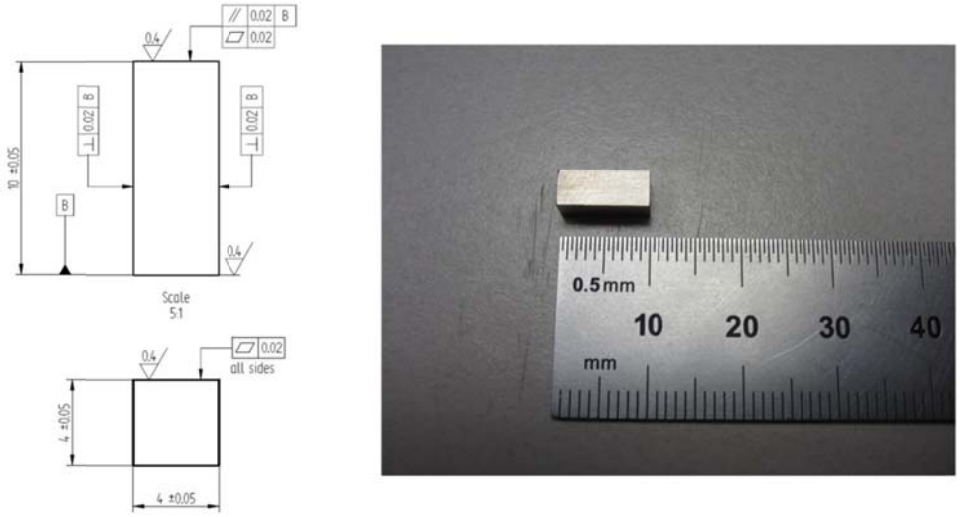

Figure 2.2. Sample geometry adopted for compression experiments. The samples were cut using Electron-Discharged Machining (EDM). The samples have a 4 mm x 4 mm cross-section. The experiments were generally conducted on displacement control.

The experiments were conducted at room temperature by means of a servo hydraulic load frame. Tension experiments were conducted on strain control, using a 5 mm gage length extensometer, while compression experiments were run in displacement control, both at a strain rate of $5X10^{-5}$ s^{-1}.

2.1.2. Digital Image Correlation setup

The work presented in this chapter is mainly based on experiments conducted using *in situ* DIC (see Chapter 1). The stresses necessary to nucleate slip and twinning were determined for different single crystal orientations using real time strain measurements. The resolution of the images captured using *in situ* DIC methodology was 2.5 µm/px. In Figure 2.3 are reported two examples of spackle patterns for a tension sample (Figure 2.3a) and compression sample (Figure 2.3b). The images refer to the samples before the experiment in the un-tested conditions. For the compression sample was used a lower resolution (tension: 2.40 µm/px versus compression: 3.94 µm/px) since the width of the sample for compression experiments is higher, and since during the test the width of the sample increases in case of compressive loads.

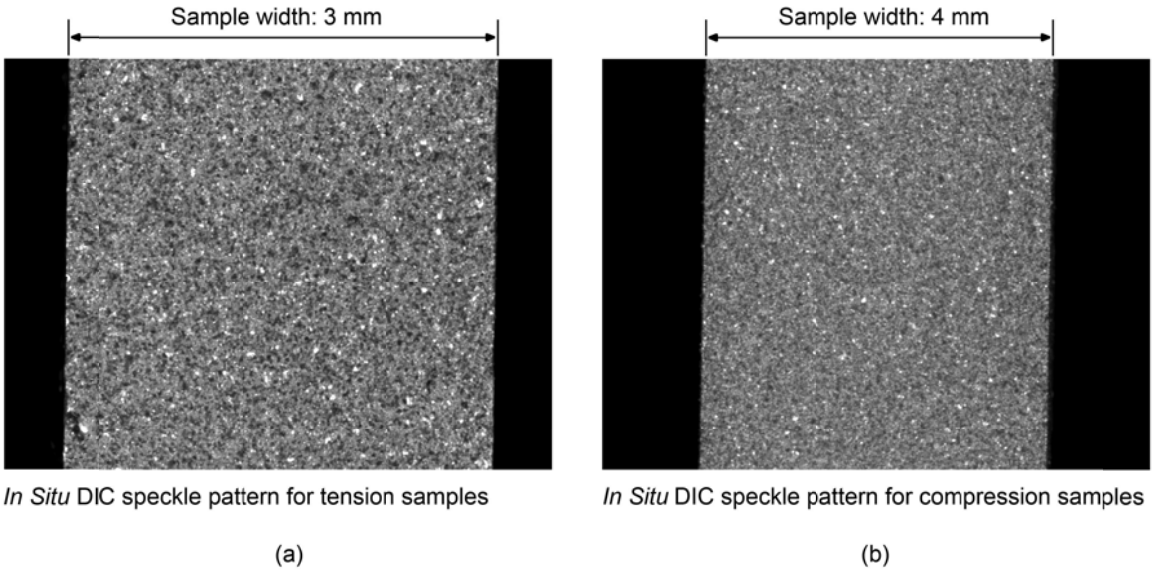

Figure 2.3. Reference images for the sample surfaces with speckle patterns produced using black paint adapted for in situ DIC: a) tension sample, b) compression sample.

2.2. Stress-strain curves

Table 2.1 provides a summary of the single crystal experiments conducted along with the number of samples tested for each combination of crystal orientation and load direction. For each case is successively presented the in situ DIC strain field which enables to characterize the strain evolution in function of the activated twin/slip systems.

Table 2.1. Crystal orientations and number of repeated experiments.

	Tensile		**Compressive**			
Axis	$[\bar{1}0\,\bar{1}]$	$[0\bar{1}0]$	$[\bar{1}0\,\bar{1}]$	$[0\bar{1}0]$	$[\bar{1}1\,\bar{1}]$	[314]
n° experiments	3	11	3	5	7	4

Figure 2.4 summarizes the stress-strain curves obtained from the selected crystals. A clear asymmetry between tension and compression behavior for the same crystal principally arises as a consequence of the unidirectionality of twinning [23]. Each twin system in the <11**1**>{112} family can be activated only with a compressive or a tensile load. For example, for the $[\bar{1}0\,\bar{1}]$ orientation two twin systems nucleate in compression in correspondence to the load drops, while reversing the load (tension) only slip is activated. More details on the possible twin systems activated based on the crystal orientation and on the load direction is provided in the next section.

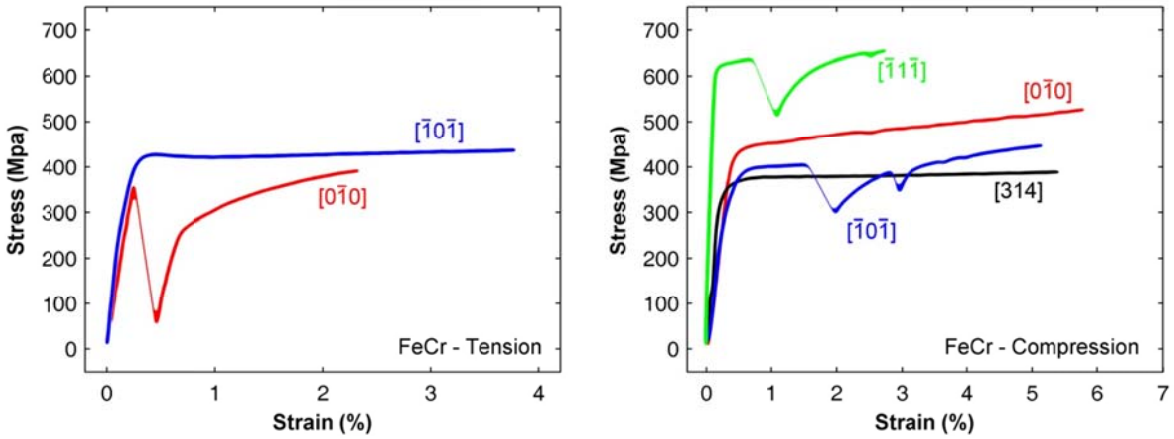

Figure 2.4. Summary of the stress-strain curves for different crystal orientations presented in this work.

Based on the results of the experiments (stress-strain curves in Figure 2.4) four general types of single crystal deformation behaviors are broadly classified (Figure 2.5). For *Case* I, twinning represents the main deformation mechanism and it initiates within the elastic region of the stress-strain curve. Twin-twin interactions govern hardening behavior for this case. In *Case* II the hardening behavior is governed by twin-slip interactions and twin nucleation is preceded by pronounced slip activity. *Case* III represents orientations with a limited number of activated slip systems (1 or 2 slip systems). Finally, *Case* IV represents the occurrence of multiple-slip systems (> 2 slip systems) with clear evidence of hardening. Examples of each one of the four cases will be given in the next sections along with the critical stress magnitudes, the activated twin/slip systems, and the DIC strain fields.

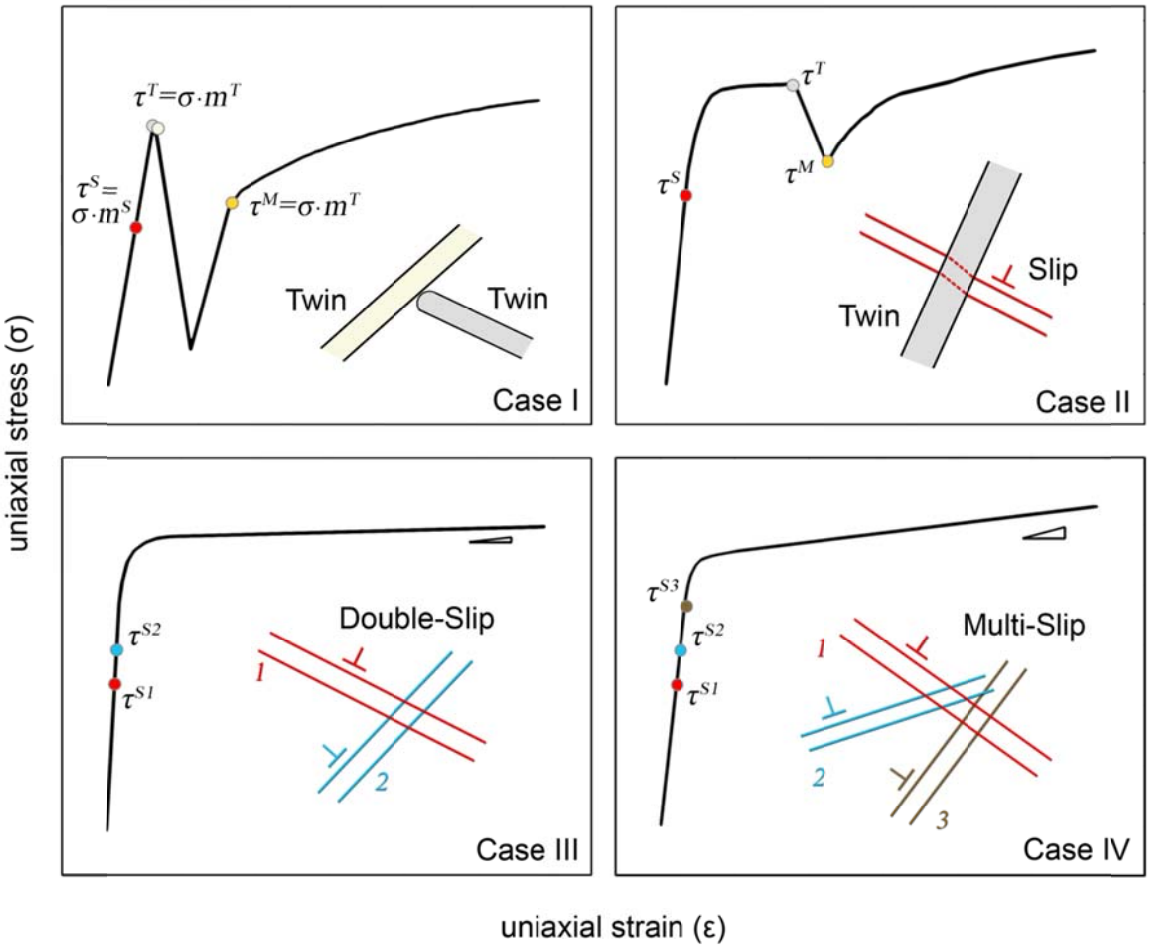

Figure 2.5. Schematic of the possible crystal deformation behaviors. The CRSSs for slip nucleation (τ^S), twin nucleation (τ^T) and twin migration (τ^M) are determined by multiplying the axial stress in the loading direction with the Schmid factors for the active slip (m^S) and/or twin (m^T) systems. Case I represents crystal hardening governed by twin-twin interactions. In Case II large slip activity precedes twin nucleation and twin-slip interactions dominate the hardening. Case III represents crystal orientations characterized by a limited number of activated slip systems. In Case IV multiple slip systems develop leading to crystal hardening.

2.3. Activated twin and slip systems

The most commonly observed slip planes in bcc materials are the {112}, {011} and {123}, while twinning is restricted to the {112} family. In both twinning and slip the shear directions are from the <111> family. The activation of certain twin/slip systems depends on both the crystal orientation and the loading direction (tension versus compression). One of the widely used approaches to establish the activated slip/twin systems is the calculation of the resolved shear stress on the slip/twin plane using Schmid Factors [75]: m^S for slip and m^T for twinning. $m^{S/T}$ are defined as

$$\tau^{S/T} = \sigma \cdot m^{S/T} = \sigma \cdot \cos(\lambda)\cos(\varphi) \tag{2.1}$$

in which λ is the angle between the slip direction and the tensile axis, φ the angle between the tensile axis and the slip-plane normal. Historically the Schmid law (equation 2.1) has been utilized for slip [75, 76] and twinning [40] in face-centered cubic (fcc) crystals, while for bcc slip deviation from the Schmid law is well known [74, 77, 78]. In these studies, the critical resolved shear stresses where determined on the atomistic scale, and the meaning of τ^S is the stress required for the dislocation gliding on a defined slip plane. The measurements of τ^S proposed in the following sections are derived from strain measurements, thus this study provides a set of results useful to check the Schmid law for slip on the meso and macro scales.

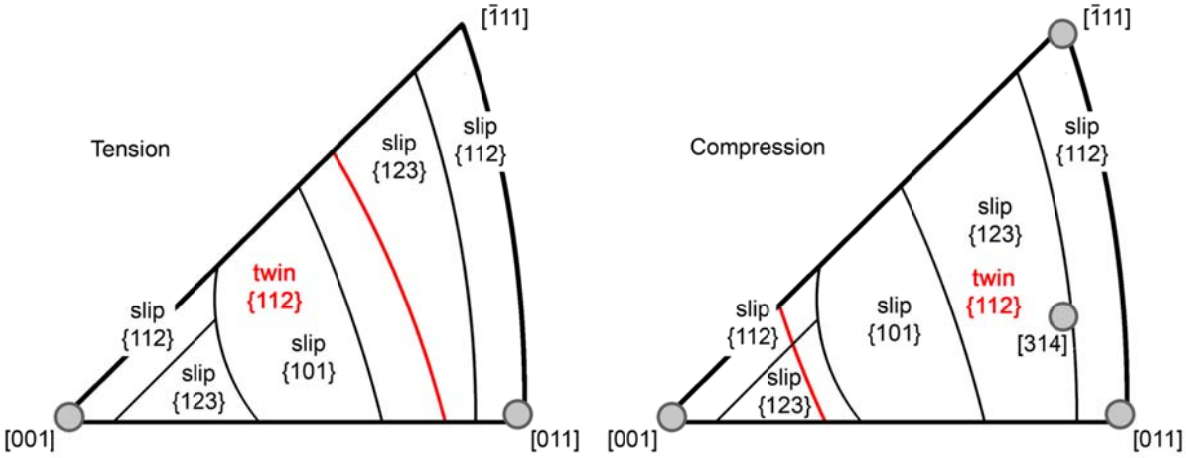

Figure 2.6. Stereographic triangles displaying slip and twin systems with largest $m^{S/T}$. Regions containing twin favored orientations are plotted considering the stress sign dependence for bcc twinning. The grey-filled points represent the crystal orientations tested in the present study.

Based on Schmid factor magnitudes the stereographic triangles in Figure 2.6 report the theoretical slip/twin systems for a bcc crystal structure. The distinction between tension and compression is necessary since bcc twinning, unlike slip, is uni-directional, i.e. there exists a unique sign of the shear stress direction (twinning direction) that leads to twinning [24, 79]. The red line in each of the stereographic triangles separates the regions in which the crystal orientations are expected to display twinning in addition to slip from regions where only slip is predicted. This line is defined based on the magnitudes of the $m^{S/T}$ for the possible twin and slip systems. In our analysis, the <111>{112} twin systems having m^T larger than 0.35 or, alternatively, much higher than the m^S for <111>{112} slip is used as a criteria to define the regions (red line) where twinning is expected.

Table 2.2 lists all the crystal orientations used in this work along with the theoretically possible slip and twin systems. The Axis column refers to the orientation of the crystal in the load direction of the sample, henceforth referred to as orientation. We report the theoretical slip/twin systems (column: Systems) displaying the highest magnitudes of $m^{S/T}$. Using this table it is possible to predict the activated twin and slip systems for the crystal orientations classified in the experimentally observed

Cases (schematic in Figure 2.5). For Cases I and II deformation via twinning is expected given the high m^T of the twin systems listed in Table 2.2. Crystal orientations belonging Case III display a limited number of slip systems with high m^S ($[\bar{1}0\,\bar{1}]$ orientation in tension and $[314]$ orientation in compression). Finally, we classify the $[0\bar{1}0]$ orientation in compression in Case IV as there are multiple slip systems with high m^S.

Table 2.2. Theoretical slip and twin systems for the crystal orientations analyzed in this work. For each crystal orientation are reported the slip/twin systems displaying the largest $m^{S/T}$.

1	2	3	4	5	6	7	8	9	10	11	12
$[1\bar{1}1]$	$[1\,\bar{1}1]$	$[1\,\bar{1}1]$	$[\bar{1}11]$	$[\bar{1}11]$	$[\bar{1}11]$	$[111]$	$[111]$	$[111]$	$[\bar{1}\bar{1}1]$	$[\bar{1}\bar{1}1]$	$[\bar{1}\bar{1}1]$
$(\bar{1}12)$	$(\bar{1}2\,\bar{1})$	$(21\,\bar{1})$	$(1\bar{1}2)$	$(12\,\bar{1})$	$(\bar{2}\,\bar{1}\,\bar{1})$	$(\bar{1}\bar{1}2)$	$(\bar{1}2\,\bar{1})$	$(2\,\bar{1}\,\bar{1})$	(112)	$(1\bar{2}\,\bar{1})$	$(\bar{2}1\,\bar{1})$

	Axis	Case	Slip System	Slip m^S	Twin System	Twin m^T
Tensile	$[\bar{1}0\,\bar{1}]$	III	2, 8	0.47	1, 3, 7, 9	0.24
	$[0\bar{1}0]$	I	2, 5, 8, 11	0.47	2, 5, 8, 11	0.47
Compressive	$[\bar{1}0\,\bar{1}]$	II	2, 8	0.47 0.47	2, 8	0.47
	$[0\bar{1}0]$	IV	2, 5, 8, 11	0.47	1, 3, 4, 6, 7, 9, 10, 12	0.24
	$[\bar{1}1\,\bar{1}]$	II	4, 8, 12	0.31	4, 8, 12	0.31
	$[314]$	III	2 $[1\,\bar{1}1](\overline{132})$	0.49 0.50	2	0.49

2.4. Crystal orientation $[0\bar{1}0]$

The crystal orientation $[0\,\bar{1}0]$ represents the classical *cleavage* orientation for the bcc lattice when the load is applied In tension [32]. The reason for this mechanical behavior along this crystal orientation is that there are four possible twin systems activated with a tensile load (see Table 2.2). Twin-twin interactions are geometrically studied based on the direction of the line which results from the interaction between the two twin planes. Along all the possible interactions between the four twin systems that can be activated for the $[0\,\bar{1}0]$ orientation, there are couples of interacting twins which have the direction of the intersecting line in the <011> family. The dislocation reaction between the twin partials for these family of interactions leads to the formation of a Cottrel dislocation [35, 80], which is the atomistic configuration leading to cleavage fractures.

2.4.1. Tension experiments

Figure 2.7 shows the stress-strain curve for the $[0\bar{1}0]$ crystal orientation tested in tension. The reported strains on the x-axis correspond to the DIC field averages, *i.e.* average axial strain (in the load direction) in the region covered by DIC. In the nominally elastic region of the stress-strain curve, high resolution DIC measurements indicate localized slip initiation. This can be clearly seen in the inset image marked A in Figure 2.7 (notice the high localized strains). Using the original crystal orientation, we project all of the possible slip planes (and twin planes) onto the sample's surface (for more details see Section 1.5). For the inset marked A, the strains localize in bands with a slope that matches the trace of the $[\bar{1}1\,\bar{1}](121)$ slip system with $m^S=0.47$. The stress level at which these localized strains appear marks the onset of slip $\sigma^S=181\ MPa$. With knowledge of the stress at the onset of slip and the activated slip system (from trace analysis), the resolved shear stress at the onset of slip is $\tau^S=85\ MPa$ (equation 2.1).

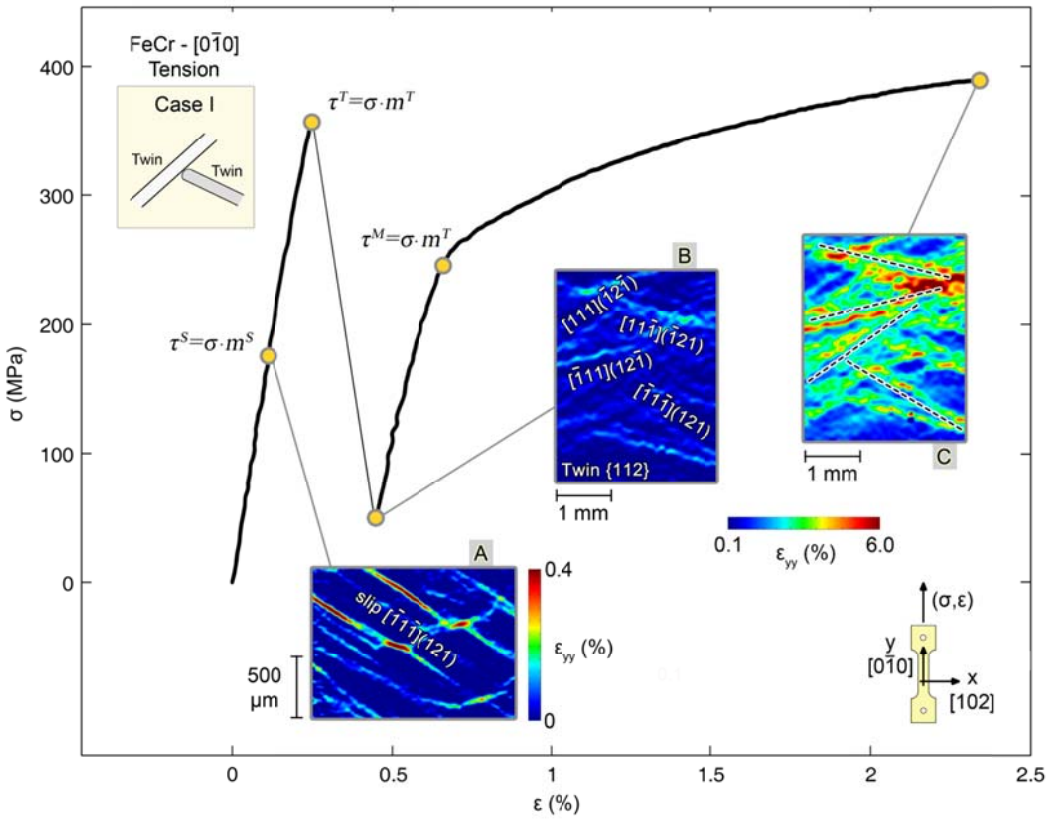

Figure 2.7. Stress-strain curve and DIC strain measurements for $[0\bar{1}0]$ orientation in tension (Case I). The inset image marked A shows localized strains due to onset of slip. Proceeding along the stress-strain curve the load drop indicates twin nucleation at τ^T. The inset image marked B displays localization of strains due to the nucleation of four twin systems in the $<111>\{112\}$ family. Twin migration starts at τ^M and produces the local strain increments visualized in the inset image marked C in the same regions (bands) formed at τ^T.

With continued loading, a stress level is reached where a pronounced and instantaneous load drop is observed (σ^T=*373 MPa*). This load drop is associated with twin nucleation. Full field strain measurements show high strain localizations in four bands (inset marked B in Figure 2.7), using trace analysis the activated twin systems are identified. All the activated twin systems have the same $m^T=0.47$, and the critical resolved shear stress for twin nucleation is obtained as $\tau^T=177\ MPa$. Following the load drop associated with twin nucleation, the material appears to deform elastically as shown by the second linear region of the stress-strain curve in Figure 2.7. With additional loading, plastic response is observed at a stress that is *lower* than the stress reached prior to twin nucleation. The strain accumulation beyond this point takes place in the same regions (bands) that were linked to twin nucleation (inset market C, Figure 2.7). The strain level increases as well as the width of the bands. These observations indicate that the plastic response may be dominated by twin migration. Consequently, the onset of twin migration $\tau^M=114\ MPa$ (Figure 2.7) is marked as the stress level at which plastic strains start to accumulate in the same bands that formed following twin nucleation.

Twin migration is also observed for the same $[0\bar{1}0]$ orientation using ex situ DIC strain fields. Figure 2.8 shows five strain fields representing the residual axial strain after each load step. The images were captured using the camera *in situ*, so the sample was in the load frame. They are considered *ex situ* DIC strain fields since the sample was at zero load, and each strain field was obtained stitching 5 images captured moving manually the microscope used for monitoring the surface of the sample during the experiment.

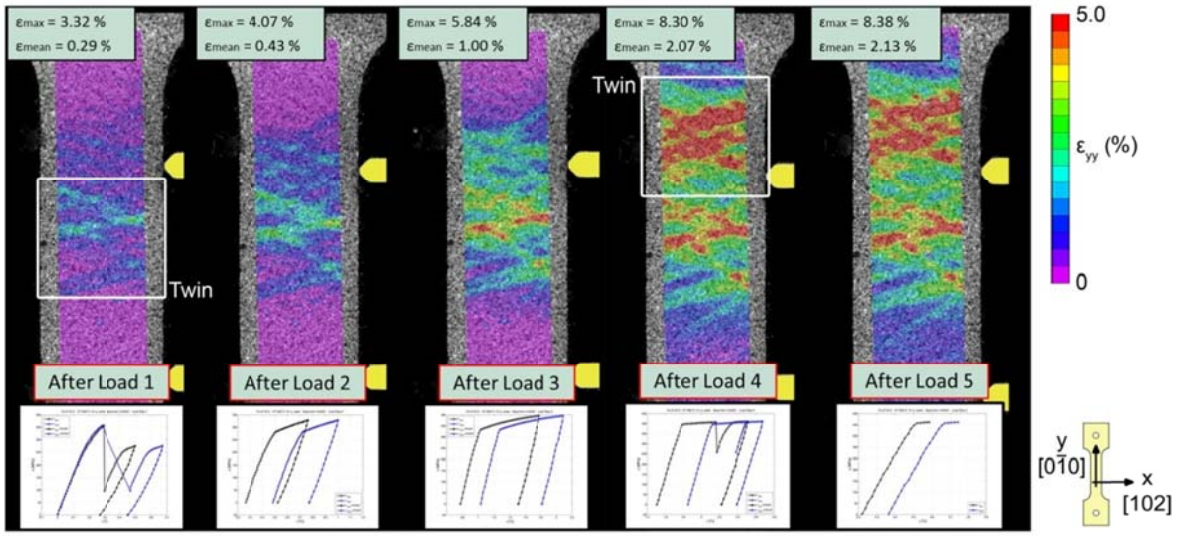

Figure 2.8. Local strain field on the $[0\bar{1}0]$ tension sample after each load step using ex situ DIC. In the stress-strain curves on the bottom of the strain fields is reported with black color the strain measured using the extensometer, while blue colored line refers to the strain measured using DIC (average strain on the DIC region).

The twins nucleated after the load 1 (first strain field in Figure 2.8) display progressive increment of the strains along the same bands formed after the load drop. Other twinned regions formed in a different sample location during load 4 (top area of the sample surface, see white box in Figure 2.8). The determination of the activated twin and slip systems using high resolution DIC was confirmed through EBSD measurements and SEM images. Figure 2.9 reports post-experiment EBSD data of the local crystal orientation for a 400 μm x 200 μm region on the sample's surface. The red-colored field represents the orientation of the matrix (very close to the original crystal orientation). Blue and green points indicate regions displaying a different crystal orientation. For both regions, the misorientation with the matrix is about 60°, this indicates that the regions are twinned. The slope on the observed twins matches with the traces of $[11\bar{1}](\bar{1}21)$ and $[\bar{1}11](12\bar{1})$ twin systems.

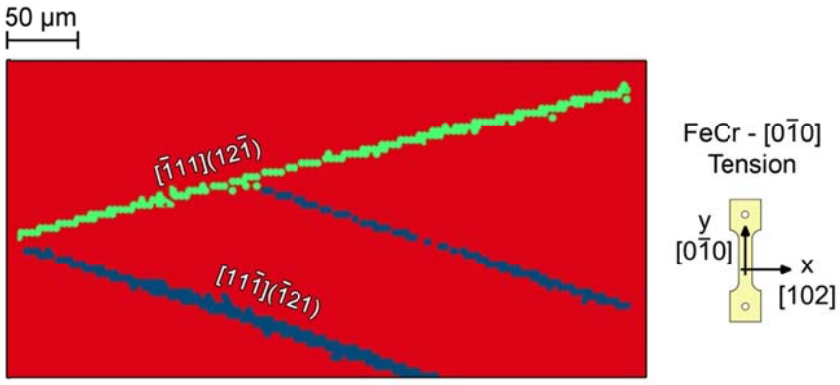

Figure 2.9. EBSD data for $[0\bar{1}0]$ orientation in tension (*Case* I). The EBSD data represent a 400 μm x 200 μm region on the sample's surface. Red-colored points indicate the crystal orientation of the matrix. Green and blue points indicate, respectively, $[\bar{1}11](12\bar{1})$ and $[11\bar{1}](\bar{1}21)$ twin systems as these two regions show a misorientation (with respect to the matrix crystal orientation) of about 60°.

In addition the trace of the activated twin and slip for the $[0\bar{1}0]$ orientation can be detected using the SEM as shown in Figure 2.10. Both of these observations are in good agreement with the results obtained from the ex situ strain field and trace analysis previously reported in the inset images A and B in Figure 2.7. In particular both the twin-twin intersections shown in Figure 2.10a-d display cases of blockage of the incoming twin.

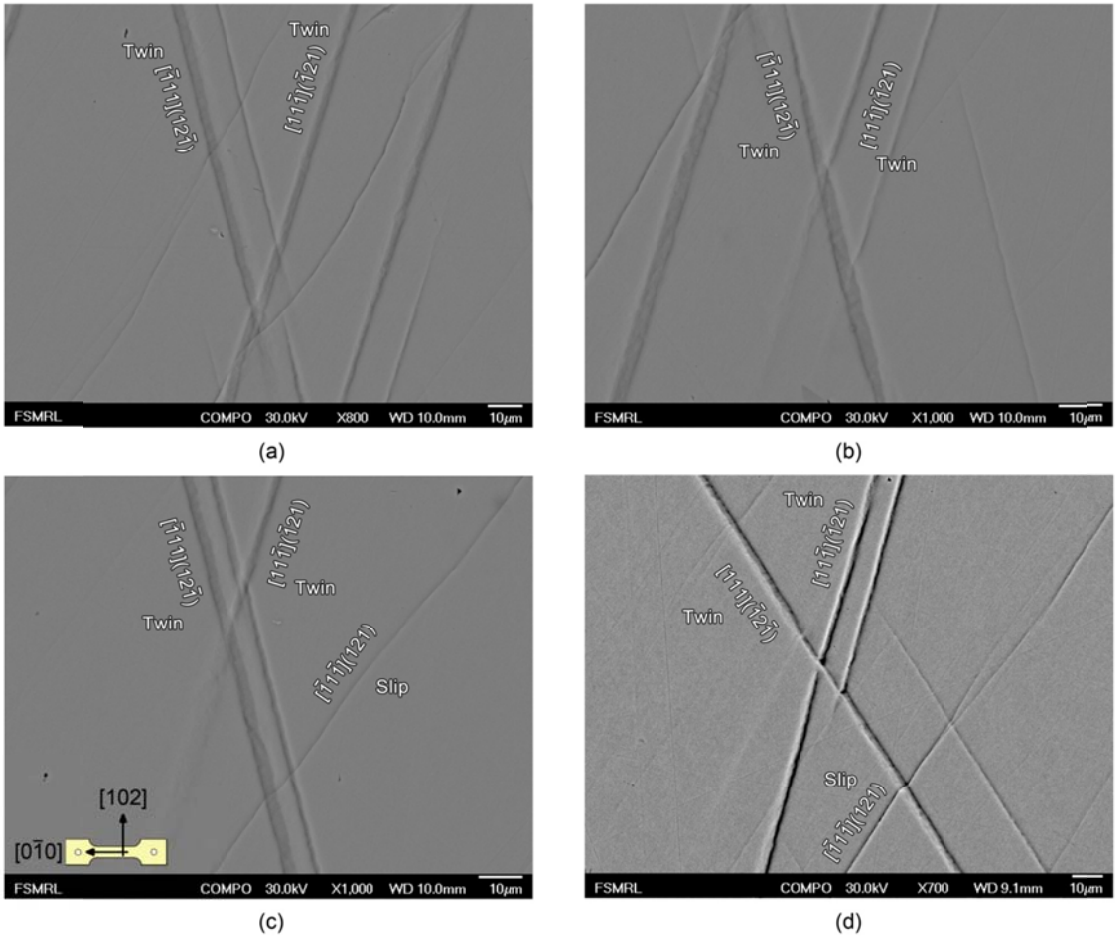

Figure 2.10. SEM image of twins in $[0\bar{1}0]$ orientation in tension. Each of the twin-twin intersections display blockage of the incoming twin.

2.4.2. Compression experiments

We classify the $[0\bar{1}0]$ orientation in compression as a multi-slip case (schematic in Figure 2.5) since there are four possible slip systems in the <111>{112} family with high m^S=0.47 (Table 2.2). The stress-strain curve for this crystal orientation displays a constant hardening (Figure 2.11). The inset image marked A represents the first evidence of strain localizations due to the activation of the $[111](\bar{1}2\bar{1})$ slip system at a CRRS of τ^S=85 MPa. Successively (inset image marked B), localized stain bands of the second slip system $[\bar{1}1\bar{1}](231)$ with m^S=0.46 appear. The in situ axial strain plot (inset image marked C, Figure 2.11) shows a direct evidence of the interaction between the two main slip systems involved in the crystal deformation. Moreover, the strain field displays strain bands oriented differently from the two main systems indicating the presence of other secondary slip systems involved, but not clearly visualized with the available DIC resolution. In this specific case, the slip systems involved lead to crystal hardening.

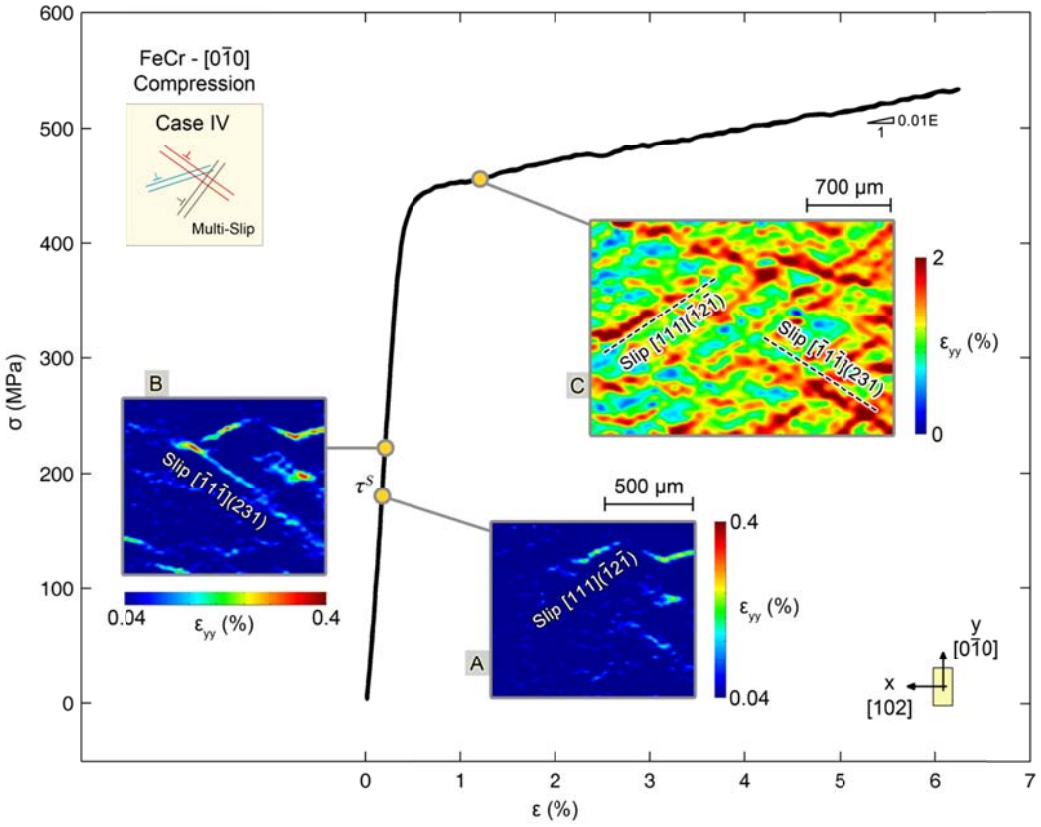

Figure 2.11. Stress-Strain curve and DIC strain field measurement for the $[0\bar{1}0]$ orientation in compression (*Case* IV). The inset images marked A-B illustrate, respectively, slip onset on the $[111](\bar{1}2\bar{1})$ and $[\bar{1}1\bar{1}](231)$ systems. The inset image marked C displays evolution of the strain field and slip-slip interactions.

2.5. Crystal orientation $[\bar{1}1\bar{1}]$

2.5.1. Compression experiments

Figure 2.12 displays the stress-strain curve for a $[\bar{1}1\bar{1}]$ oriented sample loaded in compression (*Case* II). High resolution DIC measurements (inset image marked A) reveal slip on the $[111](1\bar{2}1)$ system with $m^S=0.31$ at $\sigma^S=284\ MPa$, leading to a CRRS of $\tau^S=88\ MPa$. Slip on the same system accumulates up to $\varepsilon_B=1.07\%$ (inset image marked B). No traces of slip on other systems are observed. With the activation of only one single slip system, no significant hardening resulted as seen by the low slope of the stress-strain curve ($h=d\sigma/d\varepsilon=0.003E$). Proceeding with loading, we observe twinning nucleating with a stress drop. Three twins systems were activated at a critical stress $\sigma^T=646\ MPa$ leading to a CRRS for twin nucleation of $\tau^T=203\ MPa$. The inset image marked C displays the strain field after twin nucleation of the three observed twin systems $[111](1\bar{2}1)$, $[1\bar{1}\bar{1}](1\bar{1}2)$ and $[\bar{1}\bar{1}1](2\bar{1}1)$.

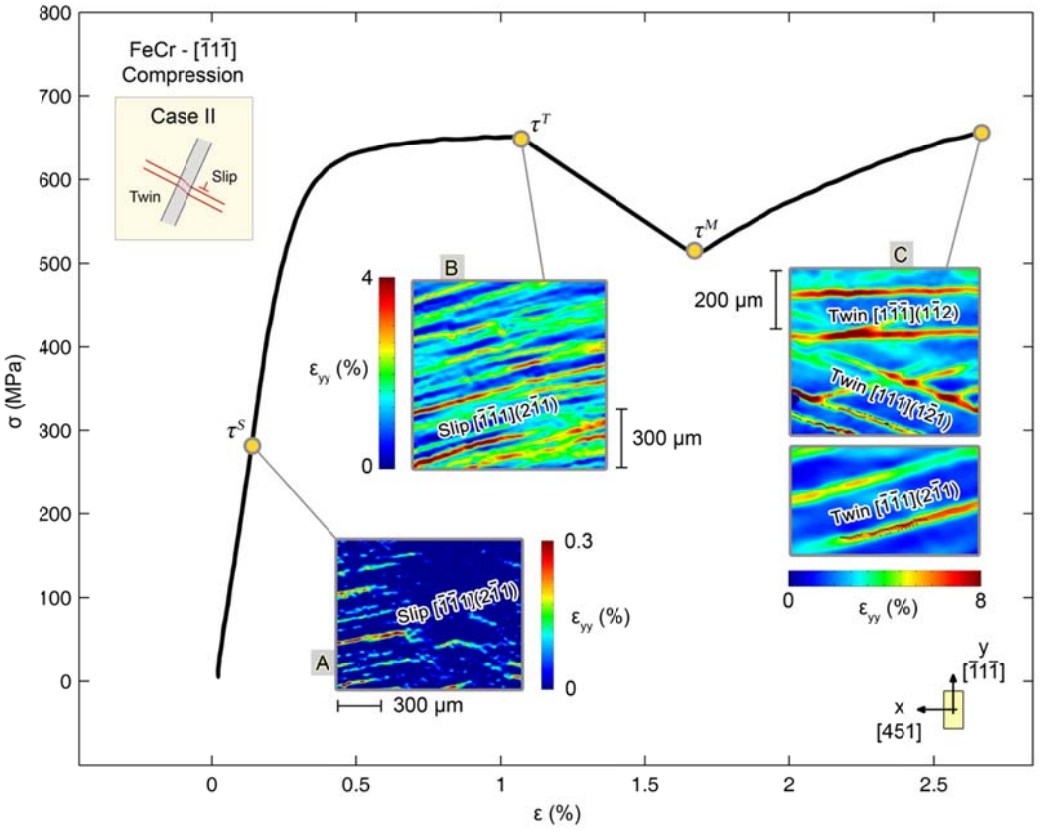

Figure 2.12. Stress-Strain curve and DIC strain field measurements for $[\bar{1}1\bar{1}]$ orientation in compression (*Case* II). Inset image marked A shows traces of localized slip on the $[\bar{1}\,1\bar{1}](2\,\bar{1}1)$ system. Slip develops on the same systems until the onset of twin nucleation (inset image marked B). The inset image marked C displays the strain localizations introduced by the nucleation of three twin systems from the <111>{112} family. All the strain plots are obtained using ex situ high resolution DIC.

In addition to DIC strain fields, TEM analyses for the $[\bar{1}1\,\bar{1}]$ orientation in compression are also provided. In Figure 2.13 are reported two TEM micrographs showing: (a) different dislocations gliding on various systems; and (b) an high resolution image displaying a twin.

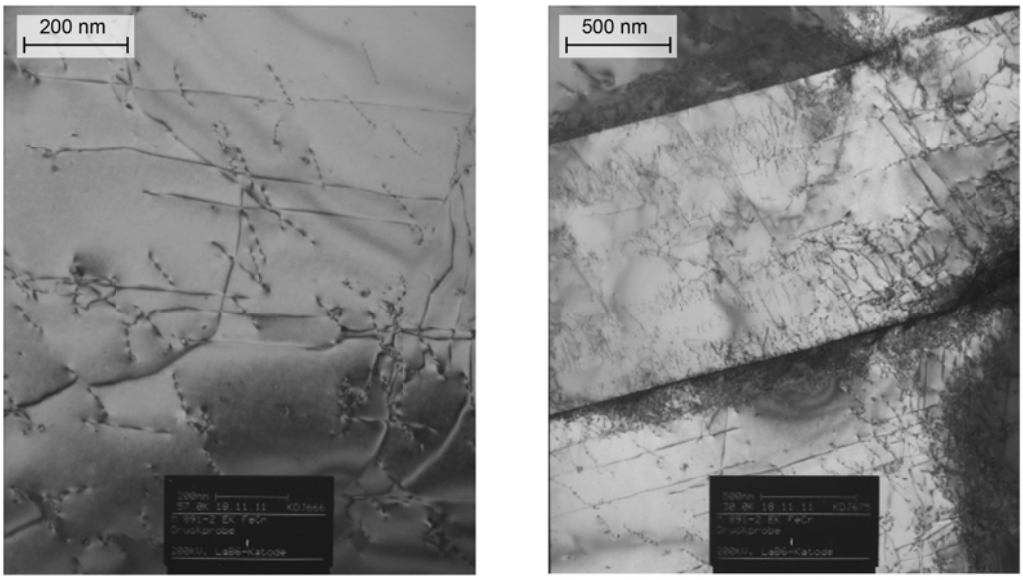

Figure 2.13. TEM images of a twin for the $[\bar{1}1\bar{1}]$ orientation in compression: a) dislocations from various systems; b) High resolution image displaying a twin.

2.6. Crystal orientation $[\bar{1}0\bar{1}]$

2.6.1. Tension experiments

Case III represents cases characterized by limited number of activated slip systems (Table 2.2). Figure 2.14 shows the stress-strain curve of a $[\bar{1}0\bar{1}]$ oriented sample in tension. For the inset marked A, the strains localize in bands with a slope that matches the trace of the $[111](1\bar{2}1)$ slip system ($m^s = 0.47$), leading to a CRSS of τ^S=87 MPa. By following the evolution of the axial strain fields through the in situ DIC measurements (inset images marked A, B, C and D) we observe higher strains developing still on bands corresponding to the $[111](1\bar{2}1)$ slip system. Traces of slip on the $[1\bar{1}1](121)$ system are also detected (inset images marked B, C and D).

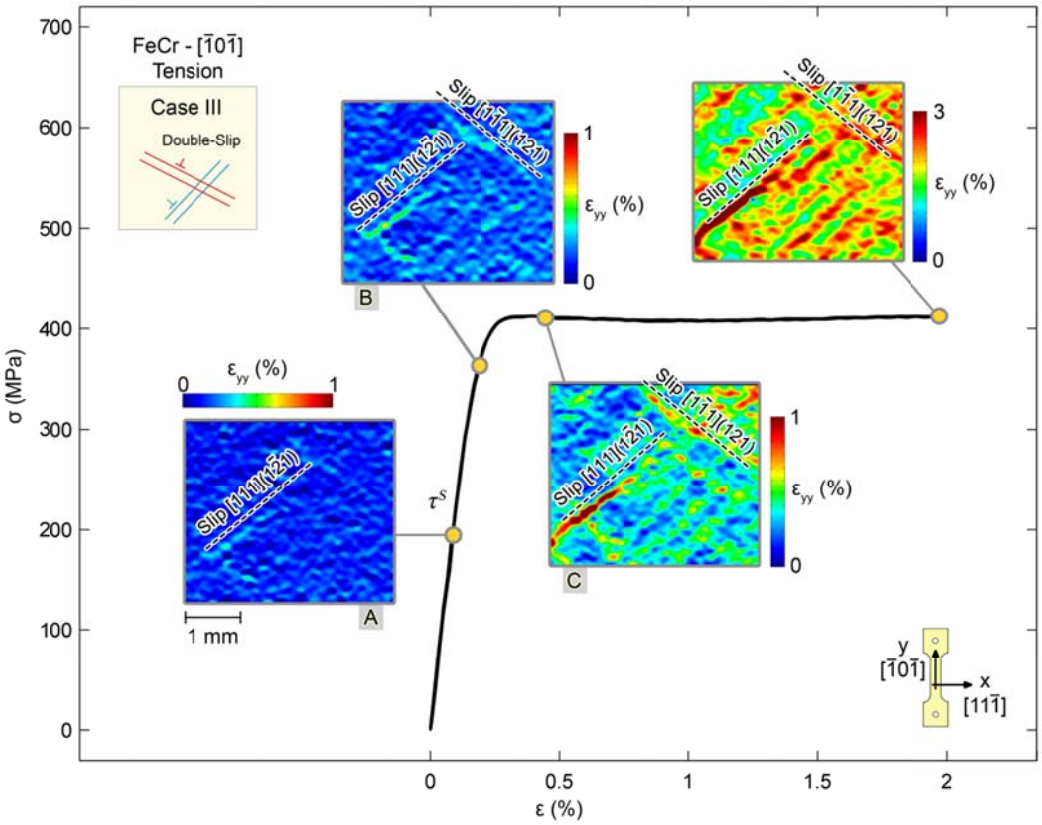

Figure 2.14. Stress-Strain curve and DIC strain field measurement for the $[\bar{1}0\bar{1}]$ orientation in tension (*Case* III). The inset image marked A shows onset of slip on the $[111](1\bar{2}1)$ system. Slip on the same system proceeds with loading as shown in the inset images marked B-C-D. From the latter strain plots traces of slip on $[1\bar{1}1](121)$ system are also detected.

The in situ DIC also shows that the activated slip systems accommodate deformation differently. To elucidate the difference, we utilize high resolution ex situ axial strain measurements. Figure 2.15 reveals again how the slip system $[111](1\bar{2}1)$ provides higher strains at this stage of the deformation (ε=1.8%). This can be clearly seen from the inset image marked A where localized strains along the bands corresponding to the $[111](1\bar{2}1)$ slip system display axial strains up to 3%. The specific case of crystal orientation $[\bar{1}0\bar{1}]$ in tension is an example of the double slip case (Table 2.2). We draw the conclusion that for relatively low applied strains (up to 3%) no hardening is observed since only one or two slip systems are active (*Case III*, double slip).

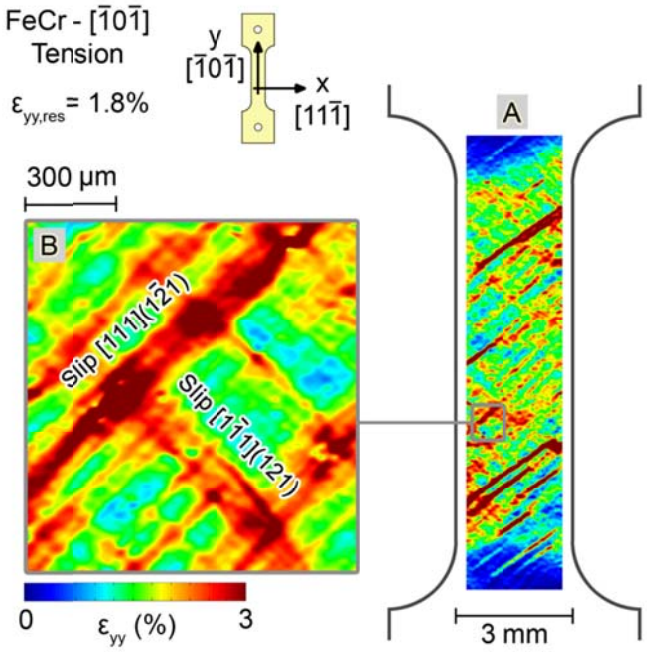

Figure 2.15. Local strain measurements using high-resolution DIC for the $[\bar{1}0\bar{1}]$ orientation in tension (*Case* III). The inset image marked A shows the residual strain field on the entire sample (low resolution DIC). The inset image marked B displays strain localizations along two traces corresponding to $[111](1\bar{2}1)$ and $[1\bar{1}1](121)$ slip systems (high resolution DIC).

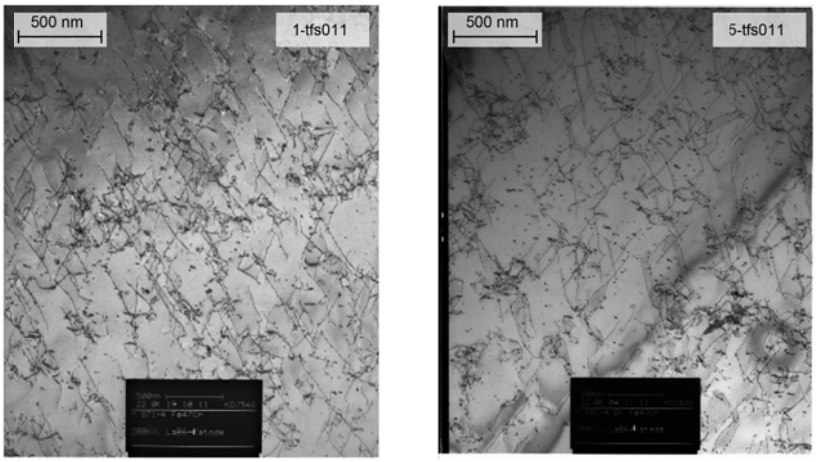

Figure 2.16. TEM image for the $[\bar{1}0\bar{1}]$ orientation in tension displaying dislocations from mostly two slip systems.

In Figure 2.16 TEM micrographs (obtained from two different samples) providing evidence of dislocations gliding on two slip systems confirming what observed on the macro-scale using DIC strain measurements (Figure 2.15).

2.6.2. Compression experiments

The results presented in Figure 2.12 for the $[\bar{1}1\bar{1}]$ orientation show evidence of high local strains for both twin and slip. It follows that accurate assessment of strain accumulation induced by twin migration for that sample is not possible. To address this issue, we analyze a similar case of crystal orientation leading to twin-slip interaction on a $[\bar{1}0\bar{1}]$ sample, having the same mechanical behavior as the $[\bar{1}1\bar{1}]$ orientation (both $[\bar{1}1\bar{1}]$ and $[\bar{1}0\bar{1}]$ orientations are classified as Case II). The stress-strain curve for the $[\bar{1}0\bar{1}]$ orientation is shown in Figure 2.17. Three critical *in situ* strain fields are analyzed. The inset image marked A indicates activation of the $[111](1\bar{2}1)$ slip system with $m^S=0.47$ occurring at $\sigma^S=185\ MPa$ leading to a CRRS of $\tau^S=87\ MPa$.

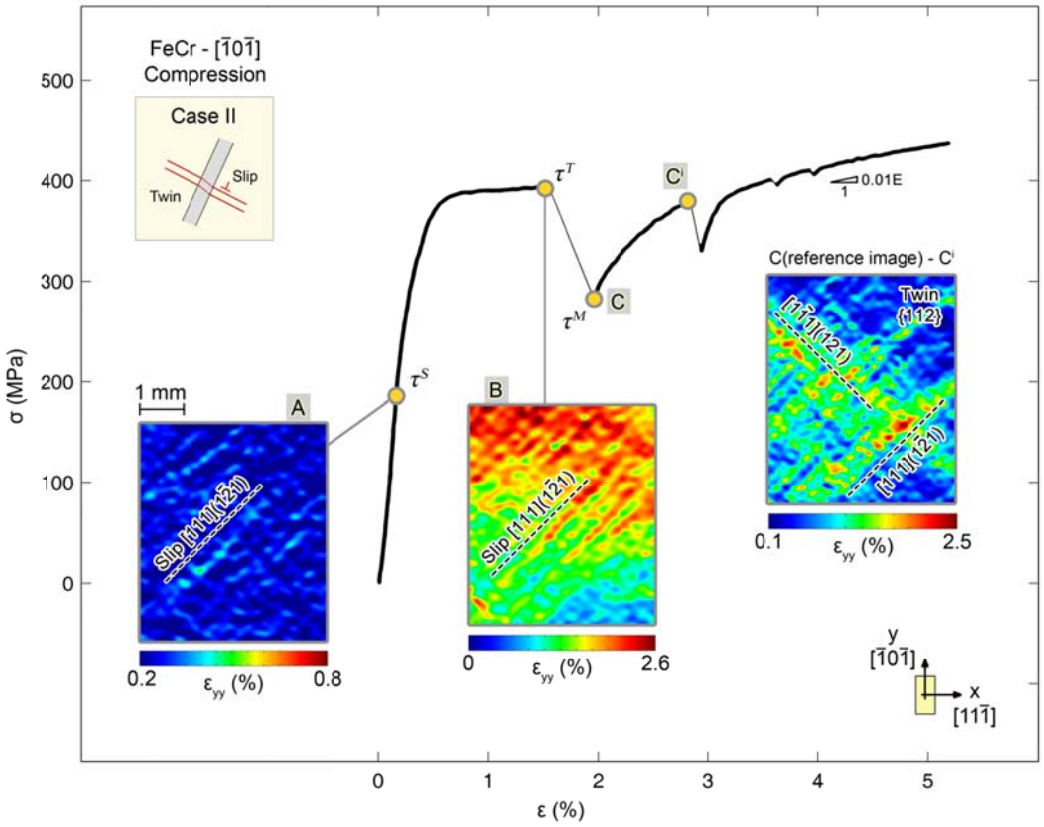

Figure 2.17. Stress-Strain curve and DIC strain field measurements for $[\bar{1}0\bar{1}]$ orientation in compression (*Case* II). The inset image marked A shows the onset of localized slip on the $[111](1\bar{2}1)$ system. Slip on the same system proceeds until twin nucleation (inset image marked B). Incremental DIC is used to illustrate twin migration in the inset image marked C-C^i (see text for details).

Proceeding along the stress-strain curve, at point B ($\sigma^T=413\ MPa$) the occurrence of the load drop indicates twin nucleation. Trace analysis indicates twin nucleation on $[1\bar{1}1](121)$ and $[111](1\bar{2}1)$ systems ($\tau^T=194\ MPa$). Incremental DIC is used to analyze the evolution of the axial strain field

between point C (following twin nucleation) and C^i, the correlation is implemented using the image at point C as the reference. The strains displayed in the inset image marked C-C^i represent strain accumulation between C and C' only. Referring to this inset image two observations are provided. (i) Twins nucleated in a region different from the preceding region displaying slip (inset image marked B). (ii) The strain accumulation between point C and C^i takes place in the same regions (bands) that were linked to twin nucleation. These observations indicate that the plastic response may be dominated by twin migration. The stress level at which plastic strains start to accumulate in the same bands that formed following twin nucleation marks the onset of twin migration $\tau^M = 149\ MPa$. Beyond point C^i, another load drop is observed, this indicates the nucleation of additional twins.

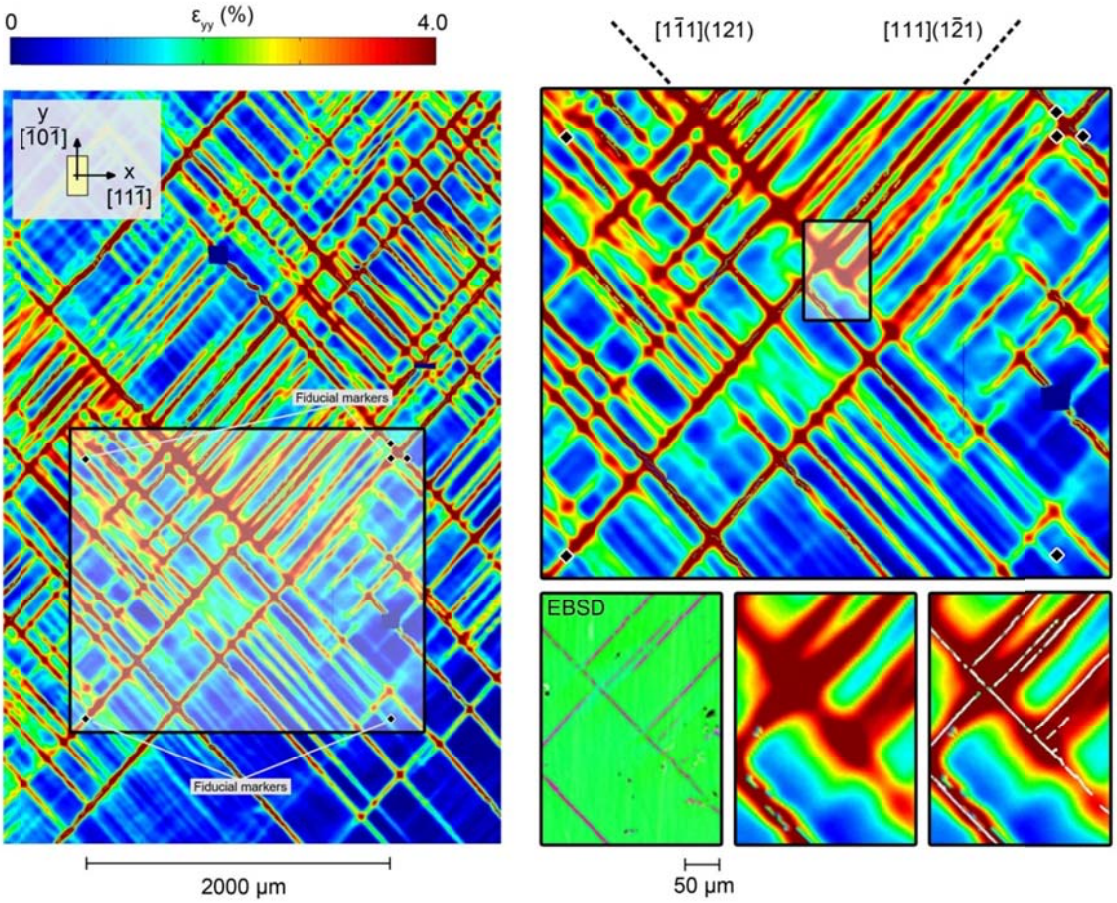

Figure 2.18. Case of local strain fields in case of Twin-Twin interactions for $[\bar{1}0\bar{1}]$ orientation in compression.

Ex-situ high resolution DIC was also used for analyzing $[\bar{1}0\bar{1}]$ orientation. Figure 2.18 shows the residual strain fields associated with large twinned regions. The markers introduced on the sample surface enable to locate a region contained in the DIC region, and overlap it with the EBSD data obtained for a small sample area. In the EBSD map reported in the bottom-right of Figure 2.18 are visualized the incoming twins which are stopped in front of an obstacle twin. In this cases, the

resolved strain measured along the incoming twin is high on the side of the obstacle twin where the incoming twin reaches the obstacle twin interface. It is easily observed that when different twinned regions are stopped in front of an obstacle twin (Figure 2.18 and successively in the strain field reported in Figure 2.19), the associated average strain field of the incoming twins is higher than the measured strain on the other side of the obstacle twin (strain plot on the right side of Figure 2.19).

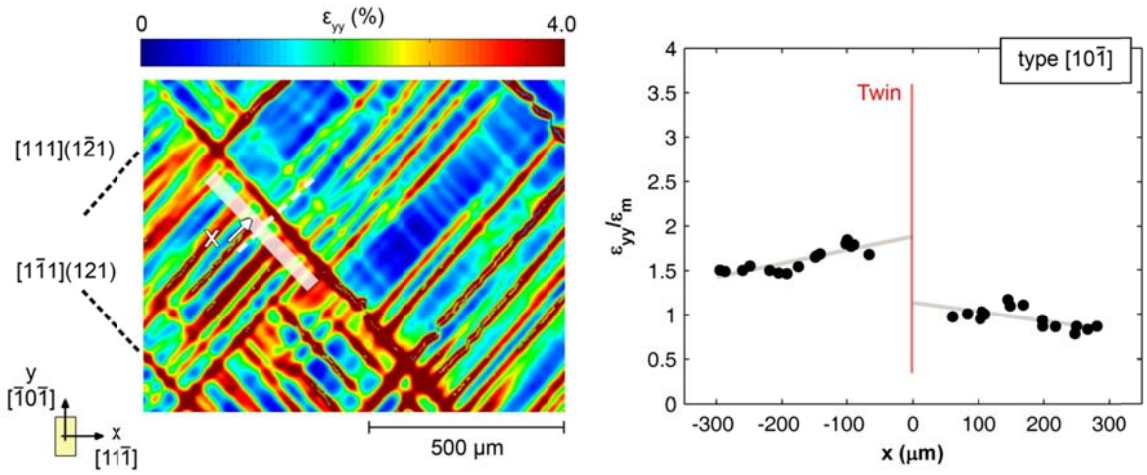

Figure 2.19. Strain measurements across the grain boundary of an obstacle twin.

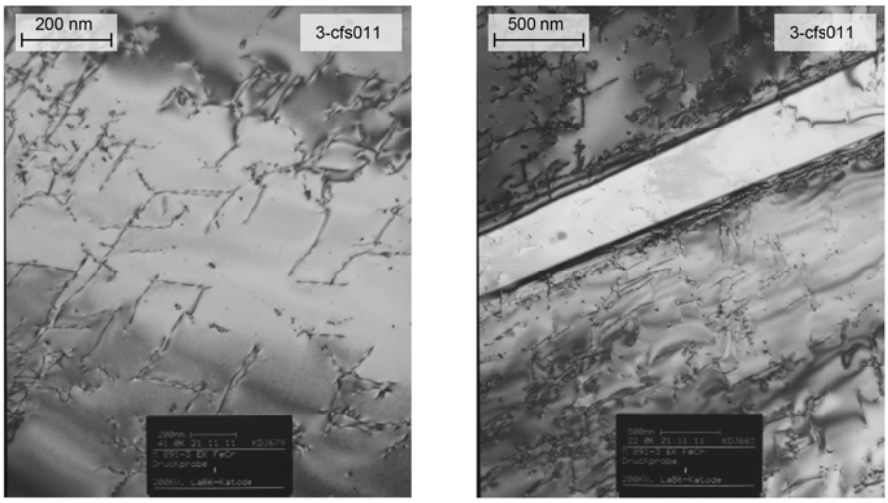

Figure 2.20. TEM image for $[\bar{1}0\,\bar{1}]$ orientation in compression: a) Planar dislocation on two systems; b) twin.

Further experiments using TEM confirm the presence of two slip systems (Figure 2.20a) and a case of twin-slip interaction (Figure 2.20b) which shows a case of slip blockage (incoming slip dislocations are blocked on the twin boundary).

2.7. Crystal orientation [314]

Crystal orientation [314] belongs to *Case III*. For this crystal orientation only one main slip system is observed in the first part of the stress-strain curve, and at microscopically level no crystal hardening is measured (Figure 2.21).

2.7.1. Compression experiments

The stress-strain curve for the [314] orientation is reported in Figure 2.19. Slip onset is measured at a resolved shear stress of $\tau^S = 91\ MPa$ (inset marked A in Figure 2.21).

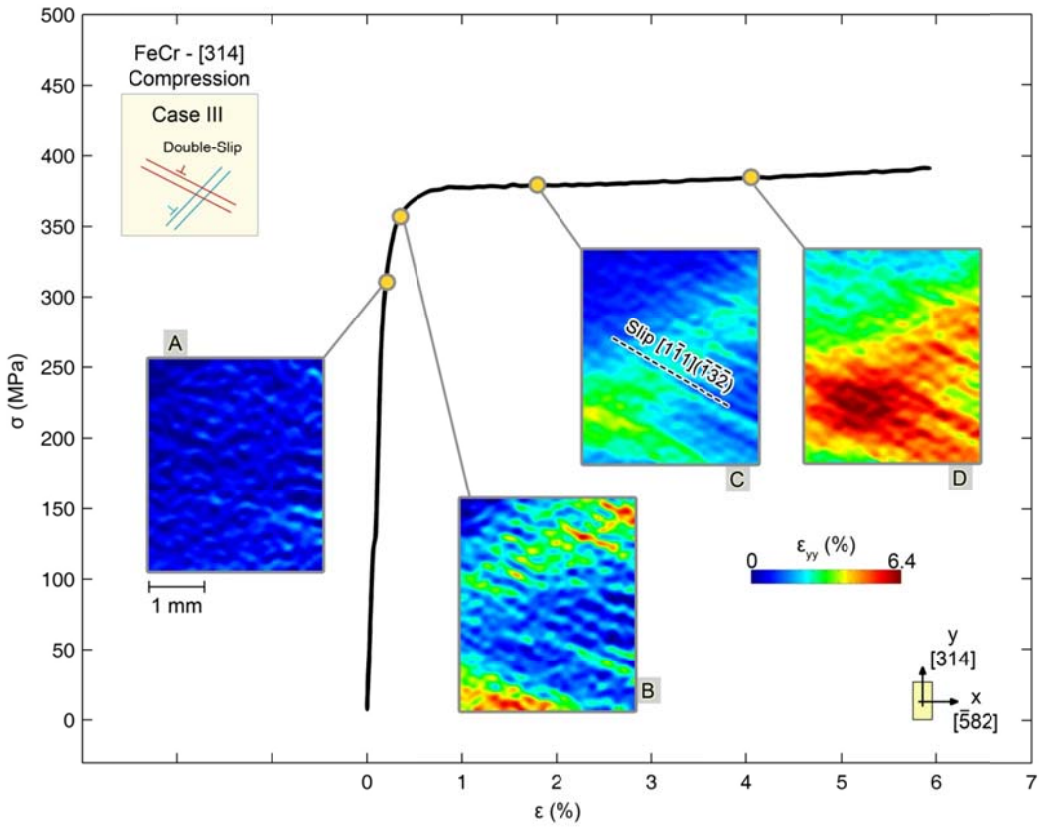

Figure 2.21. Stress-Strain curve and DIC strain field measurements for [314] orientation in compression (*Case* III). The $[1\bar{1}1](\bar{1}32)$ slip system is observed.

Proceeding along the stress-strain curve, only the $[1\bar{1}1](\bar{1}32)$ slip systems is active. For this crystal orientation, as for the $[\bar{1}0\bar{1}]$ orientation tension (section 2.6.1), no crystal hardening was observed since the presence of only one main slip system. The local strain magnitudes for this cases are lower than the strain values measured for the crystal orientations which display twin-twin and twin-slip mechanisms. In fact, as shown in the strain field reported in the inset marked D, the maximum strain measured is around 6.4%, while the average strain on the sample surface is about 4.15%. For the

twin-twin and twin-slip cases presented before much higher differences between local strains and average strains were measured.

2.8. Further analysis of the results

The usage of local deformation measurements from DIC allow for the precise determination of the critical stresses associated with the activation of slip τ^S, twin τ^T, and twin migration τ^M which are otherwise not accessible utilizing nominal sample response measurements. For example, slip can occur locally despite the overall elastic response in a number of cases. Twin nucleation is associated with a sudden load drop and can be measured by various experimental techniques, but the subsequent migration can occur immediately after the load drop or after further deformation. In situ local strain measurements via DIC permitted measurement of corresponding stress level at which twin migration initiates. The results from all the crystal orientations tested are summarized in Table 2.3.

The crystal orientations analyzed are classified in four different cases (see schematic in Figure 2.5). These four cases represent the possible crystal deformation behaviors based on the type of deformation mechanism involved (slip/twin). Each case displays a crystal hardening that is function of the main mechanism involved (twin-twin, twin/slip or slip/slip interactions). The real-time acquisition of the strain fields using DIC in conjunction with crystal orientations from EBSD determined the systems (planes and directions) and the CRSSs for slip onset τ^S, twin nucleation τ^T and migration τ^M for each crystal orientation analyzed (Table 2.3). While for slip and twin nucleation the CRSSs are constant, the twin migration stresses display deviations which are discussed in the following section.

Table 2.3. CRRSs for onset of slip τ^S, twin nucleation τ^T, twin migration τ^M as a function of the crystal orientation and load direction. The sequences S-T, S-S refer to slip-twin and slip-slip cases.

Mechanism				**Twinning (T)**		**Slip (S)**
	Axis	**Case**	**Sequence**	τ^T **(MPa)**	τ^M **(MPa)**	τ^S **(MPa)**
Compressive	$[\bar{1}0\bar{1}]$	II	S-T	194±8	149±19	87±16
	$[0\,\bar{1}0]$	IV	S-S	Not observed		85
	$[\bar{1}1\bar{1}]$	II	S-T	203±3	157±3	88
	[314]	III	S-S	Not observed		91
Tensile	$[\bar{1}0\bar{1}]$	III	S-S	Not observed		93±1
	$[0\,\bar{1}0]$	I	S-T	173±13	114±3	85

2.8.1. Twin Migration Stress

In the experimental results reported in this chapter, the twin migration stress σ^M (τ^M) represents the point of macroscopic yielding on the stress-strain curves subsequent to twin nucleation. In fact, as evident from DIC strain measurements (Figure 2.7, 2.8 and 2.17), strains localize starting from τ^M in the same region formed after the load drop. In Table 2.3, the reported values for the CRSS for twin migration show variation depending on crystal orientation. The CRSS magnitudes for the $[0\,\bar{1}\,0]$ orientation in tension was 114 MPa while for $[\bar{1}1\,\bar{1}]$ and $[\bar{1}0\,\bar{1}]$ orientations in compression 153 MPa was measured. The first case is classified as Case I, and the second one as Case II. Two possible explanations are introduced to explain the difference in the CRSS values for twin migration for Case I and Case II. First of all, for the $[\bar{1}1\,\bar{1}]$ and $[\bar{1}0\,\bar{1}]$ crystal orientations in compression (Case II) twin nucleation is preceded by appreciable deformation (1.5% slip strain) developing in one primary slip system (Figure 2.12 and 2.17). It is conceivable to argue that this large slip activity preceding twin nucleation influences the subsequent twin growth process. A growing twin can encounter slip bands [23] thus having difficulties in penetrating them. Secondly, twin growth is influenced by the dominant intersection mechanism involved, i. e. twin-twin (*Case I*) or twin-slip (*Case II*), hence the product of the dislocation reactions occurring in the intersection region. The high stresses in the intersecting regions can promote the dislocation reactions that facilitate twin growth. Therefore for Case I, where twin activity is not preceded by prior large slip activity, and twin-twin interaction (high local stress) is the primary intersection mechanism, we measured lower τ^M.

2.8.2. Strain Hardening

It is also well-known that twin-twin, twin-slip and slip-slip intersections have an important effect on the crystal hardening. As shown in an analogous work on fcc steel by Efstathiou at al. [81], the visualized accumulation of plastic deformation in the twin-twin and twin-slip intersection regions can be correlated with the observed crystal hardening. In our experiments, at the point where twin migration is observed (at twin migration stress σ^M (τ^M)) on the stress-strain curves, all the crystal orientations displaying twinning (leading to twin-twin and twin-slip interactions) show high values of the hardening parameter $h=d\sigma/d\varepsilon_{pl}=0.2E$, and high localized strains (up to 10% for the $[0\,\bar{1}\,0]$ orientation in tension, and up to 8% for the $[\bar{1}1\,\bar{1}]$ orientation in compression). For the same level of deformation, the double-slip case doesn't show hardening ($[\bar{1}0\,\bar{1}]$ in tension, *Case III*, Figure 9), while the multi-slip case analyzed ($[0\,\bar{1}\,0]$ in compression, *Case IV*, Figure 11) displays a constant hardening parameter from the onset of macroscopic plasticity ($h=d\sigma/d\varepsilon_{pl}=0.01E$) that is lower compared to the twin-twin and twin-slip cases. For both the cases displaying slip, the localized strains (up to 3%) are much lower than the localized strains measured for *Case I* and *II* indicating that the level of strain

accumulation in the region of twin/twin, twin/slip and slip/slip intersection can be correlated with the observed level of hardening.

2.8.3. Twin Nucleation Stress

For each of the crystal orientations displaying twinning ($[0\,\bar{1}\,0]$ in tension, $[\bar{1}1\,\bar{1}]$ and $[\bar{1}0\,\bar{1}]$ in compression, Table 2.2), a CRSS of 191 MPa was measured for twin nucleation (see Table 2.3). Moreover, all the twin systems having the highest magnitudes of the Schmid factors m^T activate simultaneously. These observations support the prediction of the activated twin systems using Schmid factor analysis along with the knowledge of the twinning direction for each crystal orientation and load direction (see Section 3). The existence of a constant CRSS is noteworthy because if the measurement techniques is not precise, it is possible to report a deviation contrary to the current findings. For the crystal orientations $[0\,\bar{1}\,0]$ and $[314]$ in compression, and $[\bar{1}0\,\bar{1}]$ in tension only slip is observed since the resolved shear stress for twinning is rather low $m^T=0.24$ (Table 2.2). The choice of single crystals in this study is rather unique to isolate specific mechanisms.

2.8.4. Slip Nucleation Stress

For all the crystal orientations tested in our study (Table 2.2), slip develops on planes and directions having the highest SFs, <111>{112} in most cases and <111>{123} in others. Using high resolution images (3.0 - 0.44 μm/pixel) we pinpoint strain localization due to the slip onset appearing for each crystal orientation and load direction at a constant CRSS of 88 MPa. This type of resolution during deformation is rather unique. The results conform to the Schmid law for slip (Table 2.3) and slip precedes twin nucleation. Precise measurements are needed because slip nucleation in the elastic region of the stress-strain curve (see inset image marked A in Figure 2.7, image resolution used for DIC is 0.9 μm/pixel) was detected which cannot be gleaned clearly from macroscopic observations.

Overall, the experimental results point to the utility of DIC to analyze the response of metals undergoing complex slip-twin evolution. The progression of these mechanisms are not readily explainable by macroscopic stress-strain measurements alone, and localized strain measurements shed light to the activation of slip and twinning during deformation and their interactions. Hence, the present approach provides insight for bridging the scales ranging from macroscopic response to localized behavior at micro-scales.

Chapter 3

Slip Transmission through Grain Boundaries in FeCr polycrystal

Understanding the interaction between slip dislocations and grain boundaries (GBs) has a paramount importance on the mechanical response of metals [82, 83]. In fact, extensive research has been reported during the last decades on the strengthening effect introduced by partial or full blockage of slip dislocations at GBs. In particular, much interest has been devoted on the results of the slip dislocation-GB reactions which provide deep insight into the slip transmission process across the GB. In this regard, early research focused on the details of these reactions at GBs utilized transmission electron microscopy (TEM) [48, 56]. Several insights into the transmission of the incoming dislocation, and incorporation into the GB with extrinsic (residual) dislocations have been gained as a result of these studies. Further experimental efforts are required to overcome the difficulties in correlating the results of these dislocation reactions with the associated strain fields across the GBs (on the meso-scale). A measure of the strengthening associated with a GB is decided based on whether dislocation strain fields undergo a continuous variation (full dislocation transmission), or whether large strains accumulate on one side of the GB (dislocation blockage). Therefore, a focused study on the experimental determination of the localized strains across GBs is important and will provide considerable insight into dislocation transmission and GB contribution to hardening. In this chapter are studied local strain fields at the meso-length scales covering multiple grains in Fe-Cr alloy. The strain measurements are used to establish the possible outcome of slip-GB interaction and provide further insight into the importance of the residual dislocation due to slip transmission.

3.1. Schematic of Slip Dislocation–Grain Boundary interaction

A schematic of a GB is shown in Figure 3.1. Grain 1 contains the incoming slip system, while Grain 2 contains the outgoing slip system. In this schematic, the dislocations leave the GB in the second crystal (outgoing slip plane) as a result of the dislocation-GB interaction. Of particular importance is the residual Burgers vector of the dislocation left at the GB [84-86].

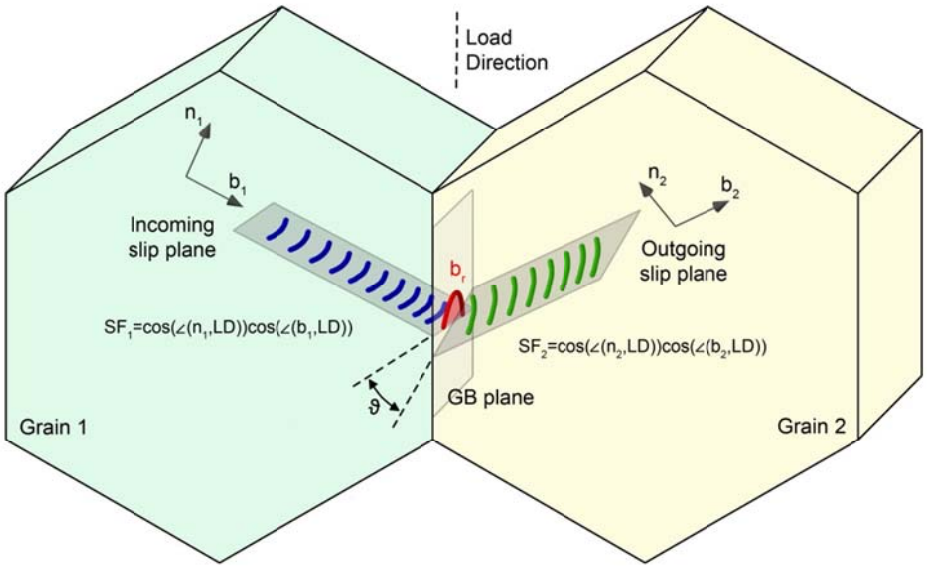

Figure 3.1. Schematic of the dislocation-grain boundary interaction geometry. For both the incoming and outgoing slip planes are indicated the normal to the slip planes (n_1 and n_2) and the Burgers vectors of the dislocations (b_1 and b_2). ϑ indicates the angle between the lines of intersection between the two slip planes and the GB plane. The Burgers vector of the residual dislocation left at the GB is determined from the equation $\vec{b}_1 = \vec{b}_2 + \vec{b}_r$.

Based on the geometry of the incoming and outgoing slip systems, different possible reactions can occur [83]: a) transmission by cross-slip: the slip planes intersect the GB plane on a common line ($\vartheta = 0$ where ϑ is the intersecting angle), $\vec{b}_1$ and $\vec{b}_2$ are parallel to the intersection line, no residual dislocation is left on the grain boundary; b) direct transmission: $\vartheta = 0$, in this case $\vec{b}_1$ and $\vec{b}_2$ are not parallel, a partial residual dislocation is left on the GB; c) indirect transmission: $\vartheta \neq 0$, $\vec{b}_1$ and $\vec{b}_2$ are not parallel, a partial residual dislocation is left on the GB; d) no transmission, the dislocations don't cross the GB and remain in the GB. For these cases the residual Burgers vector magnitude varies from zero for the case (a) to higher values in case (b) and (c) [48], and to a maximum for (d). The residual Burgers vector magnitude, $|\vec{b}_r|$, can be evaluated from

$$\vec{b}_1 = \vec{b}_2 + \vec{b}_r \Rightarrow |\vec{b}_r| = |\vec{b}_1 - \vec{b}_2| \tag{3.1}$$

where $\vec{b}_1$ (incoming) and $\vec{b}_2$ are determined on the same coordinate basis. $|\vec{b}_r|$ is used to quantify the GB resistance to slip transmission, with the aim to link the reaction occurring at the atomic scale with the strains induced by dislocation slip on the meso-scale. For the GBs analyzed is shown how, as a function of the residual Burgers vector magnitude, the strains are transmitted almost unaltered in case of low residual Burgers vector magnitudes, while they accumulate on one side of the

interface in the high residual Burgers vector magnitude cases. A clear characterization of the strain accumulation across GBs is achieved as a result of this experimental study. The experiment is confided to small deformations in compression with external strains less than 2%. The advantage of choosing the FeCr alloy is that we could observe predominantly one single slip system in the grains making the Burgers vector conservation analysis rather simple, and avoiding complex interactions associated with multiple slip systems. Successively, the analysis is focused on the strain gradients generated at the GBs. The correlation between the strain gradients across the GBs with the magnitude of the residual Burgers vector provides an excellent tool to quantify the capability of strain transmission at a GB.

3.2. Material and Methods

3.2.1. Microstructure characterization

A FeCr alloy with a composition of 47.8 at. pct. % Cr was sectioned into 4 mm x 4 mm x 10 mm compression sample by electro-discharged machining (EDM). The material was solution annealed at 900 ºC for 1 h followed by a water quench. For EBSD the surface was polished using SiC paper (from P800 up to P4000), and a final polishing suitable for EBSD data acquisition was obtained using a vibro-polishing with colloidal silica (0.05 μm).

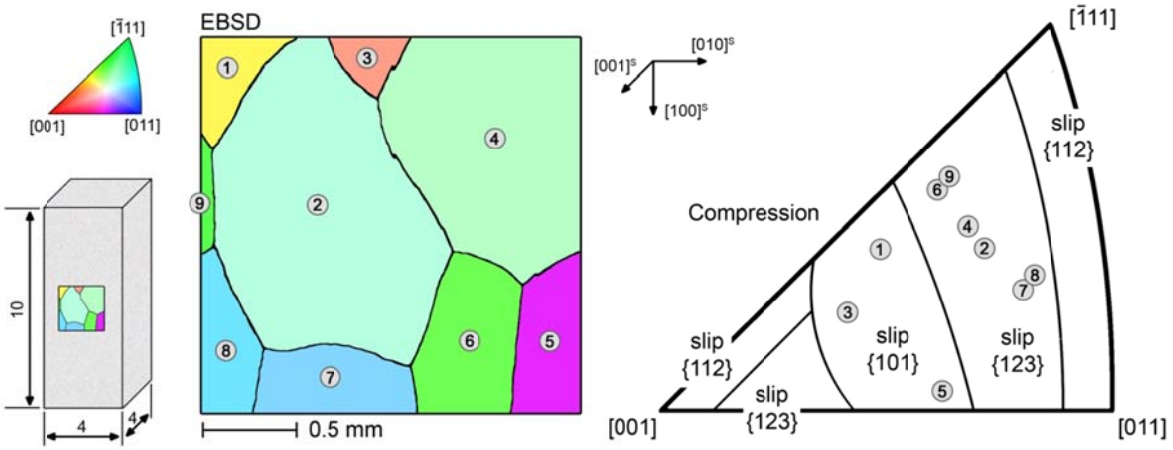

Figure 3.2. Grain orientations in the load direction obtained via EBSD for a 2 mm x 2 mm region on the sample surface. Grain orientations in the load direction are also shown in the stereographic triangle along with the slip systems for bcc materials displaying the largest SFs.

A selected 2 mm x 2 mm region of the sample surface was marked using Vickers indentation marks (the procedure is discussed in [66], also used in [43, 87]). The crystallographic grain orientations for the selected region of the specimen surface were obtained using EBSD. The grain orientation map of the area analyzed in the present paper is shown in Figure 3.2 and the corresponding Euler angles in Bunge convention (φ_1, Φ, φ_2) for each grain are reported in Table 3.1.

A total of nine grains are visualized in the selected area, with an approximately mean grain size of about 1 mm. In Figure 3.2, the stereographic triangle along with the crystal orientations of each grain in the load direction is also reported. The stereographic triangle is subdivided into five regions ([88]) that indicate the slip systems with the largest Schmidt Factors (SFs) for bcc materials. SF analysis was used in combination with slip trace analysis (from strain fields) for indexing the observed slip systems (see Section 1.5).

Table 3.1. Euler angles obtained from EBSD for each grain in the selected area of the sample surface.

Grain	1	2	3	4	5	6	7	8	9
φ_1 [°]	205.8	314.95	260.11	286.41	300.41	220.23	236.51	242.12	231.9
Φ [°]	41.56	49.86	19.92	32.46	34.42	46.03	45.97	43.49	37.21
φ_2 [°]	46.47	52.21	359.49	2.24	52.63	34.38	28.82	19.69	19.42

3.2.2. Experimental set-up and strain measurements

The experiments were conducted at room temperature using a servo hydraulic load frame. The sample was deformed in displacement control at a mean strain rate of $5x10^{-5}$ s^{-1}. In situ DIC [2, 11, 12, 89] was used for measuring the real-time evolution of the strain fields during loading (see also Chapter 1). The images were captured using an IMI model IMB-202 FT CCD camera (1600 x 1200 pixels) with a Navitar optical lens, providing for a resolution of 3.0 μm/pixel. The speckle pattern for DIC was obtained using black paint and an Iwata Micron B airbrush. A reference image of the sample surface was captured at zero load, and the deformed images of the same area every 2 seconds during the loading. The strain data obtained from in situ DIC were used to construct the stress-strain curve using the average axial strain for the selected in situ DIC region.

The main results were obtained using *ex situ* high resolution DIC. Adopting special fine speckles, the strain resolution obtained reveals the local strain intensities at grain level, in particular strain heterogeneities across grain boundaries were clearly established. As already explained in Chapter 1, the usage of ex situ DIC requires that the reference and deformed images are acquired out of the load frame using an optical microscope which enables capturing higher magnification images. The strain fields obtained refer to the un-loaded condition (residual strains). A speckle pattern suitable for high resolution DIC was applied on the surface sample after the initial EBSD scan (Figure 3.2). A set of 140 images covering the analyzed region was captured before the experiment (reference condition) and after loading the sample (deformed condition). The correlation was implemented for each pair of images (reference and deformed) and the results were successively stitched together. The grain map was overlaid with the strain fields using the Vickers indentation marks which are visible in the EBSD grain orientation map and the optical microscope images. The observed slip

systems were indexed using grain orientations from EBSD, and combining SF analysis with the slip traces on the strain fields obtained from high resolution DIC strain fields.

3.3. Results

In the following sections are reported the DIC strain measurements obtained from the compression experiments. All the strain fields report the axial strain ε_{yy} in the load direction. In section 3.3.1 the stress-strain curve along with two ex-situ DIC strain fields obtained after two successive load steps are analyzed. Higher ex-situ strain measurements are provided in Section 3.3.2 for the first load step which allow the slip systems indexing, and successively the evaluation of the dislocation reactions ($\vec{b}_r$) for each GB. In section 3.3.3 local strain measurements across GBs are used for calculating the strain changes in proximity of the GBs.

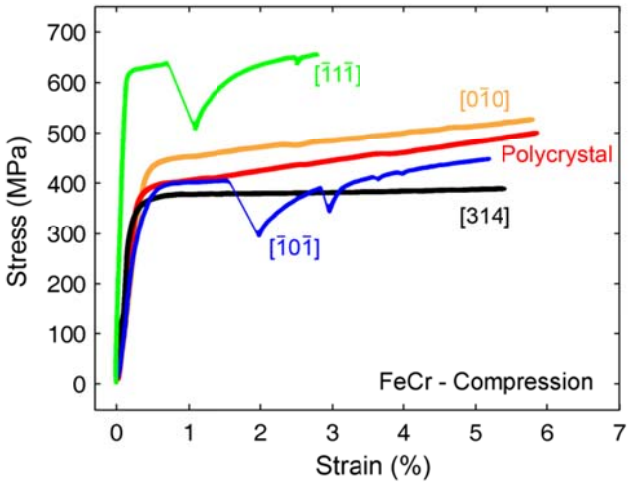

Figure 3.3. Comparison between single crystal experiments presented in Chapter 2 with the polycrystal case.

3.3.1. Stress-strain curve and DIC strain measurements

Figure 3.3 shows a comparison between the stress-strain curves obtained in compression for the polycrystal case and the single crystal samples analyzed in Chapter 2. The polycrystal case displays a mechanical behavior which is located between the single crystal stress-strain curves. In particular, the polycrystal case displays an hardening modulus which is comparable to the $[\bar{1}0\bar{1}]$ orientation (twin-slip case) and the $[0\bar{1}0]$ orientation (multi-slip case, see Chapter 2). Moreover, all the grains in the polycrystal sample analyzed displays one main slip system active. It follows that the hardening shown by the polycrystal case is induced by the presence of the grain boundaries. This represents an important aspect of the analysis presented in this chapter, since all the strain measurements obtained across the grain boundaries refer to local strain heterogeneities that follows to partial

transmission of slip dislocations and that induce hardening due to the presence of the grain boundaries.

In Figure 3.4a, the strain fields shown in the inset images marked A^i and B^i represent the residual axial strain fields for the 2 mm x 2 mm region obtained via ex-situ DIC. Each strain field is a composition of 9 images (resolution 0.87 μm/pixel) captured outside the load frame and after unloading from points A and B on the stress-strain curve. Strain heterogeneities develop as a consequence of the local material microstructure (see also the EBSD map in Figure 3.2).

Two regions are selected from the global strain fields: 1^A and 2^A after load step A^i, and 1^B and 2^B after load step B^i (Figure 3.4a). In Figure 3.4b the same regions are paired with the schematic of the slip plane geometries. The GB plane is drawn using the GB trace from the EBSD map assuming that the normal lies on the plane of the sample surface. For the region marked 1, the observed incoming slip system is $[11\bar{1}](\bar{2}31)$, while the outgoing slip system is $[\bar{1}1\bar{1}](\bar{3}\bar{2}1)$. In that case, the residual Burgers vector magnitude is low:

$$\frac{a}{2}[11\bar{1}]_{Grain2} \rightarrow \frac{a}{2}[\bar{1}1\bar{1}]_{Grain4} + \vec{b}_r \Rightarrow |\vec{b}_r| = 0.38a \tag{3.2}$$

The strain fields 1^A and 1^B clearly show an accumulation of strains for both sides of the GB. In particular, this condition of strain transmission is held for both the loading steps. For the second case shown, a GB for which the reaction occurring between the incoming and the outgoing slip systems leads to a high residual Burgers vector magnitude was selected:

$$\frac{a}{2}[11\bar{1}]_{Grain2} \rightarrow \frac{a}{2}[11\bar{1}]_{Grain7} + \vec{b}_r \Rightarrow |\vec{b}_r| = 1.28a \tag{3.3}$$

The incoming slip system is $[11\bar{1}](\bar{2}31)$, while the outgoing slip system is $[11\bar{1}](2\bar{1}1)$.

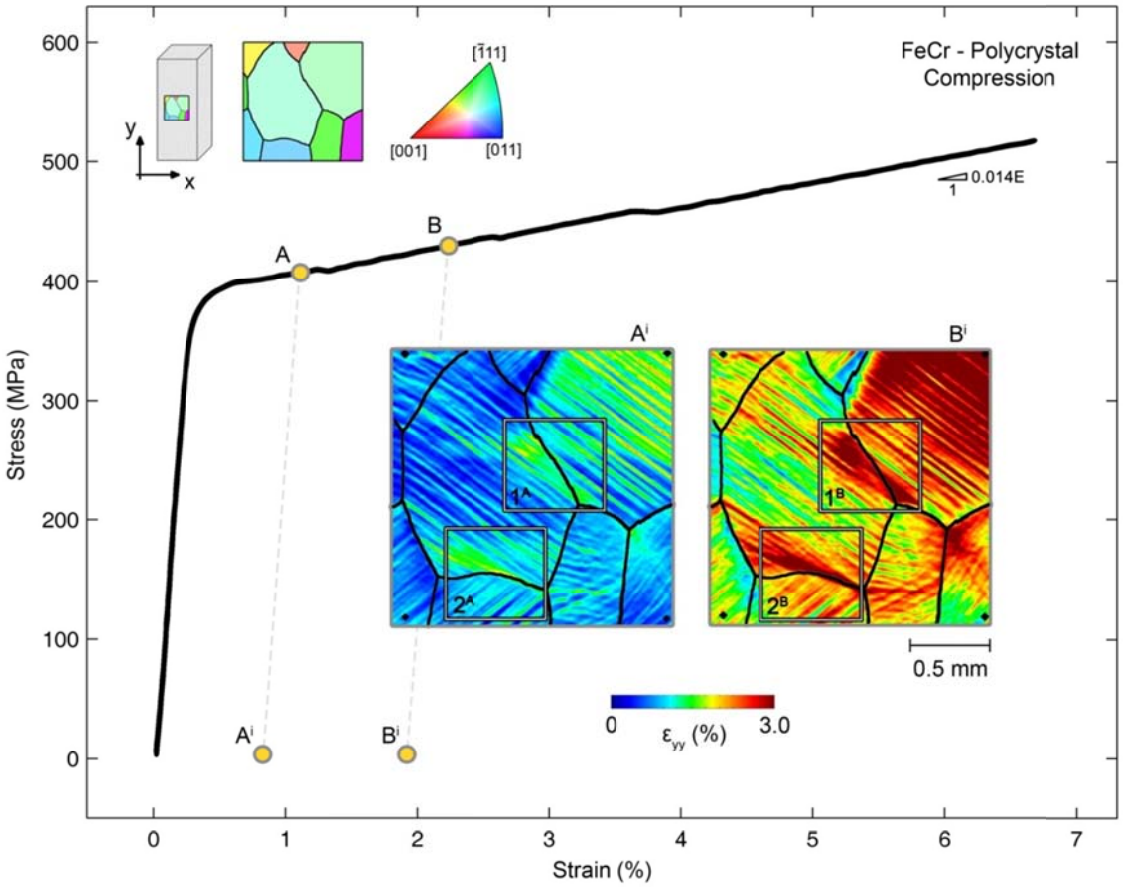

Figure 3.4a. Stress-strain curve and DIC strain measurements for the compression sample. The strain fields are obtained using ex-situ DIC measurements for two load steps, A^i and B^i. The two rectangles drawn in the inset images (A^i and B^i) mark regions $1^{A\text{-}B}$ and $2^{A\text{-}B}$ which show strain transmission through the GB and strain blockage on one side of the GB, respectively.

For the Grain 7 also the $[11\bar{1}](3\bar{2}1)$ slip system has high $SF = 0.49$, and the reaction leads to the same $|\vec{b}_r|$ value (the two alternative slip systems have the same Burgers vector). The $[11\bar{1}](2\bar{1}1)$ slip system was selected comparing the direction of the slip traces on the sample surface with the projection of the two slip planes. In this case the strains clearly accumulate on one side of the GB, indicating the difficulty for the incoming dislocations to be transmitted through the GB.

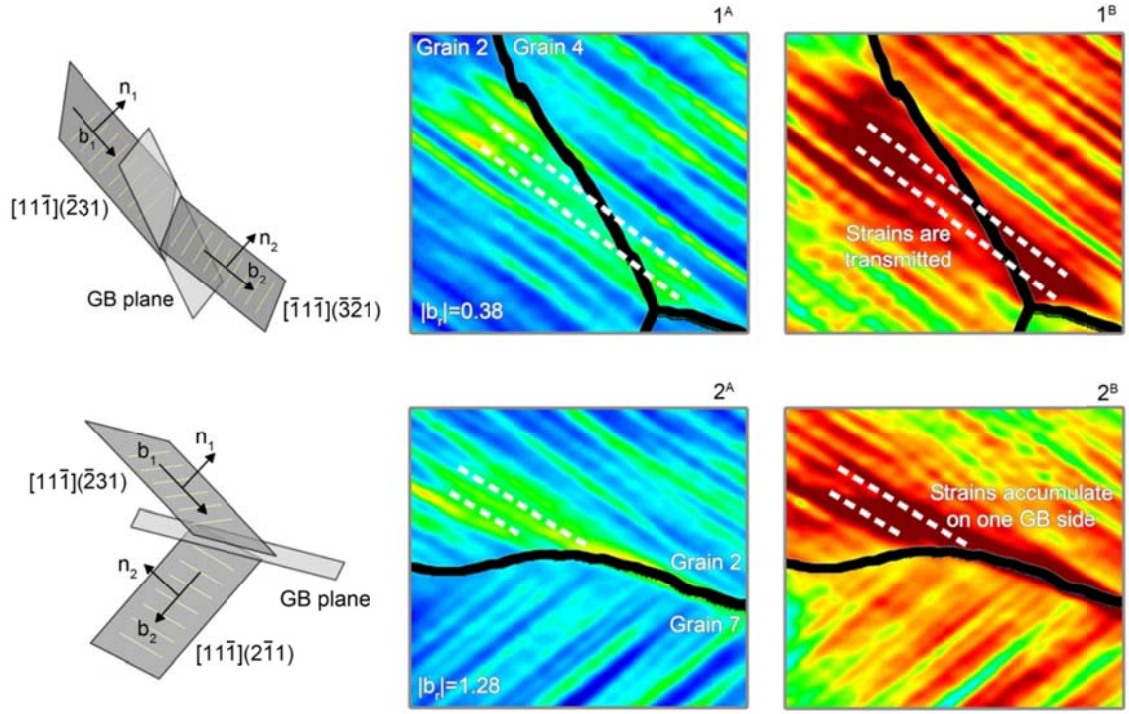

Figure 3.4b. Geometric analysis of the slip systems for the selected grain boundaries from Figure 3a. On the top a slip transmission case is described, the residual dislocation left at the GB has a low $|\vec{b}_r|$ and the strains are continuously transmitted across the GB. For the second case shown strains accumulate preferentially on one side of the GB and the associated $|\vec{b}_r|$ is high.

The accumulation of strains on the GB side of the incoming slip system is observed for both the loading steps. More details on the slip-GB interaction for the cases analyzed in equations 3.2 and 3.3 are given in Figure 3.4c. All the active slip systems have SF values close to the maximum resolved shear plane which has SF=0.5. The angle ϑ and the residual Burgers vector magnitude $|\vec{b}_r|$ are higher for the case of slip blockage ($|\vec{b}_r|=1.28$, $\vartheta=48.5°$) than for the slip transmission case ($\vartheta=17.6°$ and $|\vec{b}_r|=0.38$).

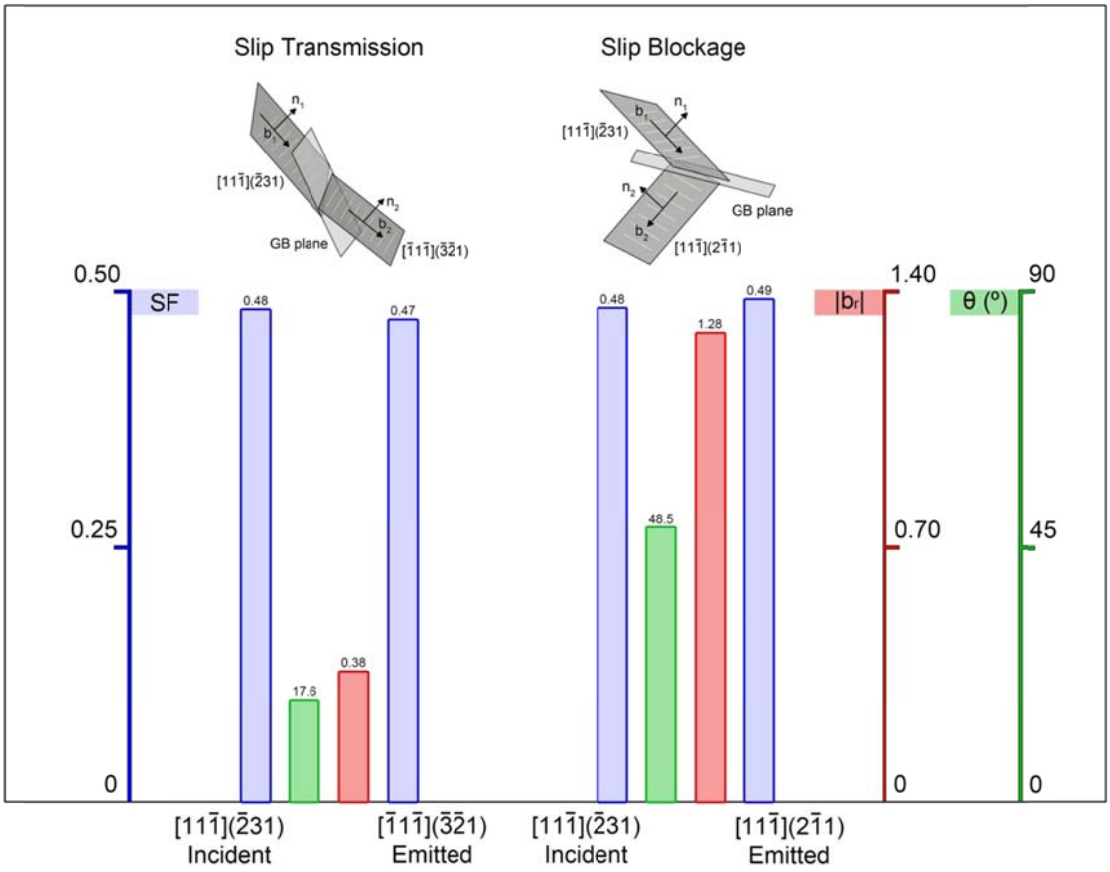

Figure 3.4c. SFs for the incoming and outgoing slip systems, $|\vec{b}_r|$ magnitudes and angle ϑ for the slip-GB interaction cases shown in Figure 3a. For both the analyzed cases the SF values of the activated slip planes are close to the maximum resolved shear stress plane ($SF = 0.5$). In case of slip transmission both the residual Burgers vector magnitude $|\vec{b}_r| = 0.38$ and the angle $\vartheta = 17.6°$ are low compared to the to the blockage case ($|\vec{b}_r| = 1.28$, $\vartheta = 48.5°$).

3.3.2. High resolution DIC strain measurements

Figure 3.5 displays the strain field obtained using images at higher resolution (0.18 μm/pixel). A total of 140 images were captured before the experiment and after loading the sample (point A^i in Figure 3.4a). Slip systems were indexed using grain orientations from EBSD. In particular, the possible slip planes for bcc materials on the well-known $<111>\{110\}$, $<111>\{112\}$, $<111>\{123\}$ slip system families were projected on the plane of the sample surface. The slip systems with largest Schmid Factors are successively selected comparing the projected lines with the slip traces on the sample surface.

In Table 3.2 the slip systems for each grain along with the SFs are reported. For grains 2, 3, 4, 5, 7 and 8 only one slip system is observed, while for grains 1 and 6 traces of a secondary slip systems

are visualized. In the schematic on the bottom of Figure 3.5 the $|\vec{b}_r|$ values for each GB are also reported. GBs on the DIC strain field with T indicate case of strain transmission visualized as a strain continuity along the slip traces, while B indicates the GBs for which no strain continuity is observed. For GBs 1-2, 2-4, 2-6, 7-8, 7-6 it is evident how the strains induced by slip continued almost unaltered through the interfaces, while for GBs 2-3, 3-4, 4-5, 5-6, 2-7, 2-8, 6-4 the strains accumulate on one side of the GB. Strain accumulation is particularly evident for GBs 4-5 and 2-7. Each GB can be also characterized by the estimation of the $|\vec{b}_r|$ magnitude (see schematic in Figure 3.5). In Table 3.3 a summary of the observed slip mechanism (T: slip transmission, B: slip blockage) and the correlation with the $|\vec{b}_r|$ magnitudes is given. It is clear that slip transmission corresponds to low $|\vec{b}_r|$, while for high $|\vec{b}_r|$ magnitudes the slip mechanism observed is blockage.

Table 3.2. Activated slip systems and SFs.

Grain	**1**	**2**	**3**	**4**	**5**	**6**	**7**	**8**
Slip System (SF)	$[\bar{1}11]$ $(0\bar{1}1)$					$[11\bar{1}]$ $(2\bar{1}1)$		
	0.46	$[11\bar{1}]$ $(\bar{2}31)$	$[11\bar{1}]$ $(1\bar{1}0)$	$[\bar{1}1\bar{1}]$ $(\bar{3}21)$	$[1\bar{1}\bar{1}]$ $(\bar{1}21)$	0.42	$[11\bar{1}]$ $(2\bar{1}1)$	$[11\bar{1}]$ $(2\bar{1}1)$
	$[\bar{1}11]$ $(1\bar{2}3)$	0.48	0.49	0.47	0.45	$[\bar{1}11]$ $(1\bar{2}3)$	0.49	0.49
	0.45					0.37		

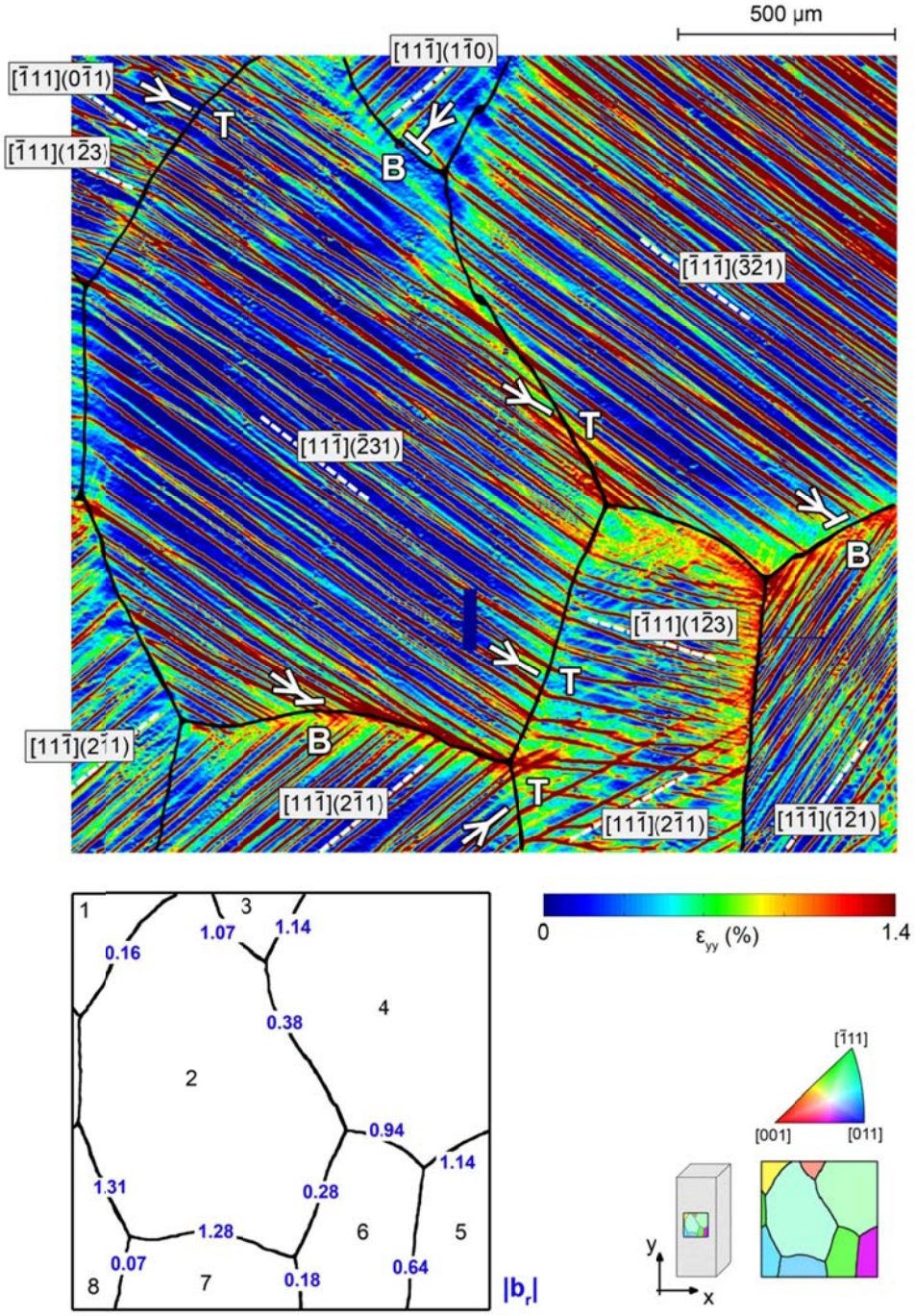

Figure 3.5. High resolution DIC strain field measurements (ε_{yy}). A total number of 140 reference images and 140 deformed images were captured outside the load frame (ex-situ), correlated and successively stitched. Slip systems were indexed using crystal orientations from EBSD selecting the systems with slip traces displaying the largest SFs. Depending on the magnitude of the residual Burgers vector, dislocations gliding on the active slip system in one grain can be transmitted through the GB or can be blocked at the GB. Different strain fields in the proximity of the GBs result from different dislocation-grain boundary interactions. Strains are transmitted in case of low $|\vec{b}_r|$, while they are blocked at the GB in case of high $|\vec{b}_r|$. In case of blockage, high local strains can be observed on one side of the GB (see for example GB 2-7).

3.3.3. Strain measurements across grain boundaries

In order to quantify the magnitude of the strain change across the GB sides, we provide two sets of strain measurements for low and high $|\vec{b}_r|$ magnitudes. The inset image marked A in Figure 3.6 shows the strain field across grains 1 and 2 (see also Figure 3.5). In this case a clear strain continuity associated with the incoming slip system $[\bar{1}11](1\bar{2}3)$ and outgoing slip system $[11\bar{1}](\bar{2}31)$ is observed through the GB, and the residual Burgers vector magnitude is low:

$$\frac{a}{2}[\bar{1}11]_{Grain1} \rightarrow \frac{a}{2}[11\bar{1}]_{Grain2} + \vec{b}_r \Rightarrow |\vec{b}_r| = 0.16a \tag{3.4}$$

Each point on the strain plots reported (Figures 3.6 and 3.7) refers to the average axial strain of a rectangular selection of strain values oriented along the GB side with an approximate size of 40 μm x 400 μm. For the case A (GB 1-2, Figure 3.6) the difference of the strain magnitudes approaching the GB is equal to $|\Delta\varepsilon_{GB1-2}| = 0.09\%$.

Table 3.3. Comparison between the observations on the DIC strain field on the slip mechanism (T: strain transmission, B: strain blockage) with the residual Burgers vector $|\vec{b}_r|$.

GB	**1-2**	**2-3**	**3-4**	**2-4**	**4-5**	**5-6**	**2-6**	**2-7**	**2-8**	**7-8**	**7-6**	**6-4**
Slip mechanism	T	B	B	T	B	B	T	B	B	T	T	B
$\|\vec{b}_r\|$	0.16	1.07	1.14	0.38	1.14	0.64	0.28	1.28	1.31	0.07	0.18	0.94

The second case (inset marked B, Figure 3.6) represents the strain measurements through grains 2 and 6 (see also Figure 3.5). Strain bands associated with the incoming slip system $[11\bar{1}](\bar{2}31)$ and the outgoing slip system $[\bar{1}11](1\bar{2}3)$ are still observed to propagate continuously across the GB. The DIC strain field displays also intermediate values of strain bands (green color) between the incoming slip bands on the left side of the GB. These additional strain bands developing in proximity of the GB can be associated with the partial dislocations left in the GB having a residual Burgers vector magnitude equal to:

$$\frac{a}{2}[11\bar{1}]_{Grain2} \rightarrow \frac{a}{2}[\bar{1}11]_{Grain6} + \vec{b}_r \Rightarrow |\vec{b}_r| = 0.28a \tag{3.5}$$

In the associated strain plot (inset marked B, Figure 3.6) the local strain measurements display a slightly increasing value approaching the left side of the GB. In this case the difference in the strain magnitudes approaching the GB is higher than the previous case and equal to $|\Delta\varepsilon_{GB2-6}| = 0.22\%$.

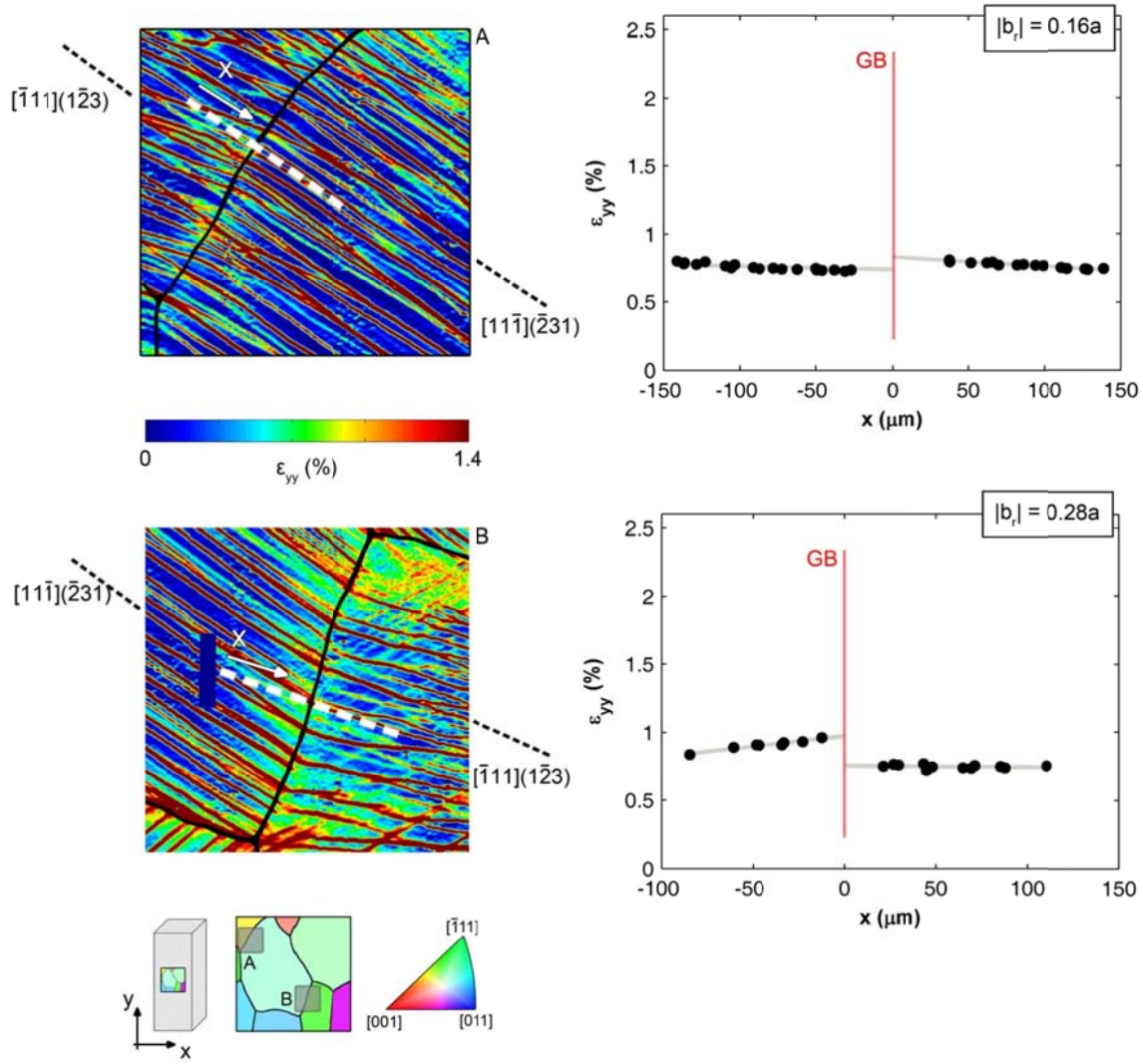

Figure 3.6. Strain measurements across a grain boundary in case of low $|\vec{b}_r|$. The inset marked A displays the lowest residual burgers vector magnitude calculated, $|\vec{b}_r| = 0.16a$. For this case strain transmit almost unaltered through the GB. For the inset marked B, a step on the strain field is observed which represents preferential strain accumulation on the left side of the GB, the residual burgers vector magnitude calculated is higher than in the previous case with $|\vec{b}_r| = 0.28a$.

In Figure 6 two cases of slip blockage corresponding to high $|\vec{b}_r|$ magnitudes are shown. The first case refers to the strain measurements across grains 4 and 5 (see also Figure 3.5). The incoming

dislocations glide on the $[1\bar{1}\bar{1}](\bar{1}2\bar{1})$ slip system, while the outgoing dislocations glide on the $[\bar{1}1\bar{1}](\bar{3}2\bar{1})$ slip system. The dislocation reaction on the interface results in a high residual Burgers vector magnitude equal to

$$\frac{a}{2}[1\bar{1}\bar{1}]_{Grain4} \rightarrow \frac{a}{2}[\bar{1}1\bar{1}]_{Grain5} + \vec{b}_r \Rightarrow |\vec{b}_r| = 1.14a \tag{3.6}$$

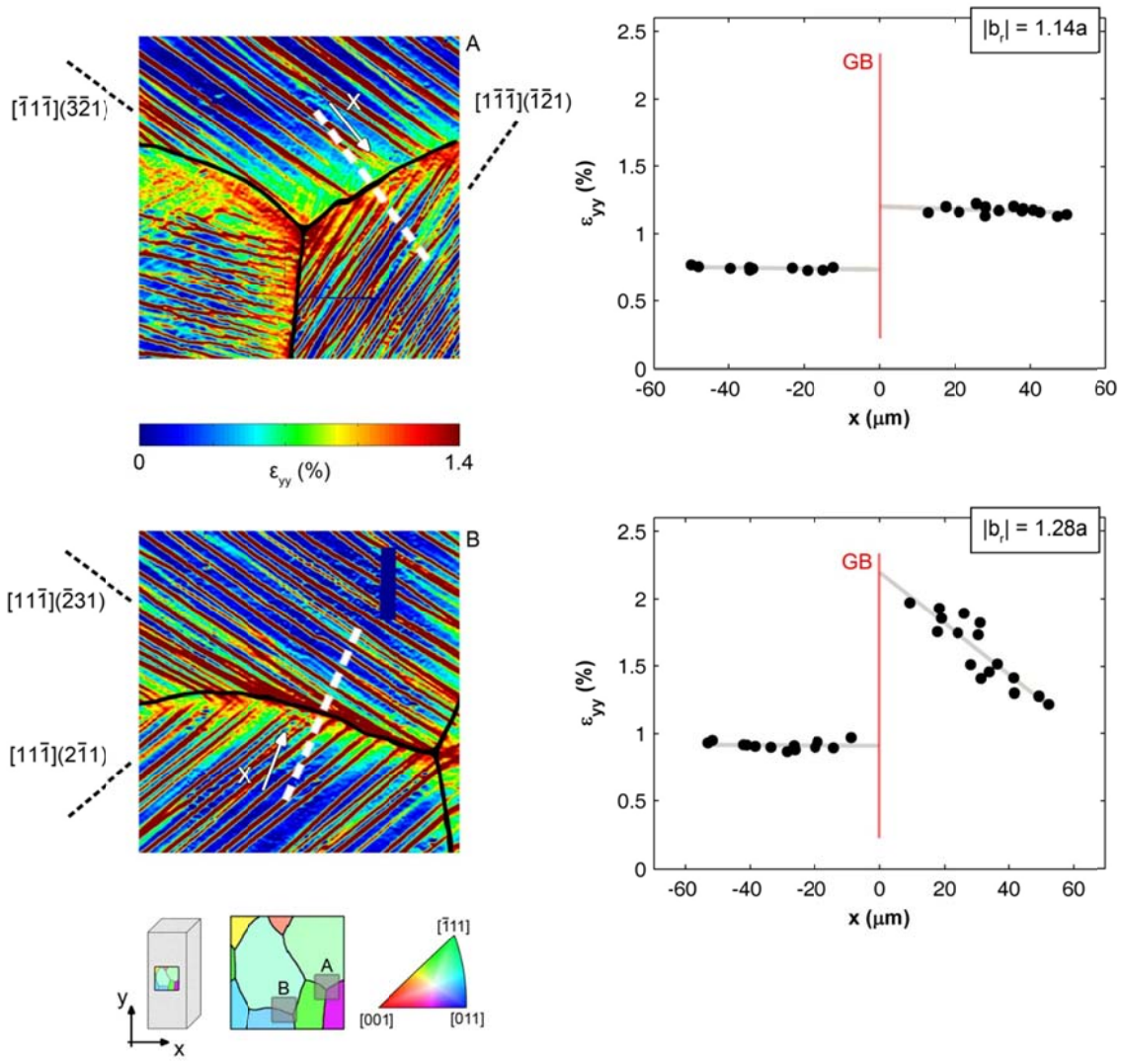

Figure 3.7. Strain measurements across a grain boundary in case of high $|\vec{b}_r|$. In both cases $|\vec{b}_r| > 1$ and the slip blockage on one side of the GB generates a high discontinuity on the strain field.

From the DIC strain plot (inset image marked A, Figure 3.7) it is clear that as a consequence of the high $|\vec{b}_r|$, strains are not transmitted and accumulate on the right side of the GB leading to an high

strain gradient equal to $|\Delta\varepsilon_{GB4-5}|=0.47\%$. The last case analyzed (inset image marked B, Figure 3.7) has been already introduced in Figure 3.4b (strain field 2^A) using lower image resolution (0.87 versus 0.18 μm/pixel). For the dislocation reaction between the incoming $[11\bar{1}](\bar{2}31)$ and the outgoing $[11\bar{1}](2\bar{1}1)$ slip systems see Eq. (3.2). From the strain measurements obtained, the strain change across the GB is particularly high $|\Delta\varepsilon_{GB2-7}|=1.29\%$.

3.4. Discussion

The concept of residual Burgers vector has been established in earlier works and its importance is well known in the materials science community [83, 90]. What has been lacking is a quantitative illustration of the link between the residual Burgers vector and the local strain fields. This became possible with the development of digital image correlation techniques, and special codes in this study, written for the purpose of analyzing the strains as the slip approaches the boundary, and emanates or gets blocked at the boundary. Using this methodology, in Section 3.3 are provided different types of strain fields across selected GBs which display different residual Burgers vector magnitudes. The strain fields are directly correlated with the mechanism of interaction:

- ✓ Low $|\vec{b}_r|\to 0$, the dislocations are transmitted through the grain boundary and the strains are continuous across the interface (Figure 5, inset marked A, $|\vec{b}_r|=0.16a$).
- ✓ Intermediate $|\vec{b}_r|=(0.2 \text{ to } 1)a$, a residual dislocation is left on the grain boundary, this represents the most common case, the strains accumulate on one side of the grain boundary depending on the $|\vec{b}_r|$ magnitude (Figure 5, inset marked B, $|\vec{b}_r|=0.28a$).
- ✓ High $|\vec{b}_r|>1$, dislocations are blocked at the grain boundary, high strain accumulation is measured on one side of the grain boundary (Figure 6, insets marked A and B, $|\vec{b}_r|=1.14a$ and $|\vec{b}_r|=1.28a$).

These results can be utilized to illustrate the significant role that grain boundaries play in the slip transfer process, in particular they can be useful in further modeling efforts, which include the strengthening associated with slip dislocation-GB interactions. The accumulation of residual dislocations at the grain boundary induces a strain discontinuity across the interface that is proportional to the $|\vec{b}_r|$ magnitude. It follows that $|\vec{b}_r|$ can be used as a parameter to quantify (i) the strain accumulation at the grain boundaries, and (ii) the strengthening effect due to the single grain boundary. We note the judicial choice of FeCr polycrystals with relatively large grain sizes, and most

importantly the activation of a single slip system in each grain. In the presence of two or more activated slip systems and also twinning, the interpretation of DIC strain fields become more complex and additional strengthening effects are introduced. Our experiments on single crystals of the same material and conditions (sample geometry, heat treatment and strain rate) indicate that no hardening is observed (for low deformations $\varepsilon < 3\%$) when only one or two slip systems are activated [91]. It follows that the contribution to the hardening observed in the present case ($h = 0.014E$) is provided by partial or full blockage of the dislocations at the grain boundaries. Therefore, the isolated single slip system results for the present polycrystal sample shed light into the mechanism very clearly, hence present unique findings in this work. In summary, in this chapter are illustrated the considerable promise of the digital image correlation method when utilized in conjunction with EBSD in gaining insight on the strain fields at the grain boundaries. Other techniques such as TEM can be used in conjunction with these results presented here as well. These results can be utilized to check the confidence of crystal plasticity calculations as well as the simulations conducted with molecular dynamics methods which provide a better description of grain boundaries.

Chapter 4

Damage accumulation on γ-TiAl

Part of this work is published in [91].

In this chapter are presented the results obtained from the fatigue experiments on the Ti-48Al-2Cr-2Nb alloy. Local strain measurements via high resolution digital image correlation enabled to further analyze the influence of the microstructure on the damage accumulation for this duplex γ-TiAl alloy. The analyzed Ti-48Al-2Cr-2Nb alloy was manufactured using Electron Beam Melting (EBM) technology. EMD allows to manufacture components without the typical defects derived from classical manufacturing processes. Such '*defect-free*' alloy enables to focus on the influence of the microstructure of γ-TiAl alloys in the damage accumulation process.

4.1 Manufacturing process

It is difficult to obtain a component produced with γ-TiAl intermetallics with exactly the composition and microstructure desired adopting the classical manufacturing processes. Using Electron Beam melting (EBM) technology (Figure 4.1), the process of material production operates under vacuum conditions, thereby reducing the risk of oxidation in the material of the final components.

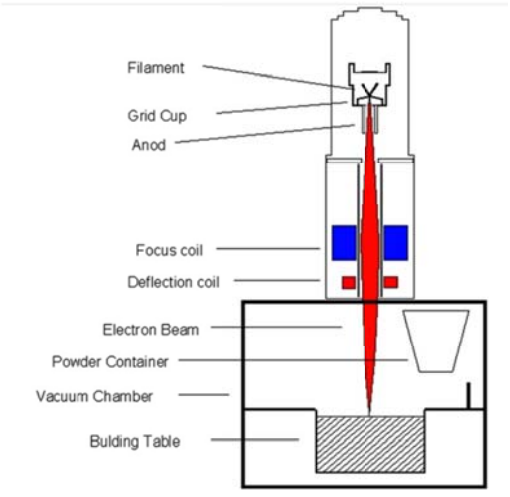

Figure 4.1. Schematic of the EBM machine (from [92]).

EBM technology for "layer by layer" productions offers several advantages with respect to other competing technologies and it is possible to operate at temperatures closer to the melting points of

the intermetallic alloys [93]. In the EBM process, components are produced without vaporization of the powders of the initial material and the powders are made of an intermetallic alloy based on titanium and aluminum with the same chemical composition as the final intermetallic with which the components are produced. The main advantage of the EBM process consists on the reduction of defects such as inclusions, pores etc. In this scenario more relevance on the material microstructure has to be accounted since the possible crack initiation sites can be found at general interfaces between equiaxed and lamellar grains. In this scenario the application of the defect tolerance design necessitates to focus on the effect of the material microstructure. An example which supports this concept is shown in Figure 4.2. The crack initiation site after a fatigue experiment was found in correspondence of a flat area resulted from the decohesion of a lamellar package. This example shows how the EBM process drastically reduces the presence of manufacturing defects, and crack initiation sites derive from the local microstructural features. It is so important to understand where strains localize before crack initiation occurs, and determine the critical conditions which lead to the formation of a crack.

In the following paragraphs the Ti-48Al-2Cr-2Nb alloy is characterized using the experimental approaches based on fatigue experiments. A series of experiments for the characterization of the material sensibility to defects in high cycle fatigue (HCF) regime using classical smooth samples and samples with an artificial defect are firstly presented. Further crack growth experiments by means of C(T) specimens allowed to analyze the crack growth for different crack lengths (short and long cracks).

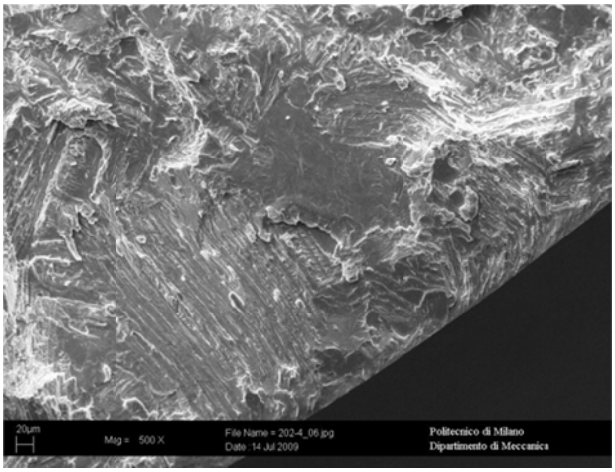

Figure 4.2. Typical failure initiation site found in fatigue tests. Specimen tested at room temperature failed after 3.2 10^6 cycles (R=0; σ_{max}=340 MPa), from [91].

The classical experimental methodologies allow to characterize the material on the meso-scale, thus neglecting all the effects correlated with the local material composition on the micro-scale lengths. In order to overcome the limitations of the classical experimental methodologies, we made a first attempt to rationalize the effect of the material microstructure using high resolution strain

measurements via digital image correlation (DIC) technique. The idea is to measure the localization of strains and correlate these localizations with the local microstructural features of the analyzed alloy (lamellar or equiaxed grains).

4.2 Material

The gamma titanium aluminide (γ-TiAl) Ti-48Al-2Cr-2Nb alloy studied in this work has been produced by means of the EBM A2 machine produced and distributed by Arcam AB (Sweden), according to a patented process [94] which allows focused electron beam melting to be performed in vacuum conditions (Figure 4.1). The EBM material was hot isostatically pressed (HIPed) at 1260 °C under a pressure of 1700 bar for 4 h. An heat treatment (TT), to be performed after HIP, was set up in order to obtain the duplex microstructure (2h at 1320 °C). As it may be observed in the micrograph of Figure 4.5, the duplex microstructure is composed of aggregates (or clusters) of equiaxed grains alternated with lamellar grains with randomly distributed orientations. From the observations made, no evidence of material defects like inclusions, pores or dendrites was found in the specimens. Material has been produced in the form of near-net-shape specimens and final the final sample geometry was manufactured by conventional machining with carefully selected cutting parameters for removing the machining allowance.

4.2.1 Microstructure

Intermetallics are defined as the *compounds of metals whose crystal structures are different from those of the constituent metals, and thus intermetallic phases and ordered alloys are included* [95].

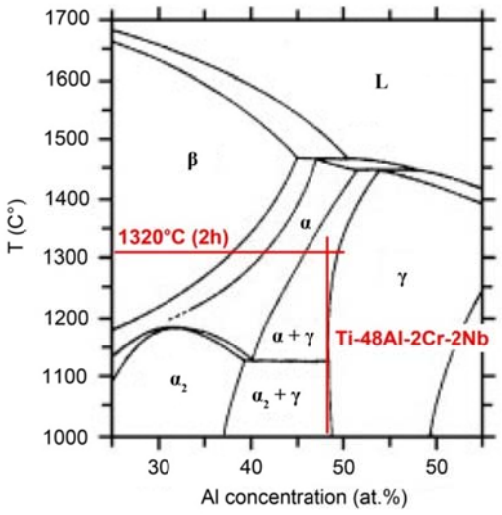

Figure 4.3. Binary Ti-Al phase diagram, [96].

The present alloy examined in this chapter, the gamma titanium aluminide (γ-TiAl) Ti-48Al-2Cr-2Nb, is mainly composed by the intermetallic phase γ-TiAl. From the phase diagram proposed by

McCullough, [96], following the heat treatment adopted (1320 °C for 2h) the main phase present is γ-TiAl. Since the heat treatment falls in the intermediate region between the γ-TiAl and (α_2-Ti_3Al + γ-TiAl), small fractions of the secondary α_2-Ti_3Al intermetallic phase can also be present along the γ-grain boundaries [97]. In general the deformation behavior of the alloy is determined by both the deformation behaviors of the present phases, γ-TiAl and α_2-Ti_3Al, which are characterized by two different crystal structures. The deformation is predominantly determined by the γ-TiAl phase which has a $L1_0$ crystal structure (Figure 4.4). For this structure, the main deformation mechanisms at room temperature are provided by ordinary dislocations and twinning on the planes and directions given in Figure 4.4 [63, 65]. The deformation provided by the secondary phase α_2-Ti_3Al is limited for the limited number of possible slip planes of the hcp crystal structure, and in the present case also for the small volume fraction.

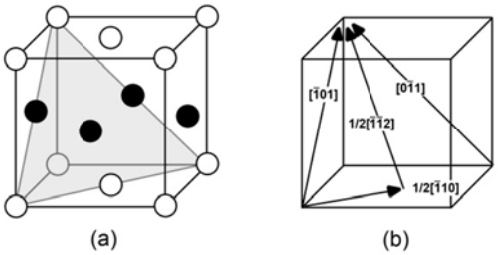

Figure 4.4. (a) $L1_0$ crystal structure for the main intermetallic phase γ-TiAl. In (b) the schematic indicates one of the $\{111\}_\gamma$ planes along with slip dislocation glides on the $\langle 110 \rangle$ direction and twinning develops along $1/6\langle 11\bar{2}]\{111\}_\gamma$.

The phases can solidify in two different microstructures: equiaxed and lamellar grains. Each microstructure has a different mechanical behavior, in particular for the fatigue properties of the alloy. For the present alloy, the term *duplex microstructure* indicates the presence of both the lamellar and equiaxed grain microstructures. In Table 4.1 are summarized the typical mechanical characteristics for both the microstructures, given for two different sizes (fine or coarse). From crack initiation and propagation characteristics two different behaviors are observed depending on the microstructure. Crack initiation is favored by the presence of lamellar colonies, since the most important failure modes are interfacial delamination and decohesion of the lamellar colonies which favor the formation of relatively large initial cracks when one of these mechanism activates [65]. Moreover, other micro-crack initiation mechanisms can be activated due to localized strains induced by blocked twinning on grain boundaries [63], or in triple points where strain incompatibilities are large [64]. The mechanisms for crack initiation are different, and a general statement on the most detrimental one is not yet available, since also many chemical, manufacturing and other factors influences each of these mechanisms. On the other side, crack propagation in lamellar colonies is slower than in equiaxed grains due to the difficulties encountered by a crack to propagate through the lamellar interfaces.

Table 4.1. Mechanical characteristics of the lamellar and equiaxed grain microstructures, from [65].

fine	*coarse*	*Property*	*lamellar*	*equiaxed*
○	○	Elastic modulus	○	+/− (texture)
+	−	Strength	−	+
+	−	Ductility	−	+
−	+	Fracture toughness	+	−
+	−	Fatigue crack initiation	−	+
−	+	Fatigue crack propagation	+	−
−	+	Creep strength	+	−
+	−	Superplasticity	−	+
+	−	Oxidation behavior	+	−

In Figure 4.5 is shown a micrograph obtained after etching a sample, the two different microstructures are clearly observed. Lamellar colonies have a mean fraction in volume of 40%, and a mean colony size of 100 μm, while the equiaxed grained microstructure is characterized by an average grain size of 15 μm [92].

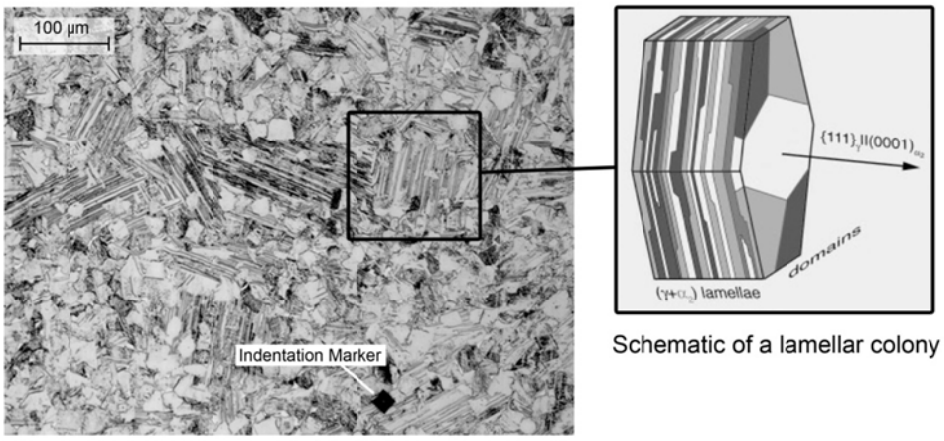

Figure 4.5. Optical microscope image following etching. The microstructure of the material is composed by uniaxial grains and lamellar colonies. In the schematic (from [98]) is reported the typical composition of the lamellae.

Several difficulties arise for adopting an experimental procedure which considers also the micromechanical deformation mechanisms (slip and twinning) as shown in the previous chapters for the FeCr alloy. First of all the average grain size is too small compared with the available strain resolution. It follows that with the adopted DIC experimental set-up, it is not possible to recognize the local strains introduced by slip and twinning separately. On the other hand, the phases inside each of the microstructure have two different crystal lattices, leading to completely different local micromechanical deformation behaviors. These aspects cannot be overtaken with the adopted experimental set-up. The scale adopted in the proceeding will be the length scale which allows to observe differences in the local microstructure, with a clear characterization of the lamellar colonies

and the equiaxed grains, neglecting the micro-scale effects derived by the local crystal structure of the different intermetallic phases.

4.3 Fatigue experiments with plain specimens

4.3.1 Experimental set-up

A set of 60 unnotched specimens suitable for high cycle fatigue testing have been produced (nominal diameter D=6.35 mm) for room temperature (RT) fatigue testing and carried out on a Rumul Testronic test system. Fatigue tests have been conducted by applying the staircase technique and the number of cycles of censored test (runout) has been fixed at 10^7 cycles. Tests have been carried out with three different loading ratio: i) $R=\sigma_{min}/\sigma_{max}=0$ (zero to tension); ii) $R=\sigma_{min}/\sigma_{max}=0.6$; iii) $R=\sigma_{min}/\sigma_{max}=-1$ (pure alternating stress). Prior to fatigue testing, the surface of the specimens has been pre-oxidized, by furnace treatment in air for 20 hr at a temperature of 650°C.

4.3.2 Results

The fatigue experiments results of the set carried out with plain specimens at R=0.6 are shown in Figure 4.6a. In all the experiments the Wöhler curves are extremely independently of the R ratio.

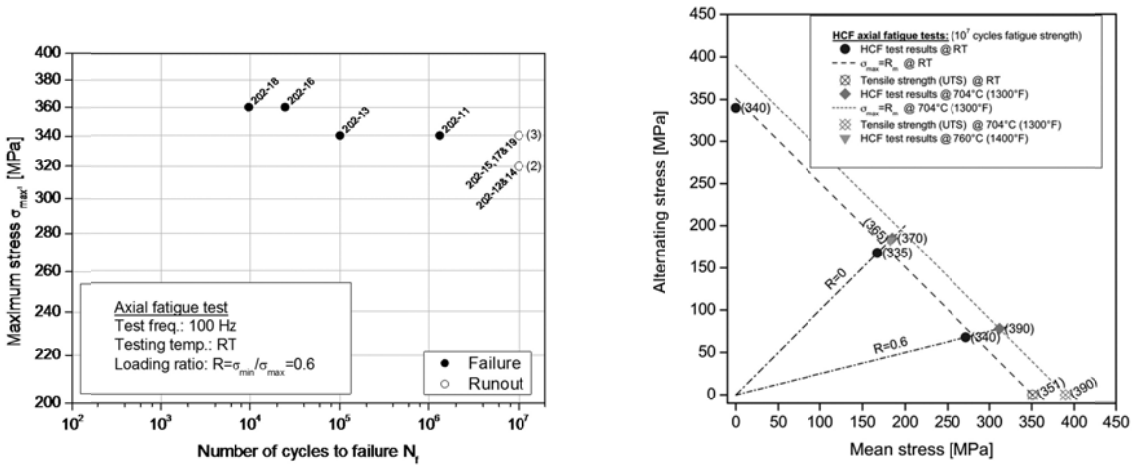

(a) (b)

Figure 4.6. Results from HCF experiments: a) Wöhler diagram of room temperature HCF test results at R=0.6; b) Haigh diagram for the HCF tests with plain specimens.

This means that a small variation in the applied stress amplitude can lead to substantial differences in the number of cycles to failure. The HCF test results obtained in the test campaign can be condensed in a single (Haigh) diagram, Figure 4.6b. By comparing the results at different loading ratios in terms of maximum stress, reported in the diagram of Figure 4.6a in parentheses ( ), it can be

observed that the fatigue limit, in terms of maximum stress, is nearly independent of the loading ratio. In the diagram of Figure 4.6b, the experimentally obtained fatigue limit values lie just below the dashed curve, representing the equation $\sigma_{max} = \sigma_m + \sigma_a = UTS$, where σ_m and σ_a represent the mean and alternating stress, respectively, while UTS is the (minimum) ultimate tensile strength, obtained in earlier experiments. This specific behavior has been observed through all the fatigue experiments with plain specimens, with nearly all specimen failing in the case the applied (maximum) stress was near or above the ultimate tensile strength, with no specimen failing (within 10^7 cycles) for maximum stress equal or below 320 MPa, irrespectively of the loading ratio *R*.

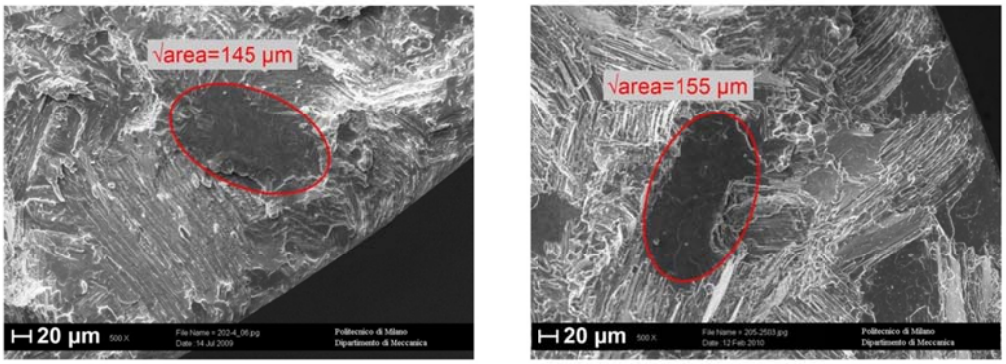

Figure 4.7. Typical nucleation sites observed on the final fracture surface of the fatigue smooth samples.

The fracture surfaces analyzed by SEM (Figure 4.7a-b) reveal that fatigue failures originate from lamellas that, due to their unfavorable direction with respect to that of loading, determine a cleavage initial fracture. One of the mechanisms that can lead to this type of fracture is decohesion of the lamellar packages, due to the elastic incompatibility between the γ-TiAl and α_2-Ti_3Al intermetallic phases. Another potential crack nucleation mechanisms can also be provided by the barrier to slip transmission induced by the interface between two different phases which can lead to micro-cracking [99]. These flat regions observed in the SEM pictures of the fracture surface (Figure 4.7a-b) have a relatively darker area with respect to the surrounding microstructure which allowed to estimate an average *defect* area of about 22000 μm^2, corresponding to an equivalent crack size of √area = 150 µm. The adoption of fatigue samples with initial artificial defects can provide further insights into the potential influence of the microstructure in the crack nucleation process.

4.4 Fatigue experiments with artificial defects

4.4.1 Experimental set-up

A set of 40 specimens with a gauge diameter of 8 mm have been produced, and two type of artificial defects in the form of tiny rectangular micro-slots have been carefully produced in the mid-section of the specimens by EDM, as shown in Figure 4.8.

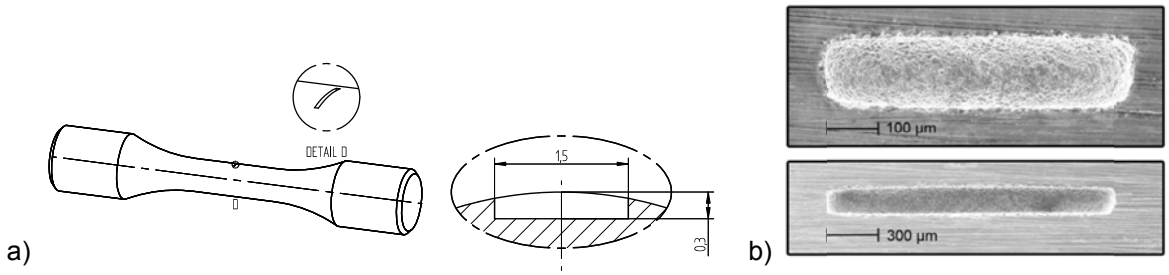

a) b)

Figure 4.8. Geometry of the specimens for assessing defect sensitivity in short crack fatigue experiments (8 mm gauge diameter) and a) nominal shape of artificial defect of $\sqrt{area}$=644 µm; b) SEM picture of artificial defects produced by EDM.

The artificial defects introduced have dimensions of 1500 µm x 300 µm (√area=644 µm) and 500 µm x 100 µm (√area=220 µm), Figure 4.8. In order to generate small cracks at the root of the EDM notches, all specimens with artificial defects have been submitted to a pre-cracking procedure consisting of fatigue loading in cycling compression for a number of cycles up to 10^7 cycles. This procedure ensures that fatigue cracks are generated at the root of the EDM notch by keeping to minimum compressive residual stresses at crack tip. After pre-cracking, all specimens have been pre-oxidized by furnace treatment in air for 20h at a temperature of 650°C, as in the case of unnotched and FCG specimens. Finally, fatigue experiments have been performed according to the staircase procedure at R=0 and R=0.6, with defects with √area equal to 220 µm and 644 µm, respectively.

4.4.2 Results

By employing the Murakami model for the assessment of the range of stress intensity factor (surface defects) as $\Delta K=0.65\Delta\sigma(\pi\sqrt{area})^{1/2}$, the threshold corresponding to the endurance strength for each R ratio can be evaluated. In the plots of Figure 4.9, for loading ratio of R=0 (Figure 4.9a) and R=0.6 (Figure 4.9b) endurance strength stress ranges are given as a function of the equivalent defect size √area. In the case of run-out specimens tested at stress amplitudes corresponding to the fatigue limit, non-propagating cracks has been observed in correspondence of the initial (artificial) defects, Figure 4.10a. A fracture surface of a sample failed at R=0.6 is shown in Figure 4.10b, the red arrows indicate the lamellar colonies where crack propagated through two lamellar colonies.

Fatigue failures in plain specimens were found in correspondence of peculiar microstructural features with a typical size of $\sqrt{area}_i$=150 µm, the modification of the El-Haddad model by Tanaka [100] have been applied in the form:

$$\Delta\sigma_{th} = \Delta\sigma_e^i \sqrt{\frac{\sqrt{area}'_0}{\sqrt{area} + \sqrt{area}'_0 - \sqrt{area}_i}} \quad \text{with} \quad \sqrt{area}'_0 = \frac{1}{\pi}\left(\frac{\Delta K_{th}^{FCG}}{0.65\Delta\sigma_e^i}\right)^2 = \sqrt{area}_0 + \sqrt{area}_i \qquad (4.1)$$

where $\Delta\sigma^i_e$ represents the fatigue endurance strength obtained in the fatigue tests with plain specimens and an inherent defect $\sqrt{area}_i$ of 150 µm has been taken into account both for loading ratio R=0 and R=0.6. If a smaller volume of material would be stressed up to the threshold level, the probability of activating an inherent "microstructural" feature with size $\sqrt{area}_i$ is likely to become lower, i.e. the initial active defect size may be smaller for smaller stressed material volume. Theoretically, as the Kitagawa diagrams in Figure 4.9 reveal, there is a possibility to observe an increased fatigue strength of the material when a non-uniformly distributed loading is applied, as in the case of bending loading of thin sections. Additionally, it may be noted that the size of inherent microstructural features of 150 µm made in the present study is in the range of the colony dimensions [101].

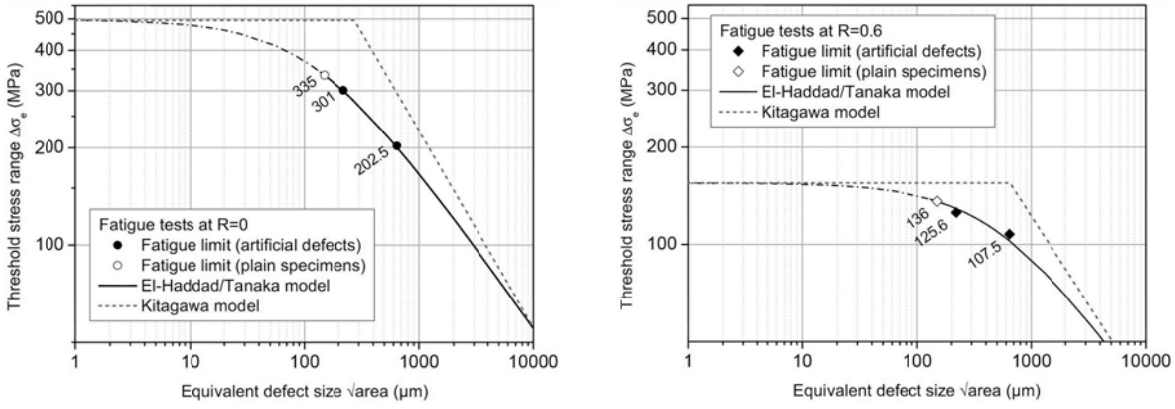

Figure 4.9. Kitagawa diagrams for: a) loading radio R=0; b) loading ratio R=0.6.

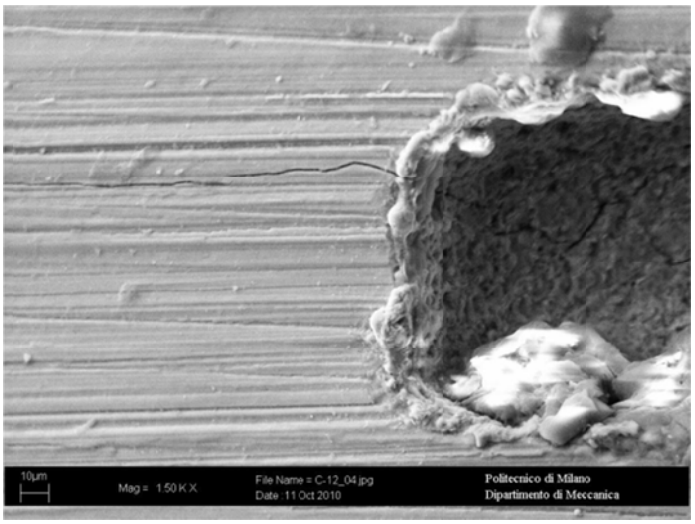

Figure 4.10a. Near threshold fatigue cracks are observed in run-out specimens (Δσ=125 MPa, R=0.6; 10^7 cycles without specimen failure).

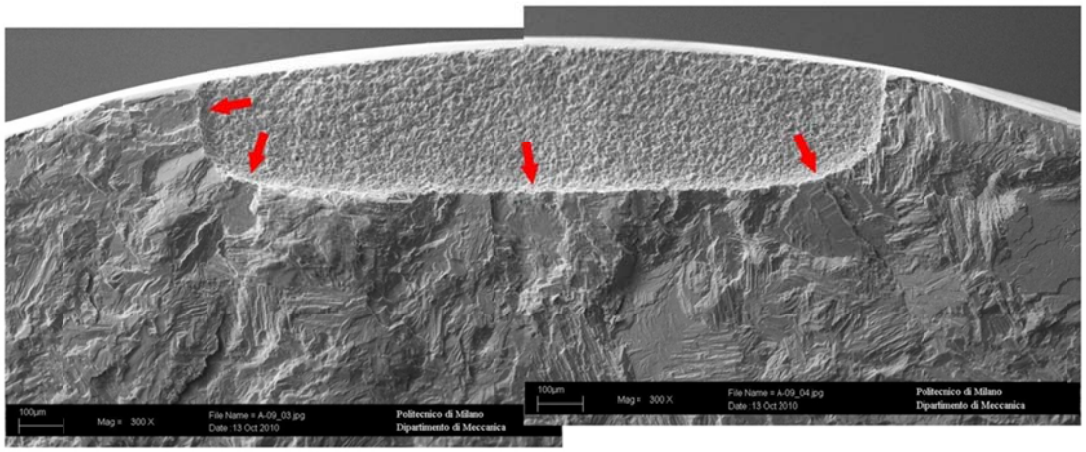

Figure 4.10b. Section of a fatigue sample with an initial artificial defect. The sample failed after 90297 cycles with Δσ=300 MPa at R=0.05. The arrows indicated the '*flat*' regions where the crack propagates through the lamellar packages.

4.5 Fatigue crack growth experiments

4.5.1 Experimental set-up

A smaller set of 6 specimens suitable for crack propagation testing have been produced using a wire EDM for producing the notch (Figure 4.11). The fracture mechanics specimens have been pre-cracked in cyclic compression [102]. Compression pre-cracking (CP) procedure is implemented in order to generate a small crack in front of the notch and thus limit the residual plastic deformations generated in case of pre-cracking procedures using tensile loads. The small yielded region generates local positive (tensile) stresses when the external load approaches zero. These stresses nucleate the crack which propagates and successively stops once reached the initial plastic (in compression)

monotonic region. Using the pre-cracking procedure, the effects of the crack closure at the beginning of the crack growth test are cancelled. Moreover, selecting the appropriate compressive load amplitude the final pre-crack length can be controlled.

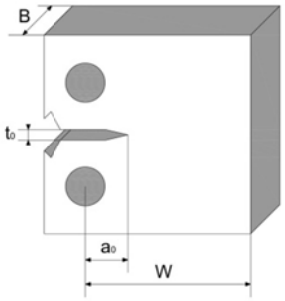

B [mm]	W [mm]	t_0 [mm]	a_0 [mm]
12.7	25.4	1.5	6.5

Figure 4.11. Sample geometry for crack growth experiments.

For starting a crack in cyclic compression the wire EDM starter notch was sharpened by a razor blade polishing technique (Figure 4.12).

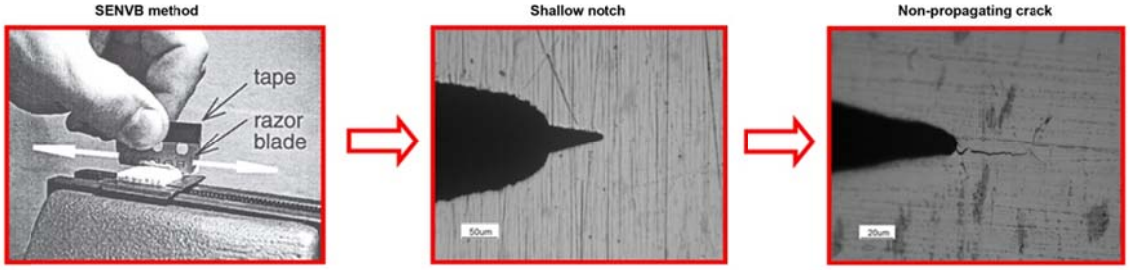

Figure 4.12. SENVB method applied to the original notch in order to obtain a shallow notch which display high localized strains and stresses. This methodology enables nucleation of non-propagating small cracks in front of the original notch.

Fatigue crack growth tests have been carried out by means of a servo-hydraulic MTS 810 testing machine (Figure 4.13a) and the crack length monitored by COD gage (Figure 4.13b). In order to determine the threshold stress intensity factor for long cracks ΔK_{th} and the long crack propagation behavior, fatigue crack growth tests at room temperature have been carried out at constant R ratio (R=0.05 and R=0.6) by increasing the applied ΔK (load amplitude) in small steps until the threshold value for a long crack is reached.

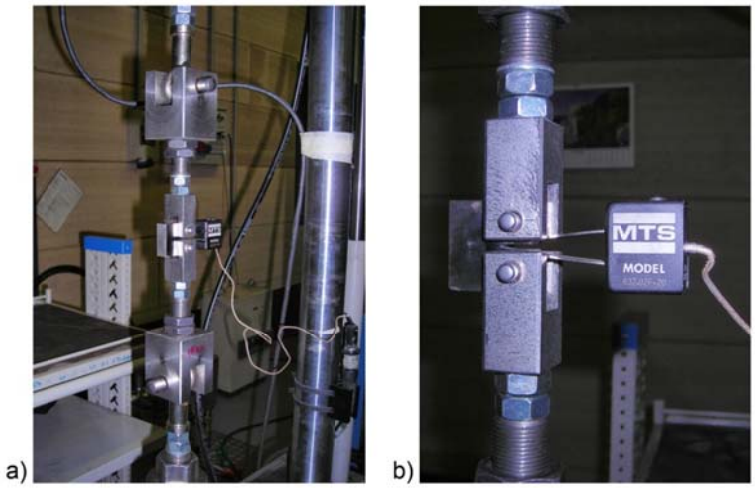

Figure 4.13. Experimental set-up for crack propagation experiments, a) load frame and grip set-up; b) particular of the COD gage for the measure of the crack length.

4.5.2 Results

In the fatigue crack growth experiments a coherent behavior was observed: for the tests conducted at R=0.05 no crack growth was observed for ΔK below 6 MPa$\sqrt{m}$, while for the tests at R=0.6, ΔK_{th} is about 4 MPa$\sqrt{m}$. Two crack growth curves for each load ratio R are reported in Figure 4.14. Each crack growth curve displays a similar crack propagation behavior. In particular, in any of the analyzed cases was observed a stable crack propagation behavior, while several instantaneous crack advancements were measured when the load was increased.

- Crack growth curve 1 (Figure 4.14a), R=0.05. Initially, the sample was cycled for about 3.25×10^6 cycles (with a final ΔK=5.77 MPa$\sqrt{m}$) and a small crack advancement was observed. Following an increment of the applied load amplitude (from ΔK=5.77 MPa$\sqrt{m}$ to ΔK=6.13 MPa$\sqrt{m}$) an instantaneous crack advancement of Δa=0.6mm was observed. Holding the load at ΔK=6.13 MPa$\sqrt{m}$ for about additional 1.5×10^6 cycles didn't lead to appreciable crack propagation. A further small increment of the load (from ΔK=6.13 MPa$\sqrt{m}$ to ΔK=6.70 MPa$\sqrt{m}$) started the fast crack propagation which quickly conducted the sample to the final failure.

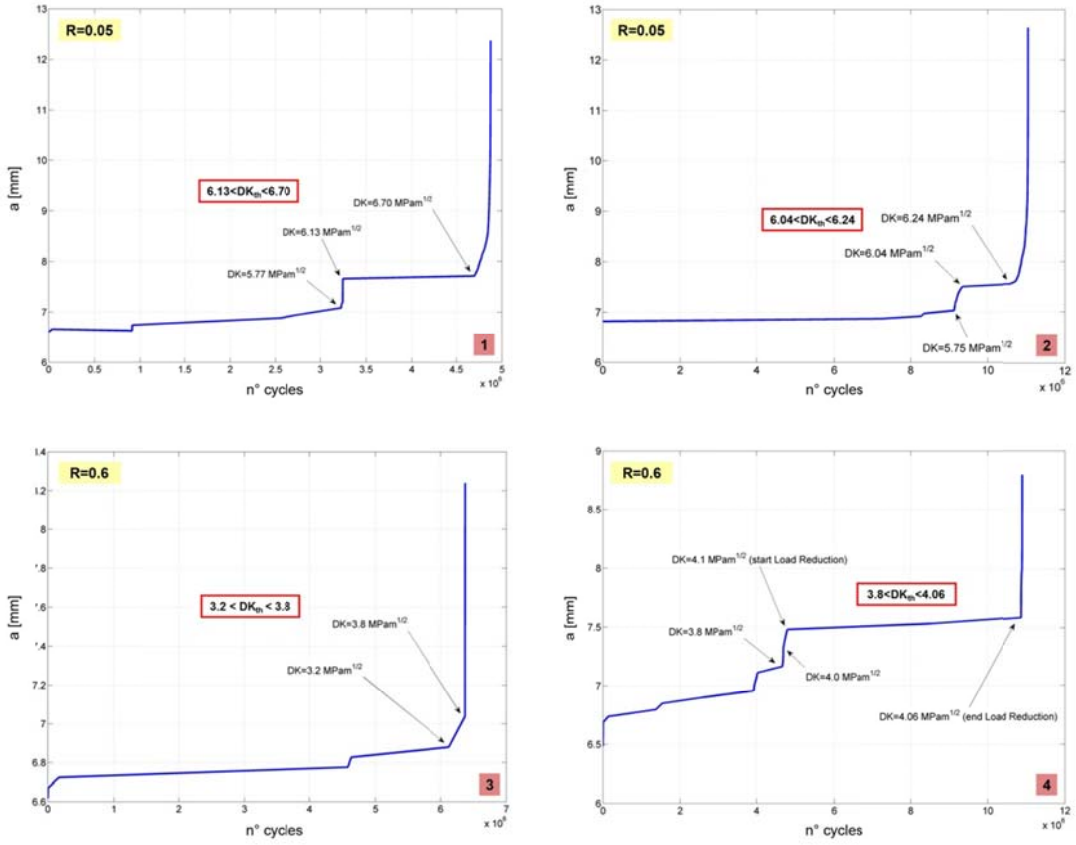

Figure 4.14a. Crack growth curves from different samples. Crack growth curves 1 and 2 refers to experiments conducted at load ratio R=0.05, while 3 and 4 to experiments conducted at load ratio R=0.6.

- Crack growth curve 2 (Figure 4.14a), R=0.05. The initial load was hold at a constant ΔK=5.75 MPa$\sqrt{m}$ for more than 9x10^6 cycles without appreciable crack advancement. A small load increment was successively applied (from ΔK=5.75 MPa$\sqrt{m}$ to ΔK=6.04 MPa$\sqrt{m}$) which produced a small crack advancement of Δa=0.5mm. A further load increment (from ΔK=6.04 MPa$\sqrt{m}$ to ΔK=6.24 MPa$\sqrt{m}$) generated the fast crack propagation.

- Crack growth curve 3 (Figure 4.14a), R=0.6. Similar crack growth behaviors were observed also for the experiments carried out at a load ration R=0.6. For crack growth curve 3 a load amplitude equivalent to ΔK=3.8 MPa$\sqrt{m}$ was required to start the propagation which basically doesn't display any stable crack propagation region. In fact, in the first two crack growth curves, 1 and 2, the final propagation stage was *"almost-unstable",* but not *"totally-unstable"* (as cases 3 and 4). In the previous cases, this characteristic of the final crack growth curves enabled to measure several points for the fatigue crack growth rate curves (Figure 4.16).

- Crack growth curve 4 (Figure 4.14a). In this case was implemented the load reduction technique in order to measure the threshold stress intensity range ΔK_{th}. The crack was grown to a final value of a=7.5mm for 5x10^6 cycles, at this point (ΔK=4.1 MPa$\sqrt{m}$) the load reduction

procedure was implemented. The load reduction procedure consists of progressively reducing the applied ΔK while the crack is propagating till the crack front stops. As clearly displayed on the crack growth curve 4, the crack didn't stop during this procedure. This implies that the value of the threshold is contained in the interval from ΔK=3.8 MPa√m (where we first observed a crack advancement) to ΔK=4.06 MPa√m (which corresponds to the load of the unstable propagation).

The crack growth curves presented here allowed to provide two main considerations. First of all crack growth curves display a *non-linear* crack growth behavior which characterizes *non-linear crack paths* due to local microstructural effects [103, 104]. Figure 4.15 shows two images obtained at early stages of small crack propagation for which is evident the non-linear character of the crack propagation. The local microstructure strongly influences the small crack growth behavior. In particular, the crack encountered lamellar colonies which are not well oriented and provided a local barrier to the crack advancement. In this scenario, a load increment (and so also an increment of the applied ΔK) is necessary to advance the crack. This effect is beneficial in terms of resistance of small crack propagation since it increases the range of stress intensity threshold ΔK_{th} with crack advancements (Figure 4.14b).

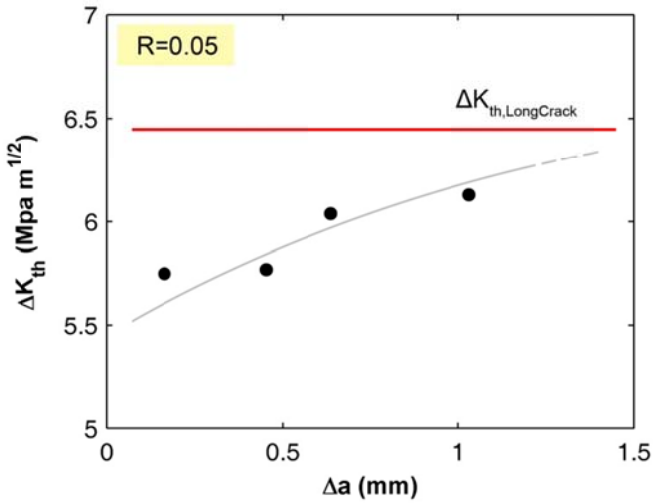

Figure 4.14b. Variation of the stress intensity threshold range with the increment of the crack length. Data extrapolated from the crack growth curves reported in Figure 4.14a from experiment at R=0.05.

The increment of ΔK_{th} with crack advancement for small crack lengths can be correlated to the progressive development of crack closure effects. In their work, Garcia and Selhitoglu [103, 104] explained that the observed closure effects (especially when the crack is small) derive from local sliding of the crack flanks induced by the non-linear nature of the growing crack due to microstructural effects. This effect becomes important especially for materials that exhibit low

plasticity-induced closure (as in γ-TiAl alloys). This consideration is also important in order to explain the difference in the crack growth rate curves reported in Figure 4.16a-b.

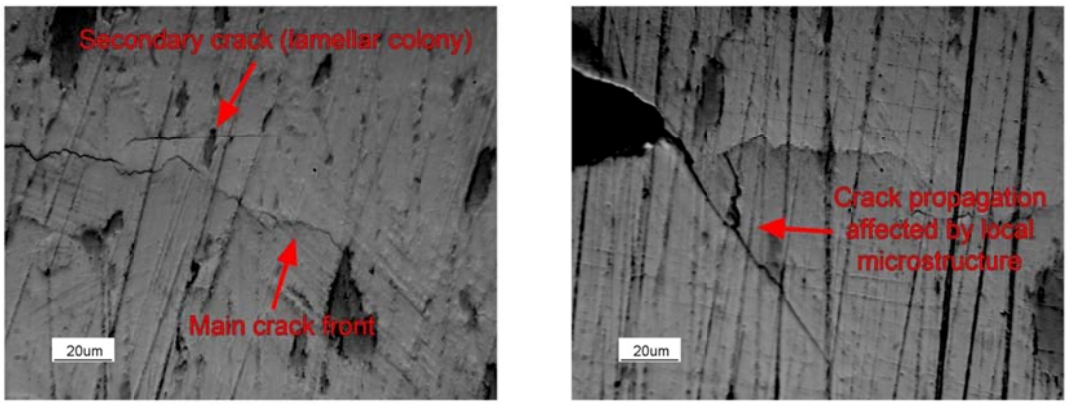

Figure 4.15. Non-linear crack paths at early stages of propagation due to local microstructural effects.

Two different abscissa were used, in particular in Figure 4.16a was used the stress intensity factor range ΔK, while in Figure 4.16b was used the maximum stress intensity factor of the cyclic load K_{max}. The critical K_{max} value, corresponding to specimen failure, is in the range 10.5-11.5 MPa$\sqrt{m}$, independently of the applied $R=K_{min}/K_{max}$ ratio. The threshold values determined here are in accordance with those reported in literature for the duplex microstructure of γ-TiAl alloys [105]. It can be observed that the available ΔK range for crack growth is rather limited, due to the relatively limited difference between ΔK_{th} and K_{max}, resulting in high value of the slope. Even if a direct comparison with other data published in the literature are difficult, due to different heat treatment and process route, resulting in different microstructures for the same (nominal) chemical composition, it may be observed that the γ-TiAl produced with the EBM process employed here offer superior fatigue crack growth threshold characteristics with respect to those of TiAl alloys obtained by conventional PM process [62, 105], where a ΔK_{th} of about 5 MPa$\sqrt{m}$ for R=0.1 was reported.

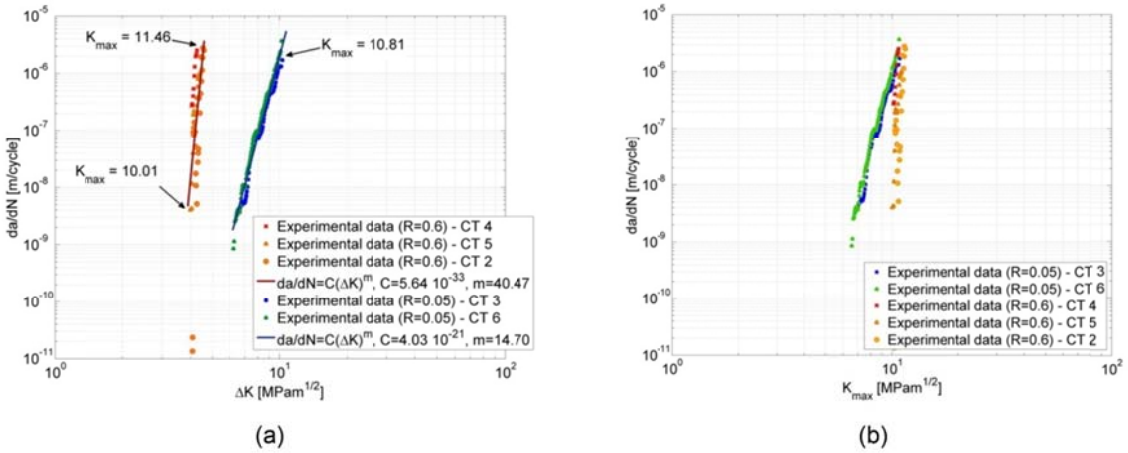

Figure 4.16. Fatigue crack growth rate curves in terms of: a) ΔK, range of stress intensity factor (SIF); b) maximum SIF in the loading cycle K_{max}.

The observed difference on the crack growth rates for different load ratios is considered related to the non-linear crack growth induced closure which is typical of materials with lamellar microstructure.

4.6 Uniaxial static experiments using DIC

4.6.1 Experimental set-up

Local damage effects induced by the material microstructure are studied using high resolution strain measurements through digital image correlation (DIC) methodology. Special plane sample geometries for uniaxial tension/compression experiments were adopted, Figure 4.17.

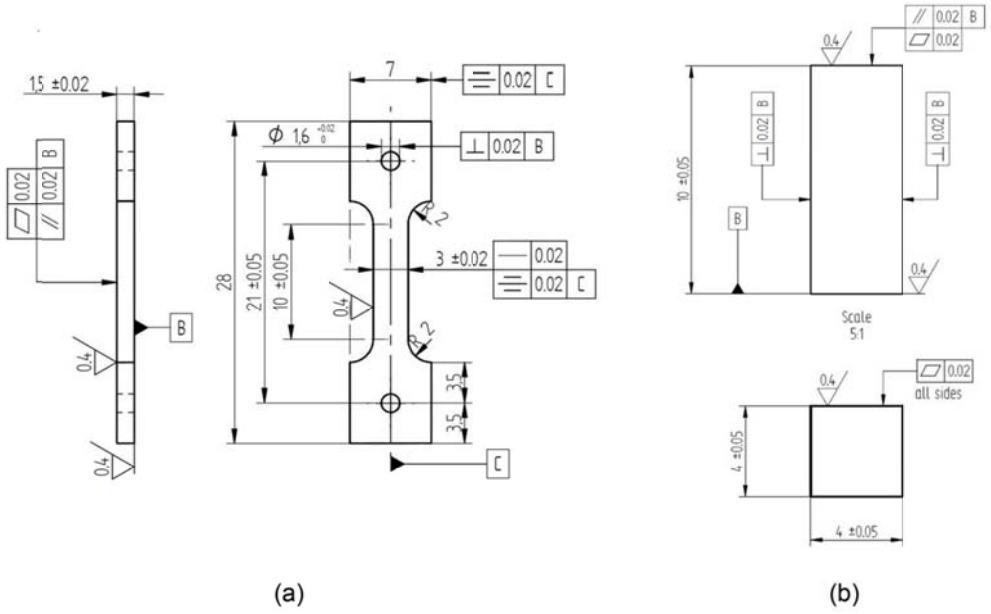

Figure 4.17. Geometry of the specimens for uniaxial static experiments using digital image correlation in a) tension and b) compression.

In particular, tensile dog-bone shaped specimens with a 1.5 mm x 3 mm cross-section and a 10 mm gage length and compression samples sectioned into 4 mm x 4 mm were produced by electro-discharged machining (EDM) with the required tolerances. Tension and compression experiments were conducted in displacement control at a strain rate of about $5x10^{-5}$ s^{-1}. High resolution ex situ DIC was used to measure the residual strain field and correlate it with the microstructure of the material [66]. For *in situ* DIC, reference and deformed images were captured using an IMI model IMB-202 FT CCD camera (1600 x 1200 pixels) with a Navitar optical lens, the resolved resolution was 3.0 μm per pixel.

Figure 4.18. Preparation of the TiAl samples. The samples are polished with SiC paper (from P800 up to P4000), and successively etched.

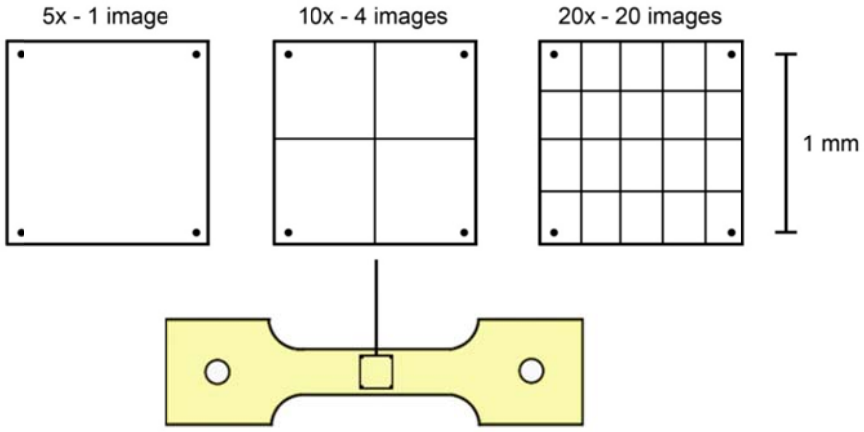

Figure 4.19. The sample has been marked with four Vickers indentation markers at a corner of a 1 x 1 mm^2 square region. This region has been analyzed capturing images with the optical microscope at different magnifications.

For *ex situ* DIC, an optical microscope was used to capture the reference and deformed images. The increased imaging magnification improves the DIC measurement resolution (3.0 μm/ pixel versus

0.44 µm/pixel for *ex situ*) and enables better characterization of the local strain magnitudes in the lamellar and equiaxed grains, respectively. Prior to etching, the samples were polished with different paper grit sizes (from 1200 to 2500), and a fine polishing with diamond paste (6, 3 and 1 µm), Figure 4.18. The 1 mm x 1 mm region covered with ex situ DIC is depicted in Figure 4.19, using different optical microscope magnifications the number of images required for covering the target area changes.

4.6.2 Results

In situ DIC was used to measure the evolution of local strains during the loading for both the tension/compression specimens. The stress-strain curves for tension/compression static experiments were derived averaging the DIC axial strain measurements in the monitored region of the sample surface, Figure 4.20. As expected, in tension the alloy displays low ductility, while in compression it is possible to reach higher deformations.

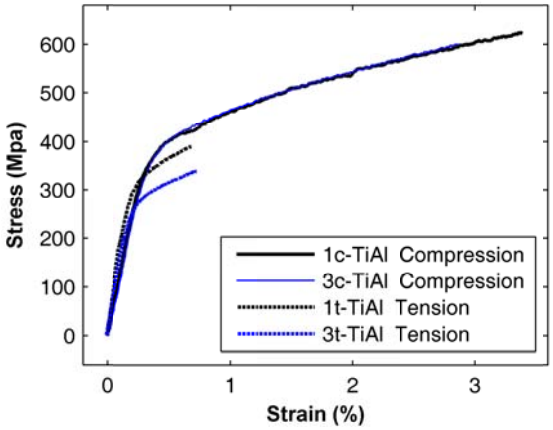

Figure 4.20. Summary of the experiments conducted on TiAl samples. Tension samples fractured at less than 1% of nominal strain, while compression samples were tested up to 3%.

The compression experiments were conducted in displacement control. Adopting in-situ DIC is possible to monitor an area of the sample and average the strains in the load direction in order to obtain the stress-strain curve reported in Figure 4.20.

4.6.3 Compression experiment

Figure 4.21 shows the strain field for a compression sample with a residual average deformation of 2.5%. In compression. As already shown in using the stress-strain curves, with a compressive load it is possible to reach higher strains. In this case clear local strain accumulations are easily detected, an example of these regions is shown in the zoomed region of the strain field in Figure 4.21. In the highlighted box is shown the effect of the different orientation of two packages of lamellar grains. For

the present level of the analysis is not possible to determine the third component of the lamellar plane which respect to the load direction. Nevertheless this limitation, it is clear how a favorable-oriented lamellar colony (on the left inside the analyzed strain field selection, Figure 4.21) displays high residual strains, while for the other lamellar colony no residual strains were observed.

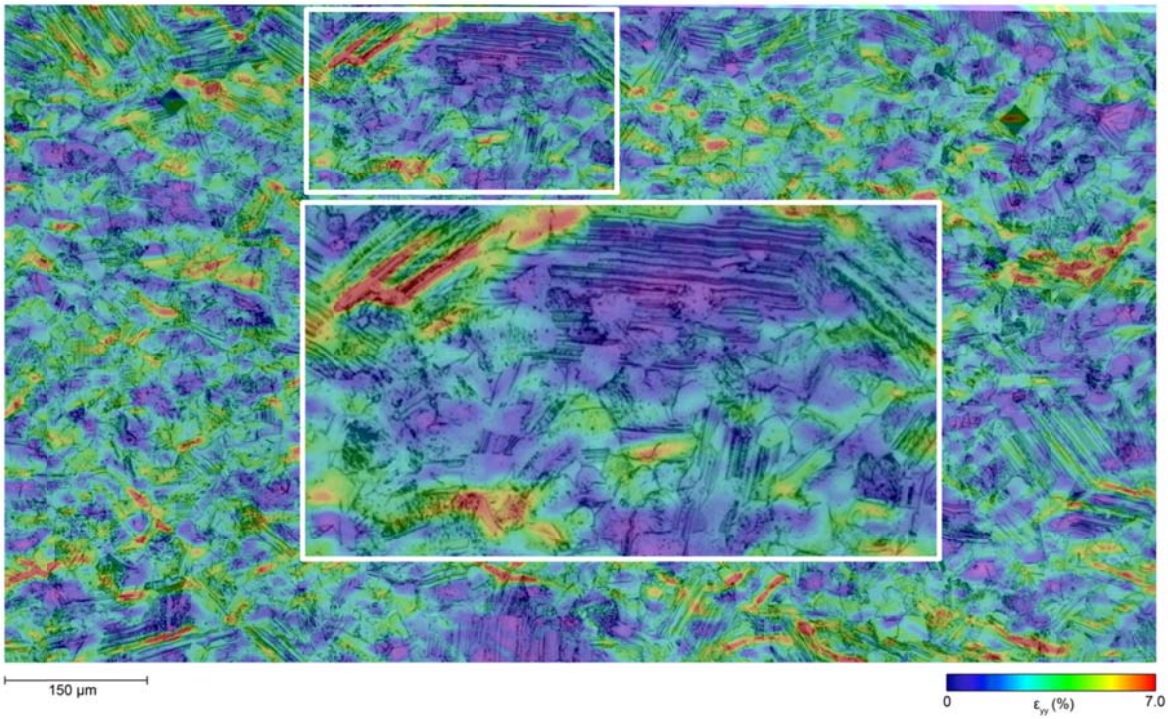

Figure 4.21. Example of ex situ high resolution DIC overlapped with the material microstructure map obtained after etching. The strain filed refers to the strain in the load direction. In the selected region is possible to observe two lamellar colonies that display different strain fields. On the lamellar colony on the left strain localization up to 7% are observed, while on the colony on the right is almost free of residual deformation. The localized strains observed in the lamellar package confirms the decohesion mechanism between lamellar colonies already observed in the HCF experiments.

4.6.4 Tension experiment

Under tensile loads, the analyzed material shows the typical brittleness of TiAl alloys (see comparison between compression-tension stress-strain curves in Figure 4.20). The stress-strain curve of the tension experiment analyzed is reported in Figure 4.22. The sample failed at a maximum stress of about σ=400 MPa at a deformation of up to 0.7%. Ex-situ DIC was implemented at an intermediate loading step. The sample was statically loaded till a maximum stress of σ=350 MPa and successively unloaded till a final residual deformation of 0.24% (the unloading part of the diagram is not reported in the stress-strain curve). In this case, it is expected much lower strain localizations than the compression case. This analysis is only a first attempt to understand the effect of the local microstructure on the local strain fields in tension, and newel experiments will be implemented introducing cycling loadings.

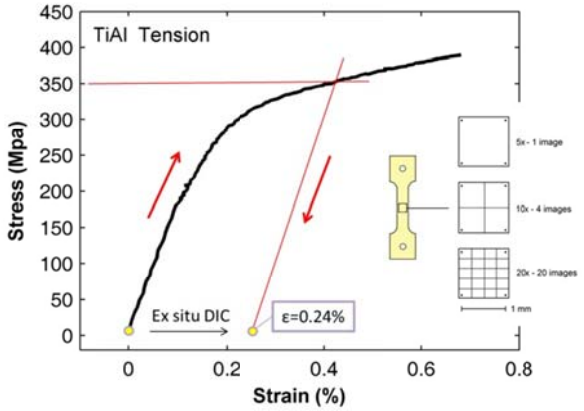

Figure 4.22. Stress-Strain curve for the tension experiment. Correlation between reference images and deformed images has been implemented out of the load frame (ex-situ) with an average residual strain of ε=0.24%.

Figure 4.23 reports the residual strain field for a selected rectangular region of the sample surface of about 340 μm x 640 μm, successively overlapped with the images of the microstructure obtained capturing the images before the experiment. A smaller region of 225 μm x 225 μm displaying high localized residual strains was successively selected and analyzed.

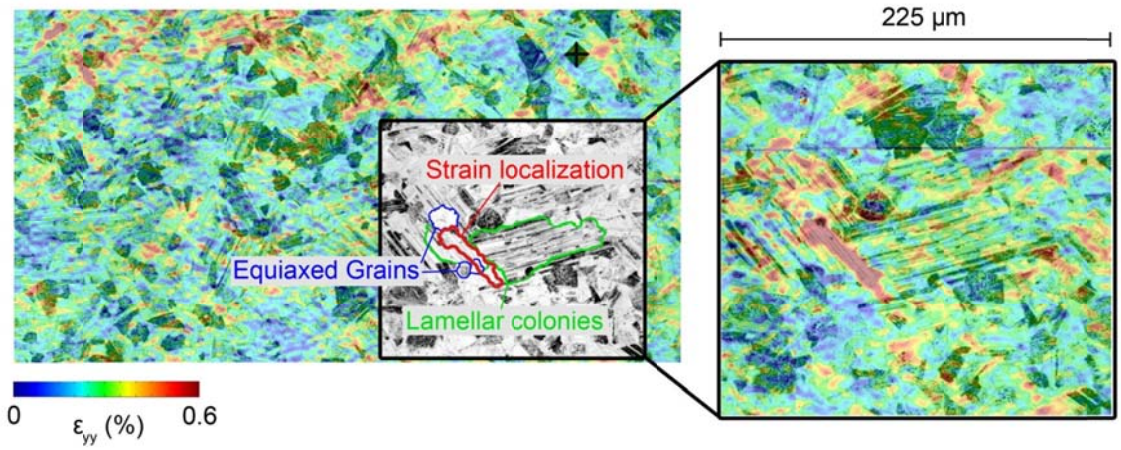

Figure 4.23. Strain plot for a region of the sample with an average residual deformation of 0.24%. Localization of strains are measured in different locations of the microstructure; in particular on the region analyzed the high localized strains nucleate on the interface regions between two lamellar colonies.

From the local residual strain field and the schematic of the local microstructure is evident that the region of high localized strains propagates along the interface between the lamellar colonies and intersects also the interface with the upper grain.

4.7 Final considerations

A potential disadvantage of cast and PM γ-TiAl alloys, in terms of component design, is their limited fatigue crack growth resistance and damage tolerance. Additionally, in the case of cast and conventional PM TiAl alloys, due to the unfavourable combination of fatigue crack growth threshold, propagation behaviour and bigger inherent defects-porosity, non-metallic inclusions and metallurgical defects, like dendrites, the usable fatigue endurance strength may be quite limited. In general, there is a small difference between the fatigue threshold stress-intensity-range of long cracks and the apparent fracture toughness, leading to shortened lifetimes for small changes in applied stress. For the analysed Ti-48Al-2Cr-2Nb alloy, the manufacturing process adopted (EBM) allows to avoid the typical defects of cast or PM materials, providing higher fatigue threshold and fatigue strength.

In this chapter were firstly depicted the results adopting the classical fatigue experiments. Fatigue experiments were implemented on fatigue specimens with an artificial defect, in this case the fatigue threshold were estimated for two different initial defect depths. The experimental results can be accurately described by a modified El-Haddad model, see equation (4.1). In Figure 4.9 is reported the equation representing the adopted model, along with the experimental fatigue limits for the samples with the artificial defects. In addition, the results obtained for plain samples are also reported in the same diagrams (see Figure 4.9). HCF limits for plain specimens are required to be translated at an initial defect size of $\sqrt{area}_i$ of 150 μm for both for loading ratio R=0 and R=0.6 in order to match the prevision made with equation (4.1). This fundamental consideration points to the fact that nevertheless the material is *free* from initial manufacturing defects, the fatigue limits for smooth samples display values which can be explained only assuming the presence of initial defects with an average size of $\sqrt{area}_i$=150 μm. Analyses of the fracture surfaces show the presence of *flat* areas corresponding to the lamellar colonies which are considered to be potential crack initiation sites (Figure 4.7). In particular these regions display an average area $\sqrt{area}_{LamellarColonies}$=150 μm which corresponds to the observed initial crack length defect $\sqrt{area}_i$. Not only fatigue limits are affected by the microstructure, but also the small crack propagation, and thus stress intensity threshold ranges (section 4.4). The lamellar colonies are observed to provide an initial tortuous crack path which provides barriers to crack advancement when the crack front encounters unfavourable lamellar packages (see micrographs in Figure 4.15). Moreover, roughness induced crack closure also develops as a consequence of the non-linear crack path (Section 4.5.2). This observation suggests that the reduction of the grain size is potentially detrimental for the capability to develop roughness-induced crack closure, thus reducing the crack propagation resistance of the alloy.

Along the classical experimental approaches just discussed, in this chapter is also introduced the implementation of high resolution DIC for determining the local effect of the material microstructure on the strain fields. The results presented using DIC strain fields clearly confirm the critical role on

crack initiation played by the lamellar grains previously argued. The high local strains reported in Figure 4.21 and 4.23 are discovered to originate along the lamellar colonies, and along the interfaces between the lamellar colonies and the equiaxed grains. Similar results were introduced to explain the fracture surfaces discovered after the experiments on the smooth samples (Figure 4.17). Of course, from this analysis is not possible to detect the exact point where, successively, cracks originate. More analyses are required, in particular adopting post-analyses via SEM. A combination between crack locations using SEM images and the present strain maps (Figures 4.21 and 4.23) can be useful for assessing a potential correlation between the regions displaying the highest strain localizations with the regions which, successively, favor crack initiation. Again, the present results suggest that the advantage of using DIC strain maps provides simultaneous analysis of several microstructural locations on significant sample's areas (damage-map of the potential and more detrimental microstructural features). In this way, the choice of the best compromise for the microstructure composition (volume fraction of equiaxed/lamellar grains and average grain size) based on the design requirements can be operated.

Chapter 5

Concluding Remarks and Future Developments

5.5 Concluding Remarks

In order to continuously improve the knowledge of the material behavior and provide more reliable models able to correctly predict the stresses and deformations inside components, newel experimental approaches are required to follow the natural evolution of the research. This work presented the usage of a promising experimental approach which is able to link the material behavior on the microscopic scales with the material behavior on the meso and macro scales through *local strain measurements*. High resolution strain fields have been obtained from Digital Image Correlation (DIC), and the combination of these results with the microstructural information of the alloy provided important conclusions on bcc crystal plasticity, and on damage accumulation on γ-TiAl alloys. The main results obtained are summarized in the following paragraphs.

5.1.1. Results of Chapter 2

In Chapter 2, the results provide the basis for discussion of pertinent issues regarding deformation in bcc materials when both slip and twinning occurs, and support the following conclusions: (i) the observed stress-strain behaviors are classified in four different Cases (schematic in Figure 2.5) based on the activated mechanisms (twin/slip) that lead to a different crystal hardening (twin-twin and twin-slip interactions display higher hardening than slip-slip interactions). (ii) For *Case* I (twinning dominated) is observed a lower critical resolved shear stress for twin migration (124 MPa) compared to the *Case* II (153 MPa) where twin nucleation is preceded by significant slip activity. (iii) Twin nucleation occurs at an average critical resolved shear stress of 190 MPa. For the cases analyzed in this study this observation suggests that a critical shear stress for twin nucleation holds to a first approximation. (iv) The nucleation of slip occurs at an average critical resolved shear stress of 90 MPa and always precedes twin nucleation. (v) Local strain measurements are provided on twin-twin and twin-slip intersection regions for two specific crystal orientations. Twin-twin intersections lead to higher strain localizations (up to 10%) compared to the twin-slip case (up to 6%).

These conclusions provide deep insight into deformation behavior of bcc alloys, in particular on the active deformation mechanisms based on the crystal orientation. Moreover, strain fields can be used as a check of crystal plasticity calculations.

5.1.2. Results of Chapter 3

In Chapter 3 were investigated dislocation-grain boundary interactions for a FeCr alloy using strain fields determined by digital image correlation. Strain fields across GBs provide a direct quantification of the GB capability to transmit or block slip dislocations. The study elucidates the role of the residual Burgers vector magnitude in predicting full/partial slip transmission, or slip blockage. Along the Chapter are provided the strain fields across four GBs displaying different residual Burgers vector magnitudes. In particular, for low $|\vec{b}_r| \to 0$ no residual dislocation is left on the grain boundary. In this case slip is observed to transmit unaltered across the interface and the resulting strain field is continuous. For intermediate $|\vec{b}_r| = (0.2 \text{ to } 1)a$, depending on the $|\vec{b}_r|$ magnitude a step on the strain field is observed on the interface that represents the strain accumulation on the GB side of the incoming slip system. Finally, for high $|\vec{b}_r| > 1a$, dislocations are blocked at the grain boundary, and high strain accumulation is measured on one side of the grain. The results clearly show a direct correlation of the strain change across the interfaces with the $|\vec{b}_r|$ magnitude thus indicating the possibility to use the $|\vec{b}_r|$ as a parameter for predicting the slip transmission capability of the grain boundaries in a polycrystal material.

5.1.3. Results of Chapter 4

In the case of the Ti-48Al-2Cr-2Nb alloy examined in Chapter 4, the advantage of the γ-TiAl produced by the EBM process is that typical defects of cast or PM materials can be avoided and higher fatigue threshold and fatigue strength with respect to competing technologies can be obtained. Thus, the experiments carried out on this duplex γ-TiAl alloy allow to focus on the influence of the microstructure (lamellar and equiaxed grains) on the fatigue properties. From the observation of the experimental results the following conclusions may be drawn. (i) The fatigue experiments with artificial defects show that ΔK_{th} for defects larger than 100-150 μm can be described very accurately by a modified El-Haddad relationship, taking into account the inherent microstructural features of the material; the values of the threshold stress intensity factor range depend on the loading ratio R, so that the mechanism does not seem to be governed by $K_{max.}$ only, as it might be assumed from the fatigue experiments with un-notched specimens at different R ratios. This apparently simple material model, illustrated in the diagrams of Figure 4.17 gives to the designers useful indications about the influence of defects size on the fatigue endurance strength that may employed for the safe design of gas turbine components. (ii) High resolution DIC strain fields were also measured in conjunction with

microstructural maps for determining the local effect of the material microstructure and locate potential micro-crack sites. From the static uniaxial tension/compression experiments were observed high localized strains accumulated along lamellar colonies and in the interfaces regions between lamellar and equiaxed grains. (iii) Further experiments adopting high resolution DIC will be carried out under cyclic loads in order to obtain more detailed damage maps of the microstructure. As shown in this work, these tools provide valuable information on the microstructure *design* (volume fraction and average size of the lamellar and equiaxed grains) in order to reach the required mechanical properties.

5.2. Future developments

Following the experiments depicted in the preceding chapters, some possible developments on the DIC technique, and some different applications are here presented. Some of these results refer to experiments obtained by the author and aim to provide further insight for future research works. The aim of this chapter is to show potential advanced applications of the experimental methodology adopted. In section 5.1 is presented an application of the in situ DIC methodology at high temperature (400°C) for a FeCr single crystal with $[\bar{1}0\,\bar{1}]$ crystal orientation. A comparison between the strain fields obtained at room temperature (chapter 2) and at high temperature is shown. In section 5.2 a promising application of ex situ DIC via SEM is investigated for studying twin-twin interactions. The strain field in correspondence of a twin-twin intersection is analyzed and the improvements obtained using these high resolution images are compared with the previous strain field resolutions available.

5.2.1. High Temperature experiments on FeCr

One of the main issues in the usage of DIC at high temperature arises with the choice of the correct speckle. In fact, the increment of the temperature introduces difficulties in generating a speckle patter that doesn't change during the experiment. Paint burning and oxidation are the main sources of modification of the speckle pattern during the experiment. If the experiment is particularly long (e. g. fatigue, creep, etc.) these problems can void the strain measurements. Different solutions for producing the speckle are available depending on the type of the experiment. The experiments carried out in this study are all static experiments, in this case the duration of the experiment is limited. Moreover also the temperature is limited (400°C). This allows to use the same type of speckle patter (black pain applied with an Iwata airbrush) providing that the speckle is pre-heated before the experiment.

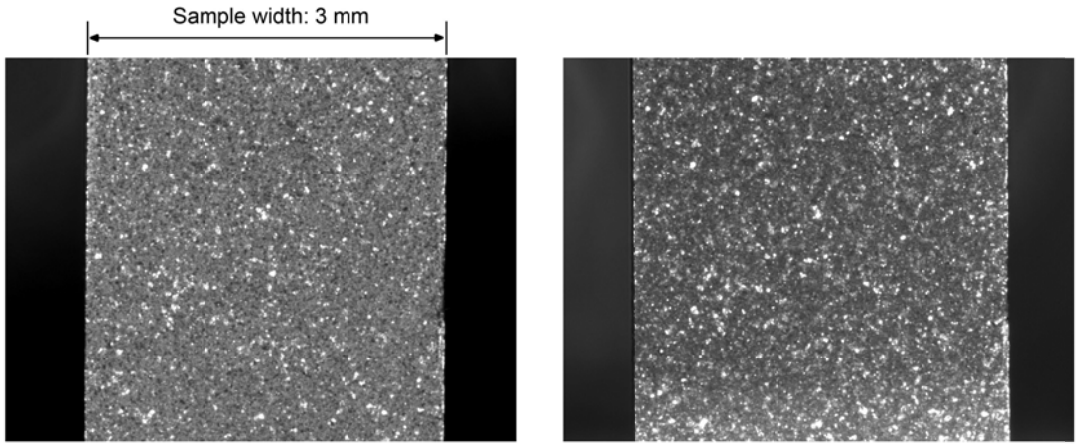

Figure 5.1. Comparison between the speckle patter produced with the Iwata airbrush at (a) room temperature, and (b) after heating the sample at 400 C. The sample heating preceding the experiment is necessary for the stabilization of the black paint at 400 C.

The pre-heating phase induces a modification on the original speckle patter, which can be seen on Figure 5.1. Figure 5.1a shows the speckle pattern used for room temperature experiments, while Figure 5.1b shows the same sample heated up to 400 °C using load control with nominal stress σ=0.

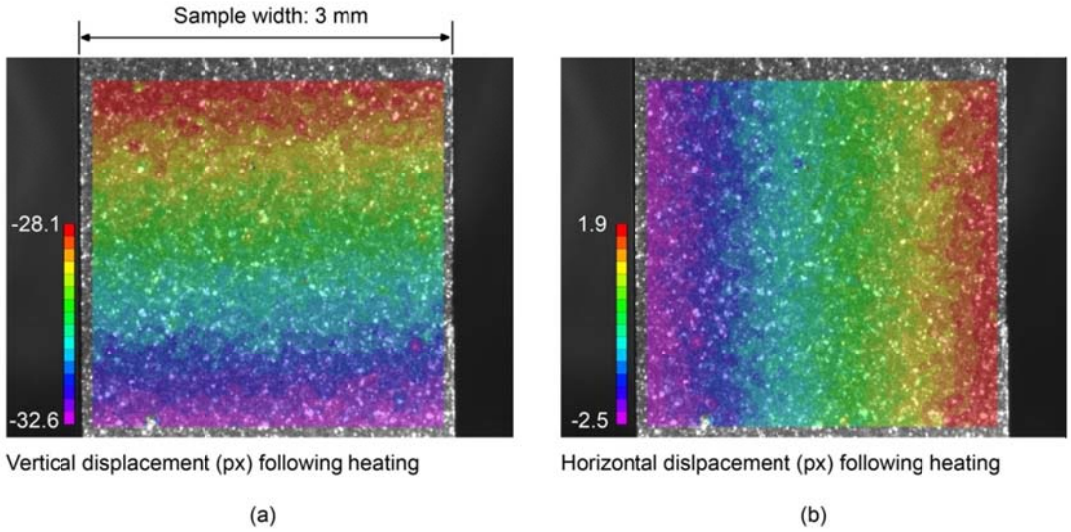

Figure 5.2. The sample heating produces elongations in the (a) vertical, and (b) horizontal directions. The measure of the displacement using DIC allows to verify the homogeneous distribution of the displacement, and verify eventual dis-homogeneities on the induction heating. Moreover it is possible to verify also the correct alignment in the sample-grips system.

This procedure enables to stabilize the speckle pattern, it is so expected that limited modifications occur to the speckle pattern during the experiment. Following the pre-heating phase, the sample is heated again at the test temperature (400°C). During this procedure some images are acquired, and a final correlation between the surface at room temperature and the surface at high temperature is

available. The displacement filed (Figure 5.2) can be used to verify the correct deformation of the sample induced by the temperature gradient, and so is an indirect verification of the grips-sample set-up. The experiment is conducted in displacement control, and the nominal strain is determined from the averaged strains obtained from the DIC strain fields.

In figure 5.3 is proposed a comparison between the room temperature (23 °C) and high temperature (400 °C) experiments for the $[\bar{1}0\,\bar{1}]$ crystal orientation.in tension. Comparing the stress-strain curves obtained two main observations are evident. First of all the nominal yield stress decreases with the temperature ($\sigma_{RT} = 420MPa$ and $\sigma_{HT} = 330MPa$). Secondly, the stress-strain curve for room temperature is smooth, while for the high temperature experiment are observed small load drops.

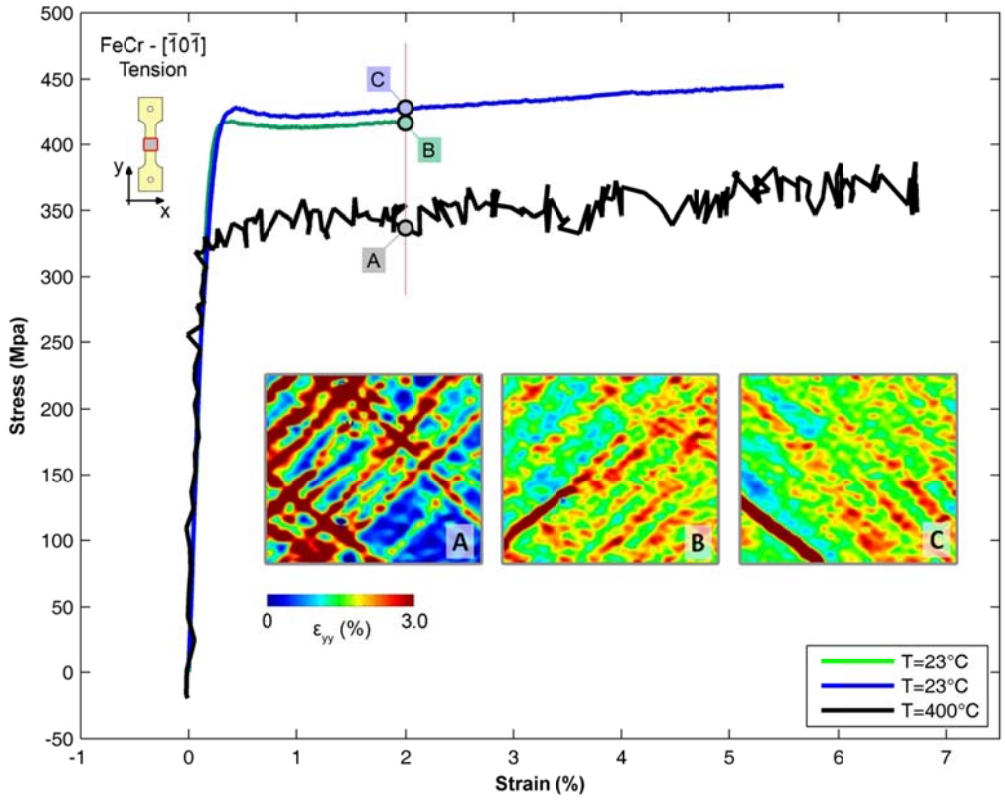

Figure 5.3. Comparison between room temperature (23°C) experiments (B and C), and high temperature (400°C) experiment (A). As expected, increasing the temperature decreases the yield stress. At high temperature two slip systems are activated, the nucleation of the slip bands leads to small load drops in the stress-strain curve.

Digital Image Correlation enables also to compare the strain fields at the same nominal strain. Inset marked A in Figure 5.3 displays the strain field for the high temperature experiment, while inset marked B and C show the strain fields for the room temperature experiments. Both strain fields display two activated slip systems as described in Chapter 2. At the same nominal strain (points A-B-C) the strain fields (inset marked A, B and C) display differences between room and high

temperature experiments. In particular for high temperature strain fields, localization of strains along the slip lines appear instantaneously (similar to twinning at room temperature) with small load drops. Moreover, strains are more localized than the room temperature strain fields, and both the slip systems clearly appear on the surface.

5.2.2. Ex Situ Digital Image Correlation using SEM

Further improvements in the strain resolution can be achieved using high resolution images from the Scanning Electron Microscope (SEM). In the experiment presented here the sample surface was used as a speckle pattern, this allowed to reach very high image magnifications (900x). Figure 5.4 shows one of the first correlations implemented. Twin-twin interaction is studied focusing on the strain field surrounding the twins. Due to the particular speckle pattern adopted, the twinned regions cannot be correlated. Nevertheless these limitations, other important information can be extracted from the regions which were correlated.

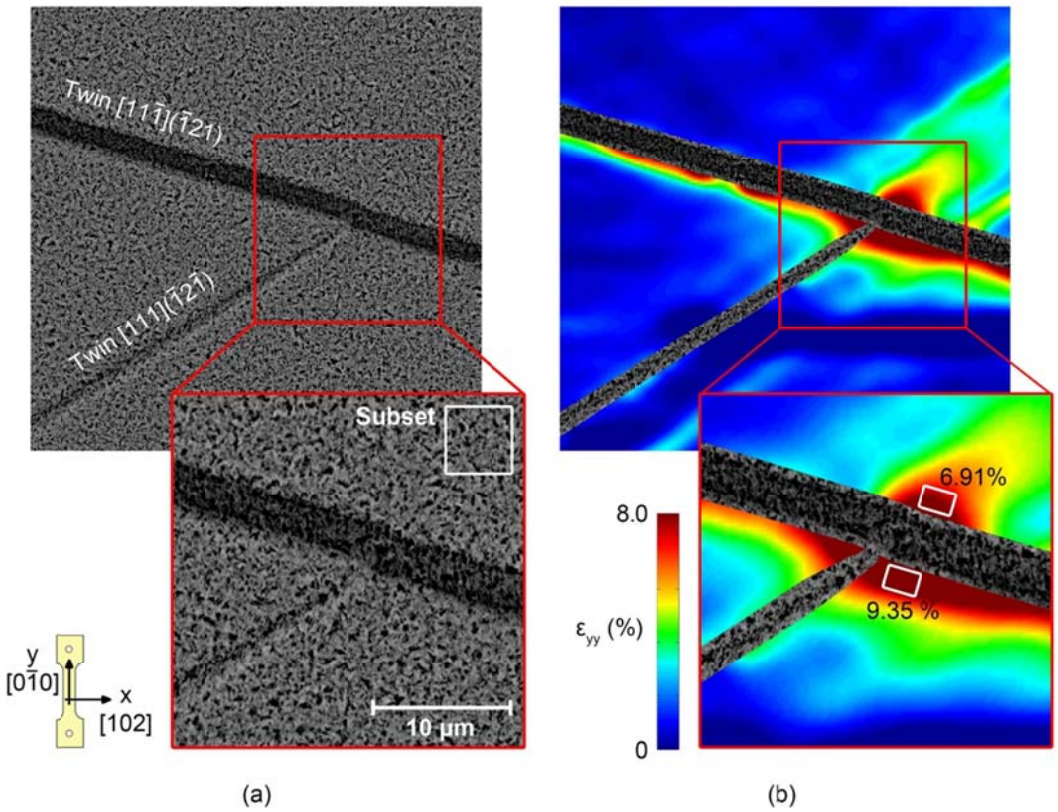

Figure 5.4. Twin-twin interaction studied using high resolution DIC from SEM images. (a) Speckle pattern adopted and subset size 5x5 µm^2; (b) Residual strain field in the axial direction, high strain localization are observed in the region of the twin-twin interaction, in particular on the obstacle twin side where the incoming twin is blocked.

For the case of twin-twin interaction reported in Figure 5.4 is possible to notice the residual strain field surrounding the region of interaction, that is the region where the $[111](\bar{1}2\,\bar{1})$ twin system is

blocked in front of the obstacle $[11\bar{1}](\bar{1}21)$ twin system. In particular on the twin boundary where the incoming $[111](\bar{1}2\bar{1})$ is blocked high strains are measured in the surrounding matrix. This is true for the intersection region (zoomed region on Figure 5.4b), and also along the blocked twin, on the side of the incoming twin. These results can be analyzed and interpreted with Molecular Dynamics. The dislocation mechanisms can be derived and used to interpret the measured strain fields shown.

References

1. Hobrough, A.G.L., *The Photogrammetric Record.* 2003. **18(104)**: p. 337-340.

2. Sutton, M.A., J.-J. Orteu, and H. W. Schreier, *Image Correlation for Shape, Motion and Deformation Measurements: Basic Concepts, Theory and Applications*. 2009.

3. Dainty, J.C., *Laser Speckle and Related Phenomena.* Laser Speckle and Related Phenomena, 1984. **XVII**.

4. Archbold, E., J.M. Burch, and A.E. Ennos, *Recording of In-plane Surface Displacement by Double-exposure Speckle Photography.* Optica Acta: International Journal of Optics, 1970. **17**(12): p. 883-898.

5. Archbold, E. and A.E. Ennos, *Displacement Measurement from Double-exposure Laser Photographs.* Optica Acta: International Journal of Optics, 1972. **19**(4): p. 253-271.

6. Forno, C., *White-light speckle photography for measuring deformation, strain, and shape.* Optics & Laser Technology, 1975. **7**(5): p. 217-221.

7. Luxmoore, A.R., F.A.A. Amin, and W.T. Evans, *In-plane strain measurement by speckle photography: A practical assessment of the use of Young's fringes.* The Journal of Strain Analysis for Engineering Design, 1974. **9**(1): p. 26-35.

8. Stetson, K.A., *New design for laser image—speckle interferometer.* Optics Technology, 1970. **2**(4): p. 179-181.

9. Peters, W.H. and W.F. Ranson, *Digital Imaging Techniques In Experimental Stress Analysis.* Optical Engineering, 1982. **21**(3): p. 213427-213427.

10. Peters, W.H., et al., *Application Of Digital Correlation Methods To Rigid Body Mechanics.* Optical Engineering, 1983. **22**(6): p. 226738-226738.

11. Sutton, M.A., et al., *Determination of displacements using an improved digital correlation method.* Image and Vision Computing, 1983. **1**(3): p. 133.

12. Sutton, M.A., et al., *Application of an optimized digital correlation method to planar deformation analysis.* Image and Vision Computing, 1986. **4**(3): p. 143.

13. Tian, Q. and M.N. Huhns, *Algorithms for subpixel registration.* Computer Vision, Graphics, and Image Processing, 1986. **35**(2): p. 220-233.

14. Reid, C., *The association of twinning and fracture in bcc metals.* Metallurgical and Materials Transactions A, 1981. **12**(3): p. 371.

15. Ha, K.F., H.M. Zhang, and K.L. Jing, *An investigation on the mechanism of 475°C embrittlement in High-Cr ferritic stainless steel.* Metallurgical Transactions A, 1989. **20**(11): p. 2563-2567.

16. Hull, D., *Effect of grain size and temperature on slip, twinning and fracture in 3% silicon iron.* Acta Metallurgica, 1961. **9**(3): p. 191.

17. Isozaki, S., S. Takaki, and K. Abiko, *High Temperature Deformation Mechanism of a High-Purity Fe–50 mass% Cr Alloy.* physica status solidi (a), 1998. **167**(2): p. 471.

18. Kako, et al., *Effect of grain size on the deformation properties of a high-purity Fe-50Cr alloy at 293 and 773 K*. 2000, Sendai, JAPON: Japan Institute of Metals. 251.

19. Kako, K., et al., *Deformation Mechanisms in High-Purity Fe–50Cr(–5W) Alloys at Elevated Temperatures.* physica status solidi (a), 1998. **167**(2): p. 481.

20. Lagneborg, R., *Deformation in an iron-30% chromium alloy aged at 475°c.* Acta Metallurgica, 1967. **15**(11): p. 1737.

21. Mahajan, S., S. Jin, and D. Brasen, *Micro-twinning in a spinodally decomposed Fe-Cr-Co alloy.* Acta Metallurgica, 1980. **28**(7): p. 971.

22. Marcinkowski, M.J.F., R. M.; Sziemae, A., *Effect of 500°C aging on the deformation behavior of an iron-chromium alloy.* Transaction of the American Institute of Mining, Metallurgical and Petroleum Engineers, 1964. **230**: p. 676-89.

23. Christian, J.W. and S. Mahajan, *Deformation twinning.* Progress in Materials Science, 1995. **39**(1-2): p. 1.

24. A.W, S., *Twinning and the origin of cleavage nuclei in α-iron.* Acta Metallurgica, 1962. **10**(9): p. 803.

25. Sleeswyk, A.W., *½<111> screw dislocations and the nucleation of {112}<111> twins in the b.c.c. lattice.* Philosophical Magazine, 1963. **8**(93): p. 1467.

26. Cottrell, A.H. and B.A. Bilby, *LX. A mechanism for the growth of deformation twins in crystals.* Philosophical Magazine Series 7, 1951. **42**(329): p. 573-581.

27. Mahajan, S., *Nucleation and growth of deformation twins in Mo-35 at. % Re alloy.* Philosophical Magazine, 1972. **26**(1): p. 161.

28. Cahn, R.W., *Plastic deformation of alpha-uranium; twinning and slip.* Acta Metallurgica, 1953. **1**(1): p. 49.

29. Karaman, I., et al., *Deformation of single crystal Hadfield steel by twinning and slip.* Acta Materialia, 2000. **48**(6): p. 1345.

30. Venables, J.A., *The electron microscopy of deformation twinning.* Journal of Physics and Chemistry of Solids, 1964. **25**(7): p. 685.

31. Ezaz, T., M.D. Sangid, and H. Sehitoglu, *Energy barriers associated with slip-twin interactions.* Philosophical Magazine, 2011. **91**(10): p. 1464.

32. Honda, R., *Cleavage Fracture in Single Crystals of Silicon Iron.* Journal of the Physical Society of Japan, 1961. **16**(7): p. 1309.

33. Kirillov, V.A., et al., *The relation between twinning and brittle failure in single crystals of Fe-Cr-Co-Mo.* Phys. Met. Metall., 1989. **68**: p. 133-138.

34. Priestner, R. and N. Louat, *Twinning and fracture in grain-oriented silicon steel.* Acta Metallurgica, 1963. **11**(3): p. 195.

35. Levasseur, J., *Étude géometrique de l'intersection des macles et de l'interaction macle-glissement dans le fer [alpha].* Materials Science and Engineering, 1969. **4**(6): p. 343.

36. Magnin, T., L. Coudreuse, and A. Fourdeux, *Consequences of slip-twinning interactions on the monotonic and cyclic deformation of b.c.c. stainless steels.* Materials Science and Engineering, 1984. **63**(1): p. L5.

37. Mahajan, S. and G.Y. Chin, *Twin-slip, twin-twin and slip-twin interactions in Co-8 wt.% Fe alloy single crystals.* Acta Metallurgica, 1973. **21**(2): p. 173.

38. Mahajan, S., *Twin-Slip And Twin-Twin Interactions In Mo-35 At Per Cent Re Alloy.* Philosophical Magazine, 1971. **23**(184): p. 781-&.

39. Mathur, K.K. and P.R. Dawson, *On modeling the development of crystallographic texture in bulk forming processes.* International Journal of Plasticity, 1989. **5**(1): p. 67.

40. Karaman, I., et al., *Modeling the deformation behavior of Hadfield steel single and polycrystals due to twinning and slip.* Acta Materialia, 2000. **48**(9): p. 2031.

41. Kalidindi, S.R., C.A. Bronkhorst, and L. Anand, *Crystallographic texture evolution in bulk deformation processing of FCC metals.* Journal of the Mechanics and Physics of Solids, 1992. **40**(3): p. 537.

42. Lebensohn, R.A. and C.N. Tomé, *A self-consistent anisotropic approach for the simulation of plastic deformation and texture development of polycrystals: Application to zirconium alloys.* Acta Metallurgica et Materialia, 1993. **41**(9): p. 2611-2624.

43. Abuzaid, W., et al., *Slip transfer and plastic accumulation across grain boundaries in hastelloy X.* J. Mech. Phys. Solids, 2012.

44. Hook, R.E. and J.P. Hirth, *The deformation behavior of isoaxial bicrystals of Fe-3%Si.* Acta Metallurgica, 1967. **15**(3): p. 535.

45. Hook, R.E. and J.P. Hirth, *The deformation behavior of non-isoaxial bicrystals of Fe-3% Si.* Acta Metallurgica, 1967. **15**(7): p. 1099.

46. Šittner, P., V. Novák, and J. Brádler, *Persistent slip band - Grain boundary interactions in low strain fatigue of isoaxial Fe-14wt. %Cr bicrystals.* Scripta Metallurgica et Materialia, 1992. **27**(6): p. 705.

47. Šittner, P. and V. Paidar, *Observation and interpretation of grain boundary compatibility effects in Fe-3.3wt%Si bicrystals.* Acta Metallurgica, 1989. **37**(7): p. 1717.

48. Lee, T., I. Robertson, and H. Birnbaum, *An In Situ transmission electron microscope deformation study of the slip transfer mechanisms in metals.* Metallurgical and Materials Transactions A, 1990. **21**(9): p. 2437.

49. Aifantis, K.E., et al., *Interfaces within strain gradient plasticity: Theory and experiments.* Acta Materialia, 2006. **54**(19): p. 5077.

50. Soifer, Y.M., et al., *Nanohardness of copper in the vicinity of grain boundaries.* Scripta Materialia, 2002. **47**(12): p. 799.

51. Wang, M.G. and A.H.W. Ngan, *Indentation strain burst phenomenon induced by grain boundaries in niobium.* Jouenal of Materials Research, 2004. **19**: p. 2478-2486.

52. Britton, T.B., D. Randman, and A.J. Wilkinson, *Nanoindentation study of slip transfer phenomenon at grain boundaries.* Journal of Materials Research, 2009. **24**(03): p. 607-615.

53. Wo, P.C. and A.H.W. Ngan, *Investigation of slip transmission behavior across grain boundaries in polycrystalline Ni3Al using nanoindentation.* Journal of Materials Research, 2004. **19**(01): p. 189-201.

54. Hosford, W.F., *Mechanical Behavior of Materials*. 2005: Cambridge University Press.

55. Patriarca, L., et al., *Twin nucleation and migration in FeCr single crystals.* Materials Characterization, 2013. **75**(0): p. 165-175.

56. Clark, W.A.T., et al., *The use of the transmission electron microscope in analyzing slip propagation across interfaces.* Ultramicroscopy, 1989. **30**(1â€“2): p. 76.

57. Sangid, M.D., et al., *Energy of slip transmission and nucleation at grain boundaries.* Acta Materialia. **59**(1): p. 283.

58. de Koning, M., et al., *Modeling of dislocationâ€“grain boundary interactions in FCC metals.* Journal of Nuclear Materials, 2003. **323**(2â€“3): p. 281.

59. Dimiduk, D.M., *Gamma titanium aluminide alloysâ€”an assessment within the competition of aerospace structural materials.* Materials Science and Engineering: A, 1999. **263**(2): p. 281.

60. Winstone, M.R., A. Partridge, and J.W. Brooks, *The contribution of advanced high-temperature materials to future aero-engines.* Proceedings of the Institution of Mechanical Engineers, Part L: Journal of Materials Design and Applications, 2001. **215**(2): p. 63-73.

61. Bartolotta, P., et al., *The use of cast Ti−48Al−2Cr−2Nb in jet engines.* JOM Journal of the Minerals, Metals and Materials Society, 1997. **49**(5): p. 48.

62. Hénaff, G. and A.-L. Gloanec, *Fatigue properties of TiAl alloys.* Intermetallics, 2005. **13**(5): p. 543.

63. Ng, B.C., et al., *The role of mechanical twinning on microcrack nucleation and crack propagation in a near-γ TiAl alloy.* Intermetallics, 2004. **12**(12): p. 1317-1323.

64. Kad, B.K., M. Dao, and R.J. Asaro, *Numerical simulations of plastic deformation and fracture effects in two phase γ-TiAl + α2-Ti3Al lamellar microstructures.* Philosophical Magazine A, 1995. **71**(3): p. 567-604.

65. Leyens, C. and M. Peters, *Titanium and Titanium Alloys*. 2003: WILEY-VCH.

66. Carroll, J., et al., *An experimental methodology to relate local strain to microstructural texture.* Review of Scientific Instruments, 2010. **81**(8).

67. Bruck, H., et al., *Digital image correlation using Newton-Raphson method of partial differential correction.* Experimental Mechanics, 1989. **29**(3): p. 261.

68. Chu, T., W. Ranson, and M. Sutton, *Applications of digital-image-correlation techniques to experimental mechanics.* Experimental Mechanics, 1985. **25**(3): p. 232.

69. Carroll, J., et al., *Investigation of fatigue crack closure using multiscale image correlation experiments.* Engineering Fracture Mechanics, 2009. **76**(15): p. 2384-2398.

70. Efstathiou, C., H. Sehitoglu, and J. Lambros, *Multiscale strain measurements of plastically deforming polycrystalline titanium: Role of deformation heterogeneities.* International Journal of Plasticity. **26**(1): p. 93.

71. *Deformation Twinning*. 1963. Gainesville, Florida: Gordon and Breach Science Publishers / New York - London - Paris.

72. Baeslack Iii, W.A., et al., *Metallography of gamma titanium aluminides.* Materials Characterization, 1993. **31**(4): p. 197-207.

73. Engler, O. and V. Randle, *Introduction to Texture Analysis*. 2010: CRC Press.

74. Christian, J., *Some surprising features of the plastic deformation of body-centered cubic metals and alloys.* Metallurgical and Materials Transactions A, 1983. **14**(7): p. 1237.

75. Schmid, E., Proc. Internat. Cong. Appl. Mech., 1924.

76. Nabarro, F.R.N., *Extended dislocations and the schmid law of resolved shear stress.* Philosophical Magazine, 1966. **14**(130): p. 861.

77. Vitek, V., M. Mrovec, and J.L. Bassani, *Influence of non-glide stresses on plastic flow: from atomistic to continuum modeling.* Materials Science and Engineering: A, 2004. **365**(1-2): p. 31.

78. Duesbery, M.S. and V. Vitek, *Plastic anisotropy in b.c.c. transition metals.* Acta Materialia, 1998. **46**(5): p. 1481.

79. Sleeswyk, A.W. and J.N. Helle, *Zigzag configurations of twins in α-iron.* Acta Metallurgica, 1961. **9**(4): p. 344.

80. Weertman, J. and J.R. Weertman, *Elementary Dislocation Theory*. 1992: Oxford University Press.

81. Efstathiou, C. and H. Sehitoglu, *Strain hardening and heterogeneous deformation during twinning in Hadfield steel.* Acta Materialia, 2009. **58**(5): p. 1479.

82. Hirth, J., *The influence of grain boundaries on mechanical properties.* Metallurgical and Materials Transactions B, 1972. **3**(12): p. 3047.

83. Sutton, A.P. and R.W. Balluffi, *Interfaces in crystalline materials*. 1995: Clarendon Press.

84. Lim, L.C., *Slip-twin interactions in nickel at 573K at large strains.* Scripta Metallurgica, 1984. **18**(10): p. 1139.

85. Lim, L.C. and R. Raj, *Continuity of slip screw and mixed crystal dislocations across bicrystals of nickel at 573 K.* Acta Metallurgica, 1985. **33**(8): p. 1577.

86. Lim, L.C. and R. Raj, *The role of residual dislocation arrays in slip induced cavitation, migration and dynamic recrystallization at grain boundaries.* Acta Metallurgica, 1985. **33**(12): p. 2205.

87. Abuzaid, W., et al., *The Role of Slip Transmission on Plastic Strain accumulationacross Grain Boundaries.* Procedia IUTAM. **4**(0): p. 169.

88. Seeger, A., *Experimental evidence for the {110} ↔ {112} transformation of the screw-dislocation cores in body-centred cubic metals.* physica status solidi (a), 2004. **201**(4): p. R21.

89. Sutton, M., et al., *Full-field representation of discretely sampled surface deformation for displacement and strain analysis.* Experimental Mechanics, 1991. **31**(2): p. 168.

90. Hirth, J. and J. Lothe, *Theory of Dislocations*. Second ed. 1982: John Wiley and Sons, Inc.

91. Filippini, M., et al., *Defect tolerance of a gamma titanium aluminide alloy.* Procedia Engineering, 2011. **10**(0): p. 3677-3682.

92. Biamino, S., et al., *Electron beam melting of Ti-48Al-2Cr-2Nb alloy: Microstructure and mechanical properties investigation.* Intermetallics. **19**(6): p. 776.

93. Murr, L.E., et al., *Characterization of titanium aluminide alloy components fabricated by additive manufacturing using electron beam melting.* Acta Materialia. **58**(5): p. 1887.

94. Andersson, L.E. and M. Larsson, *Device and Arrangement for producing a Three-Dimensional Object*, 2001.

95. Sauthoff, G., *Intermetallics*. 1995: VCH.

96. McCullough, C., et al., *Phase equilibria and solidification in Ti-Al alloys.* Acta Metallurgica, 1989. **37**(5): p. 1321-1336.

97. Gloanec, A.L., et al., *Cyclic deformation mechanisms in a gamma titanium aluminide alloy at room temperature.* Scripta Materialia, 2005. **52**(2): p. 107-111.

98. Appel, F., J.D.H. Paul, and M. Oehring, *Gamma Titanium Aluminide Alloys*. 2011: Wiley.

99. Yoo, M.H., J. Zou, and C.L. Fu, *Mechanistic modeling of deformation and fracture behavior in TiAl and Ti3Al.* Materials Science and Engineering: A, 1995. **192-193, Part 1**(0): p. 14.

100. Tanaka, K., Y. Nakai, and M. Yamashita, *Fatigue growth threshold of small cracks.* International Journal of Fracture, 1981. **17**(5): p. 519.

101. Voice, W.E., et al., *Gamma titanium aluminide, TNB.* Intermetallics, 2005. **13**(9): p. 959.

102. Pippan, R., et al., *Fatigue threshold and crack propagation in Î³-TiAl sheets.* Intermetallics, 2001. **9**(1): p. 89.

103. García, A. and H. Sehitoglu, *Contact of crack surfaces during fatigue: Part 1. formulation of the model.* Metallurgical and Materials Transactions A, 1997. **28**(11): p. 2263-2275.

104. Sehitoglu, H. and A. García, *Contact of crack surfaces during fatigue: Part 2. Simulations.* Metallurgical and Materials Transactions A, 1997. **28**(11): p. 2277-2289.

105. Gloanec, A.L., et al., *Fatigue crack growth behaviour of a gamma-titanium-aluminide alloy prepared by casting and powder metallurgy.* Scripta Materialia, 2003. **49**(9): p. 825.